INCREASING THE IONIC CONDUCTIVITY OF SODIUM-BASED CERAMIC-POLYMER COMPOSITE ELECTROLYTES AND IMPROVING THE INTERFACIAL CONDITIONS

by

Uğur Cucu

B.S., Mechanical Engineering, Istanbul Technical University, 2020

Submitted to the Institute for Graduate Studies in
Science and Engineering in partial fulfillment of
the requirements for the degree of
Master of Science

Graduate Program in Mechanical Engineering
Boğaziçi University

2024

ACKNOWLEDGEMENTS

First and foremost, I would like to thank Prof. Nuri Ersoy for his invaluable support and academic guidance throughout my thesis. I am deeply grateful for our enriching conversations on academic, social, and political issues. I am also grateful to my co-supervisor, Assoc. Prof. Gülin Vardar, for broadening my perspective on my thesis topic.

I would like to thank Assoc. Prof. Oktay Demircan, Eslem, Furkan, Hüseyin and Janset for their help in my experimental studies and for sharing their experiences with me.

I am deeply grateful to my friends Mehmet Can Engül, Serdar Demir and Kaveh Shahidi, who have been with me since the beginning of my masters and with whom I have shared many things.

I am grateful to Demet Mansuroğlu who has given me incredible support with her guidance during my thesis research. I would also like to thank my friend Mustafa Kangal for his support during the course and thesis terms.

I would like to thank TÜBITAK for financially supporting my work within the scope of the 1004-P4B project.

Finally, I would like to express my deepest gratitude to my beloved family. I extend my heartfelt thanks to my mother, Gülcan Cucu, and my father, Mehmet Cucu, for their unwavering trust and support. I am also grateful to my sister, Tuğçe Cucu, for her constant encouragement, and to my dear wife, Berivan, for always being by my side.

ABSTRACT

INCREASING THE IONIC CONDUCTIVITY OF SODIUM-BASED CERAMIC-POLYMER COMPOSITE ELECTROLYTES AND IMPROVING THE INTERFACIAL CONDITIONS

Studies in the field of solid electrolytes have accelerated due to safety problems such as leakage and ignition of liquid electrolytes. While batteries have become safer with improvements in solid electrolytes, problems like poor contact surface and low strength of solid electrolytes have emerged. These obstacles for the ionic conductivity of electrolytes are being overcome by the development of composite electrolytes; however, the effect of variables such as pressure and temperature on ionic conductivity is not sufficiently understood. This study aims to synthesize NASICON-polymer composite electrolytes and investigate the effects of pressure and temperature on ionic conductivity. For this purpose, an experimental study is conducted covering the production process of electrolytes and the design of a test rig that enables to measure the change of ionic conductivity under pressure and temperature. Solid electrolytes with different proportions of NASICON are prepared. XRD, SEM and FTIR studies are carried out for the characterization of the electrolyte. Electrochemical impedance spectroscopy measurements are taken. The findings indicate that the 25% NASICON additive electrolyte has the highest ionic conductivity. The ionic conductivity value is measured as 5.19×10^{-5} S cm^{-1} that is consistent with previous studies. Electrochemical impedance spectroscopy measurements of the samples are taken under various pressure and temperature values, and the mechanisms that explain how these variables affect the ionic conductivity are elaborated.

ÖZET

SODYUM BAZLI SERAMİK-POLİMER KOMPOZİT ELEKTROLİTLERİN İYONİK İLETKENLİĞİNİN ARTIRILMASI VE ARAYÜZEY KOŞULLARININ İYİLEŞTİRİLMESİ

Sıvı elektrolitlerin sızdırma ve tutuşma gibi güvenlik sorunları sebebiyle katı elektrolitler alanındaki çalışmalar hızlanmıştır. Katı elektrolitlerdeki gelişmelerle birlikte bataryalar daha güvenli hale gelirken katı elektrolitlerin zayıf temas yüzeyi ve düşük mukavemet gibi sorunları ortaya çıkmıştır. Elektrolitlerin iyonik iletkenliği önündeki bu engeller kompozit elektrolitlerin geliştirilmesiyle aşılmaya çalışılmaktadır; ancak basınç ve sıcaklık gibi değişkenlerin iyonik iletkenlik üzerindeki etkisi yeterince anlaşılamamıştır. Bu çalışmanın amacı, NASICON-polimer kompozit elektrolitlerini sentezlemek ve basınç ile sıcaklığın iyonik iletkenlik üzerindeki etkilerini araştırmaktır. Bu amaçla elektrolitlerin üretim sürecini, basınç ve sıcaklık altında iyonik iletkenliğin değişimini gösteren bir düzeneğin tasarlanmasını kapsayan bir çalışma yürütülmüştür. Farklı oranlarda NASICON katkılı elektrolitler hazırlanmıştır. Elektrolitin karakterizasyonu için XRD, SEM ve FTIR çalışmaları yapılmıştır. Elektrokimyasal empedans spektroskopi testleri yapılmıştır. Elde edilen bulgular yüzde 25 NASICON katkılı elektrolitin en yüksek iyonik iletkenliğe sahip olduğunu göstermektedir. İyonik iletkenlik değeri $5.19 \times 10^{-5}\,\mathrm{S\ cm^{-1}}$ olarak ölçülmüştür ve bu değer önceki çalışmalarla tutarlıdır. Numunelerin Elektrokimyasal empedans spektroskopi ölçümleri çeşitli basınç ve sıcaklık değerleri altında yapılmış ve bu değişkenlerin iyonik iletkenliği hangi mekanizmalarla nasıl etkilediği açıklanmıştır.

TABLE OF CONTENTS

ACKNOWLEDGEMENTS iii
ABSTRACT iv
ÖZET v
LIST OF FIGURES vii
LIST OF TABLES xii
LIST OF SYMBOLS xiii
LIST OF ACRONYMS/ABBREVIATIONS xv
1. INTRODUCTION 1
1.1. High Conductivity or High Strength: Liquid and Solid Electrolytes . . 1
1.2. Two Core Ion Sources: Lithium and Sodium 4
1.3. Polymer Matrix and Ion Transfer Mechanism 6
1.4. Inorganic Additives 9
1.5. Composite Electrolytes 12
2. EXPERIMENTAL STUDY 17
2.1. Preparation of Solid Polymer Electrolytes (SPEs) 18
2.2. Preparation of NASICON-PEO Composite Solid Electrolytes (CSEs) . 19
2.3. Characterization of the CSEs 20
3. RESULTS AND DISCUSSION 25
3.1. Effects of Ball-Milling on Conductivity and Surface Condition of CSE . 27
3.2. Effects of the Weight Percent of NASICON on Ionic Conductivity . . . 35
3.3. XRD Studies of the CSE Thin Films 40
3.4. FTIR Studies of the CSE Thin Films 43
3.5. Ionic Conductivity Studies of the CSE Thin Films 46
3.6. Effect of Pressure and Preload on Ionic Conductivity 52
4. CONCLUSION 63
5. FUTURE WORK 65
REFERENCES 67
APPENDIX A: ADDITIONAL FIGURES 81

LIST OF FIGURES

Figure 1.1. Schematic representation of the liquid electrolyte and interfaces. . 2

Figure 1.2. Schematic representation of the solid electrolyte and interfaces. . . 3

Figure 1.3. Inorganic fillers doped PEO matrix. 7

Figure 1.4. Na^+ transport in polymer chains. 8

Figure 1.5. Schematic representation of the structures of (a) copolymer, (b) cross-linked polymer and (c) polymer blends. 9

Figure 1.6. Rhombohedral and monoclinic phases of NASICON structure [59]. 11

Figure 1.7. General characteristics of Composite Solid Electrolytes (CSEs). . . 12

Figure 1.8. The representation of (a) Na^+ ion transfer and dendrite growths through ISE and SPE, (b) electrode for ISEs, (c) electrode for SPEs, (d) polymer chains, (e) suppressed dendrite, (f) developed dendrite, (g) Na^+ ions, (h) inorganic fillers and ion transport, (i) ion pathways across ISEs and (j) ion pathways across SPEs. 14

Figure 2.1. SEM images of as received PEO at (a) 1500 magnifications, (b) 5000 magnifications, (c) 10000 magnifications and (d) 20000 magnifications. 17

Figure 2.2. SEM images of as received NASICON at (a) 5000 magnifications, (b) 10000 magnifications, (c) 50000 magnifications and (d) 50000 magnifications. 18

Figure 2.3. Schematic representation of the production process of the CSE. . . 19

Figure 2.4. Cross-sectional view of the test rig. (a) Contact channel, (b) lid, (c) rod, (d) copper tube, (e) polyamide body, (f) rod, (g) lid, (h) centralizer, (i) copper tube, (j) probe channel, (k) CSE thin film, (l) centralizer, and (m) spring. 22

Figure 2.5. Representation of the test apparatus designed to measure impedance at different temperatures. 23

Figure 2.6. Disassembled view of the mechanical device. (a) Lid, (b) polyamide body, (c) probe channel (d) lid, (e) copper tube, (f) contact channel, (g) centralizer, (h) rod, (i) CSE thin film, (j) rod, (k) copper tube, (l) centralizer, and (m) spring. 24

Figure 3.1. The ionic conductivity of SPEs with various EO:Na^+ ratios at room temperature. 26

Figure 3.2. SEM images of SPE (PEO and 15.6 wt% $NaClO_4$) at (a) 1200 magnifications, (b) 3000 magnifications, (c) 6000 magnifications and (d) 12000 magnifications. 27

Figure 3.3. SEM images of the surface of CSE 25 wt% NASICON before ball-milling. 28

Figure 3.4. EDX analysis of the surface of CSE 25 wt% NASICON before ball-milling in terms of (a) oxygen, (b) zirconium and silicon, (c) sodium and (d) zirconium. 29

Figure 3.5. Cross-sectional view of CSE containing 25 wt% NASICON before ball-milling. 31

Figure 3.6. SEM images of the surface of CSE 25 wt% NASICON after ball-milling at (a) 1000 magnifications, (b) 1000 magnifications, (c) 4000 magnifications and (d) 4000 magnifications. 32

Figure 3.7. EDX Analysis of the surface of CSE 25 wt% NASICON in terms of (a) oxygen, (b) sodium, (c) zirconium and (d) silicon. 33

Figure 3.8. Particle size of NASICON after 70 hours ball-milling. 33

Figure 3.9. Cross-sectional view of CSE containing 25 wt% NASICON after ball-milling. 34

Figure 3.10. Cross-sectional view of CSE containing 25 wt% NASICON after ball-milling at 1500 magnification showing the locations of two points and one region where the weight percentages of zirconium are shown. 34

Figure 3.11. Ionic conductivity of CPE with different NASICON content at different temperatures. 35

Figure 3.12. Cross-sectional image of CSE containing 20 wt% NASICON at (a) 1500 magnifications and (b) 3000 magnifications. 37

Figure 3.13. Cross-sectional image of CSE containing 25 wt% NASICON at (a) 1500 magnifications and (b) 3000 magnifications. 37

Figure 3.14. Cross-sectional image of CSE containing 30 wt% NASICON at (a) 1500 magnifications and (b) 3000 magnifications. 37

Figure 3.15. Cross-sectional image of CSE containing 40 wt% NASICON at (a) 1500 magnifications and (b) 3000 magnifications. 39

Figure 3.16. Thickness of CSE thin films with (a) 20 wt% NASICON, (b) 25 wt% NASICON, (c) 30 wt% NASICON and (d) 40 wt% NASICON. 40

Figure 3.17. X-ray diffraction (XRD) patterns of the PEO, $NaClO_4$, NASICON and CSE. 41

Figure 3.18. X-ray diffraction (XRD) patterns of the CSE with 0, 20, 25, 30 wt% NASICON. 43

Figure 3.19. FTIR analysis of CSE 25 wt% NASICON. 44

Figure 3.20. FTIR analysis of CSEs with 20-25-30 wt% NASICON. 45

Figure 3.21. Nyquist plots of the CSEs containing 20, 25, 30 and 40 wt% NASICON at 25 °C. 46

Figure 3.22. Nyquist plots of the CSEs at different temperatures. 47

Figure 3.23. Equivalent circuit models for fitting studies of EIS in terms of (a) R's and C, (b) R's, C and W, (c) R and CPE's, and (d) R's and CPE's. 48

Figure 3.24. Fitting studies of equivalent circuit models. 49

Figure 3.25. Arrhenius plots of the CSEs with 20-25-30-40 wt% NASICON. . . 50

Figure 3.26. Activation energy of CSEs with 20, 25, 30 and 40 wt% NASICON. 51

Figure 3.27. One cycle compression-relaxation plot of CSE. 53

Figure 3.28. Two cycles compression-relaxation plot of CSE. 56

Figure 3.29. Three cycles compression-relaxation plot of CSE. 56

Figure 3.30. First compression and third relaxation of CSE. 57

Figure 3.31. Second and third compression of CSE. 58

Figure 3.32. Thinning of CSE film at the centre after the third compression cycle. 59

Figure 3.33. The onset of tearing of CSE thin film with the third compression. 60

Figure 3.34. Tearing of CSE thin film with third compression. 60

Figure 3.35. Cross-sectional image of CSE after first compression at (a) 800 magnifications and (b) 1600 magnifications. 61

Figure 3.36. Cross-sectional image of CSE after second compression at (a) 800 magnifications and (b) 1500 magnifications. 61

Figure 3.37. Cross-sectional image of CSE after third compression at (a) 800 magnifications and (b) 1500 magnifications. 62

Figure A.1. Permission for Figure 1.6. 81

Figure A.2. The error rates of the parameters of the CPEs and resistors in (a) equivalent circuit of c, and (b) equivalent circuit of d. 82

Figure A.3. The error rates of the CSEs containing (a) 20 wt% NASICON, (b) 25 wt% NASICON, (c) 30 wt% NASICON, and (d) 40 wt% NASICON. 82

LIST OF TABLES

Table 1.1. Ionic conductivity comparison of liquid and solid electrolytes. . . . 2

Table 3.1. Percentage by weight of NASICON in the top, bottom and middle regions. 38

Table 3.2. Average, maximum, minimum thickness and standard deviation of films. 40

LIST OF SYMBOLS

$A_{contact}$	Contact area
C	Capacitance
CH_2	Carbon hydrogen bond
cm	Centimeter
C-O	Carbon oxygen bond
D	Diameter
E_A	Activation energy
e_V	Electron volt
Hz	Hertz
k_B	Boltzmann constant
kPa	Kilopascal
kV	Kilovolt
MHz	Megahertz
mL	Milliliter
mm	Millimeter
mV	Millivolt
N_c	Critical speed
nm	Nanometer
R	Resistance
s	Time-step
S	Siemens
t	Thickness
T	Temperature
V	Volt
α	Alpha radiation
θ	Scanning range angle
μm	Micrometer

σ_{ion}	Ionic conductivty
σ_0	Arrhenius pre-exponential factor

LIST OF ACRONYMS/ABBREVIATIONS

3D	Three Dimensional
AC	Alternative Current
ACN	Acetonitrile
Al_2O_3	Aluminium Oxide
Ce^{4+}	Cerium Ion
ClO_4^-	Perchlorate Ion
CPE	Constant Phase Element
CS	Chitosan
CSE	Composite Solid Electrolyte
Cu	Copper
DMAc	Dimethylacetamide
DMF	Dimethylformamide
EDX	Energy Dispersive X-ray Spectroscopy
EIS	Electrochemical Impedance Spectroscopy
EMIFSI	Ethyl Methyl Imidazolium Bis(fluorosulfonyl)imide
EO	Ethylene Oxide
F^-	Fluoride Ion
FSI	Bis(florosülfonil)imid
FTIR	Fourier Transform Infrared Spectroscopy
ISE	Inorganic Solid Electrolyte
Li^+	Lithium Ion
LiFSI	Lithium Bis(fluorosulfonyl)imide
LiPON	Lithium Phosphorus Oxynitride
LiTCM	Lithium Tricyanomethanide
LiTFSI	Lithium Bis(trifluoromethanesulfonyl)imide
MnO_2	Manganese Dioxide
Na^+	Sodium Ion
$Na_3Zr_2Si_2PO_2$	Sodium Zirconium Silicon Phosphorus Dioxide

$NaClO_4$	Sodium Perchlorate
NaFSI	Sodium bis(fluorosulfonyl)imide
NASICON	Sodium Super Ionic Conductor
NaTFSI	Sodium Bis(trifluoromethanesulfonyl)imide
Na-β/β''	Sodium Beta Alumina
PAN	Polyacrylonitrile
PC	Propylene Carbonate
PEGUPy	Poly(ethylene glycol)-co-ureidopyrimidinone
PEO	Polyethylene Oxide
PMMA	Polymethyl Methacrylate
PTFE	Polytetrafluoroethylene
PVA	Polyvinyl Alcohol
PVDF	Polyvinylidene Fluoride
Pyr	Pyrrolidinium
SEM	Scanning Electron Microscopy
SiO_2	Silicon Dioxide
SEM	Scanning Electron Microscopy
SPE	Solid Polymer Electrolyte
SSEs	Solid-state Electrolytes
TCM	Tricyanomethanide
TFSA	Bis(trifluoromethylsulfonyl)-amide
TiO_2	Titanium Dioxide
TTE	Tetrafluoroethyl
wt%	Weight Percent
XRD	X-ray Diffraction
Zr	Zirconium
ZRA	Zero Resistance Ammeter
ZrO_2	Zirconium Dioxide

1. INTRODUCTION

Batteries are used in various applications, from smartphones to laptops and electric vehicles to grid systems [1]. Due to the ever-increasing need for energy, research on battery technology is accelerating. With the improvement of manufacturing processes and the discovery of novel battery materials, efforts are being made to increase energy density and lifespan of batteries and reduce initial investment and maintenance costs [2].

Batteries consist of an anode, a cathode, an electrolyte, a separator and current collectors [3]. As the battery completes the charge-discharge cycle, ions travel back and forth between the anode and cathode along the electrolyte [4]. The function of the electrolyte is providing ionic conductvity for ion transportation between anode and cathode while preventing electron transfer. When the battery is discharged, the ions move from the anode to the cathode and for each pass, electrons pass through the circuit. Conversely, when the battery charges, the ion movement is from the cathode to the anode.

1.1. High Conductivity or High Strength: Liquid and Solid Electrolytes

Electrolytes create an interface between the anode and cathode, providing a medium for ion transfer [5]. Electrolytes are divided into two main groups according to the electrolytes' physical state: liquid and solid. Liquid electrolytes have disadvantages such as flammability, leakage, dendrite growth [6] and low mechanical strength [7]. Contrary to these issues, they have high ionic conductivity and good wettability thanks to their physical form [8]. Table 1.1 presents a comparison about the ionic conductivity between liquid and solid electrolytes. The ionic conductivity of solid electrolytes is less than 1% of the ionic conductivity of liquid electrolytes. Liquid electrolytes have ionic conductivities as high as 10^{-3} S cm^{-1}, even at low temperatures. On the other hand, polymer electrolytes have ionic conductivities ranging from 10^{-8} to 10^{-5} S cm^{-1}. Solid

electrolytes with fillers reach ionic conductivity values of 10^{-7} to 10^{-3} S cm^{-1}, while composite electrolytes can get close to the performance of liquid electrolytes [9].

Table 1.1. Ionic conductivity comparison of liquid and solid electrolytes.

		Temperature (°C)	Ionic Conductvity (S cm^{-1})	Reference
Liquid Electrolytes	[Li(triglyme)$_4$][TFSA]	30	3.80×10^{-3}	[10]
	LiTCM:Pyr$_{14}$TCM	20	5.70×10^{-3}	[11]
	LiFSI-EMIMFSI	25	7.20×10^{-3}	[12]
	LiTFSI:P$_{13}$FSI:TTE	25	3.40×10^{-3}	[13]
	LiTFSI:EMIFSI	20	5.97×10^{-3}	[14]
Solid Electrolytes	LiPON	25	2.30×10^{-6}	[15]
	PEO/NASICON/PAN	30	4.13×10^{-4}	[16]
	PEO$_{20}$NaFSI/Al$_2$O$_3$	30	1.00×10^{-5}	[17]
	PEGUPy/NaTFSI/SiO$_2$	25	2.37×10^{-5}	[18]
	PEO$_9$NaTFSI	20	4.50×10^{-6}	[19]

Figure 1.1 illustrates the liquid electrolyte and its interface with the anode and cathode. While charge and discharge occurs, dendrite growths form in anode and reach into the electrolyte media [20]. As the charge-discharge cycle continues, the dendrite grows and after a while, it crosses the electrolyte and reaches the cathode.

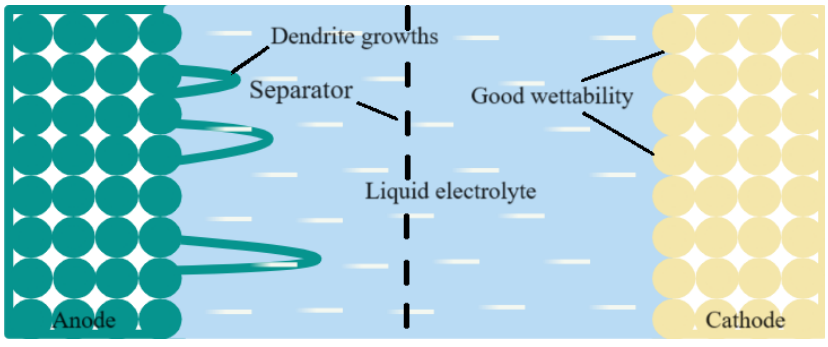

Figure 1.1. Schematic representation of the liquid electrolyte and interfaces.

In this case, electrons start to flow between the anode and cathode instead of the current collectors, and a short circuit ensues and the battery may even ignite. On the other hand, the electrolyte in liquid form assures satisfactory wettability between the anode and cathode [21]. It lessens the impedance at the interfaces between anode/electrolyte and cathode/electrolyte and regulates ion deposition [22]. Solid-state electrolytes (SSEs) have been produced to eliminate flammability and leakage problems encountered in conventional liquid electrolytes. Moreover, SSEs significantly inhibit dendrite growth at the anode and cathode interfaces [23]. Figure 1.2 demonstrates the solid electrolyte and its interface with the anode and cathode.

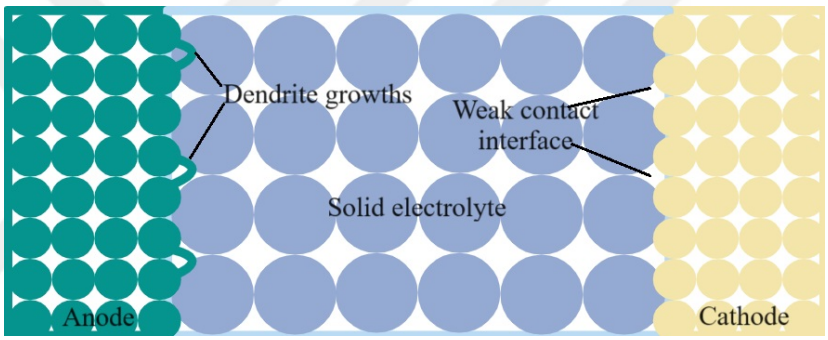

Figure 1.2. Schematic representation of the solid electrolyte and interfaces.

SSEs have higher mechanical strength than liquid electrolytes, they suppress the extension of dendrite growth into the electrolyte [24]. Solid electrolytes also exhibit a resistance to volume change during charge and discharge [25]. On the contrary, solid-state electrolytes have weak contact with electrolyte and electrode interfaces. Inadequate contact surface of the electrolyte and electrode interfaces causes impedance to rise as ion transfer occurs [26]. Although SSEs suppress dendrite growth due to their high mechanical strength, dendrite nucleation and growth can still develop at grain boundaries because of the insufficient contact surface [27]. Liu et al. [28] summarize the parameters that cause dendrite nucleation and growth, such as voids, electronic conductivity, surface and bulk defects, soft parts of electrolytes and weak solid-solid surface contact. Huo et al. [29] propose polymer-ceramic composite electrolytes are flawless dendrite suppressors and improves electrolyte/electrode interfacial contact.

The elastic nature of the polymer matrix creates an improved contact zone at the interfaces and enhances ionic conductivity [30], while the high mechanical strength provided by the ceramic dopant to the electrolyte suppresses dendrite growth.

Dendrite nucleation develops not only at electrolyte/electrode interfacial areas but also at grain boundaries within the electrolyte [31]. The dendrite nucleation that occurs within the electrolyte elevates the electronic conductivity. When this nucleation turns into dendrite growth, the electronic conductivity becomes exceptionally high and causes a short circuit in the battery. For example, Han et al. [32] investigated the relationship between lithium concentration and dendrite nucleation in the electrolyte and stated that high electronic conductivity of the electrolyte leads to dendrite formation. The findings of this study proposed that to prevent dendrite propagation throughout the electrolyte, emphasis should be placed on lessening the electronic conductivity of the electrolyte instead of increasing its ionic conductivity.

Since leakage and flammability are severe threats to battery technology, SSEs are being developed as an alternative to liquid electrolytes. Although parameters such as ionic conductivity and energy density are lower than those of liquid electrolytes, much progress has been made with solid electrolytes regarding leakage and flammability. However, the microstructure and chemical composition of solid-state electrolytes affect the battery lifetime, energy efficiency and dendrite growth through factors such as ionic conductivity, electrochemical stability and contact surface stability. Therefore, electrolytes are strengthened with various additives.

1.2. Two Core Ion Sources: Lithium and Sodium

Whether the electrolytes are liquid or solid is not the only parameter determining the battery type. Another factor is the ion source. The most widely used electrolyte material is lithium. Lithium-ion batteries stand out with their high energy density and short charging time [33]. However, considering the limited availability of lithium [34] and the environmental damage caused during the processing of lithium mines, the

search for other metals that are more abundant and more environmentally friendly as compared to lithium has accelerated. Along the way in lithium mining, large quantities of water are used to extract lithium resources from mines [35]. During this process, the waste materials, soil and rocks in the mines are also separated and these materials are mixed with the water sources. These waste materials may also contain compounds that are harmful to the environment, such as heavy metals and radioactive substances [36].

On the other hand, sodium metal is more abundant in nature than lithium and can be synthesized [37]. For example, considering that sodium salt can be obtained from the sea, it can be understood how abundant sodium metal is in nature. In this way, the production cost of sodium metal is relatively low compared to lithium metal.

In addition to the above advantages, sodium-ion batteries also have significant disadvantages. The disadvantage of sodium-based electrolytes over lithium-based electrolytes is their low ionic conductivity at room temperatures. Due to the larger radius and atomic weight of sodium ions, which are 1.3 and 3.3 times greater than those of lithium ions, respectively, the ionic conductivity of sodium-based electrolytes is lower than that of lithium [38]. Its larger diameter increases the charging time of sodium batteries as compared to lithium counterparts. Their energy density is lower than lithium-ion batteries [34]. Additively, dendritic growths at the interfaces formed by the electrolyte and the electrodes are also seen in sodium-based electrolytes. Due to its abundance, easy synthesis, low cost and safety, sodium salts have been widely used as electrolyte material [39]. Although sodium is an alternative to lithium as an ion source in electrolytes, sodium based solid electrolytes must be reinforced with a polymer matrix and various inorganic additives to compete with lithium to enhance ionic conductivity and block dendrite growth.

Various electrolytes have been developed to enrich ionic conductivity and obtain a more well-established interfacial contact. Sodium-based solid electrolytes can be grouped into three main groups: Solid Polymer Electrolytes (SPEs), Inorganic Solid Electrolytes (ISEs) and Composite Solid Electrolytes (CSEs).

1.3. Polymer Matrix and Ion Transfer Mechanism

SPEs are formed by dissolving sodium salts in the polymer matrix. Polymers dissolve in solvents such as water, acetonitrile (ACN), dimethylacetamide (DMAc), dimethylformamide (DMF) and ethanol [40–43]. Among these solvents, ACN is the most widely used because of its high ionic conductivity contribution to the electrolyte. For example, Koo et al. [44] dissolve LiTFSI salt and propylene carbonate (PC) in ACN and attribute the increase in ionic conductivity in the electrolyte to the high amount of free solvent in the form of ACN, which does not coordinate with Li ions.

Since this study aims to improve the ionic conductivity of sodium-ion solid electrolytes and the condition of the interface contact regions, it is crucial to understand how the ion transport mechanisms take place in the electrolyte. The other issue that needs to be understood is how to suppress the nucleation and growth of dendrites in the interface and electrolyte. What internal and external factors can improve interfacial conditions and increase ionic conductivity?

Sodium-based polymer electrolytes are obtained by mixing sodium salts with various polymers. The types of polymers used together with solid-state electrolytes in the literature are: Polyethylene oxide (PEO), polymethyl methacrylate (PMMA), polyvinylidene fluoride (PVDF), polyvinylidene fluoridehexafluoropropylene, polyvinyl chloride, polypropylene oxide, polyacrylonitrile (PAN), polyvinyl alcohol (PVA) [45–49].

With the help of the polar groups of the polymer compounds, sodium salts are dissolved in the polymer matrix [50]. According to the widely accepted view in the literature, ion transfer occurs in the polymer's amorphous regions since the amorphous regions are less densely packed as compared to crystalline regions. The physical explanation of this mechanism is the oscillatory movements of the molecular chains in these amorphous regions [46]. Figure 1.3 illustrates the amorphous region of the polymer matrix. The dots scattered between the polymer chains represent inorganic additives.

Inorganic fillers are used to increase the ionic conductivity and improve the mechanical strength of the electrolyte.

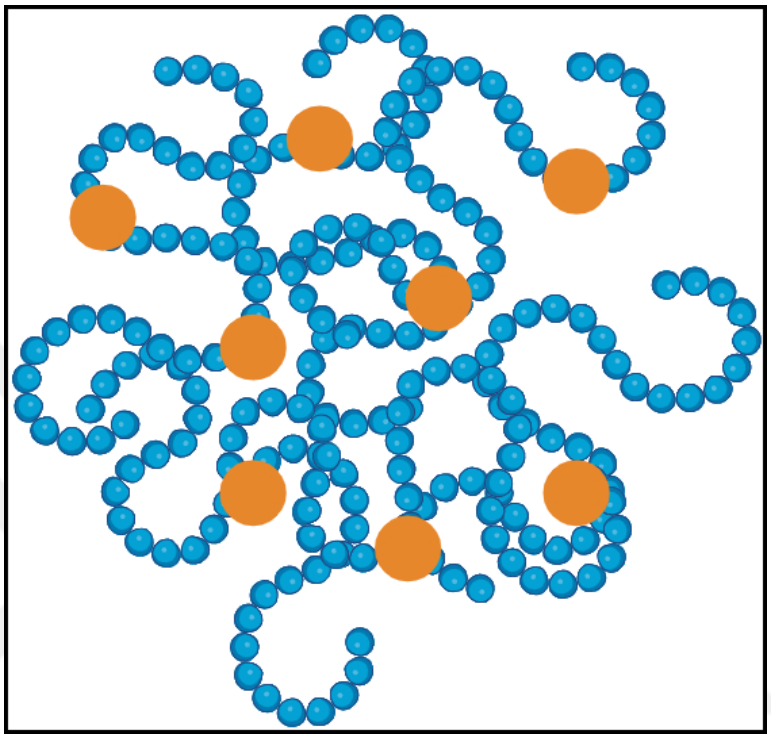

Figure 1.3. Inorganic fillers doped PEO matrix.

The transfer of ions occurs by the movement of polymer chains [51]. Quartarone et al. [52] emphasizes that ion transport in polymer-based electrolytes is related to the contraction and relaxation of polymer chains. Ion transfer can take place in the polymer matrix in three ways. Firstly, the ion attached to the active groups of the polymer chain can move in the space between the chains. Secondly, ions can move within the chain they are part of. And thirdly, ions can break away from one chain and bind to the active groups of another chain. Thus, ions are transferred through the electrolyte, traveling from the anode to the cathode and vice versa [53].

Figure 1.4 represents the transfer of a sodium ion in the polymer matrix. The structures shown in red are ethoxy groups. These structures are symbolised by (-O-) and are called active groups of polyethylene oxides. Sodium ions bind to these groups in the polymer matrix. They move on the polymer chain or between polymer chains

with the movements of polymer chains. The sodium ion attached to one polymer chain is transferred to another chain.

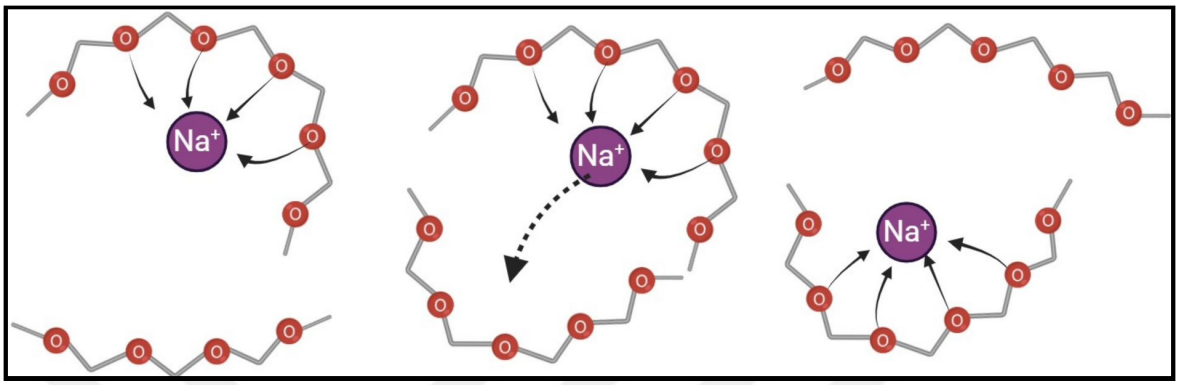

Figure 1.4. Na^+ transport in polymer chains.

SPEs are not always composed of a single polymer. By blending various polymers, the degree of crystallization of the structure is reduced and amorphous regions can be enlarged. This contributes directly to ionic conductivity by increasing the area for ion transfers to occur [54]. Figure 1.5 indicates the various types of mixed polymers. Copolymers are formed by linking two different polymer chains and are shown in Figure 1.5a. Polymers containing cross-linked bonds are shown in Figure 1.5b. Polymer blends, which are formed by mixing two different polymer types together, are shown in Figure 1.5c. Reddy et al. obtained polymer blend electrolyte films using PEO and polymethyl methacrylate (PMMA) polymer and demonstrated by X-ray diffractometer analysis how the amorphous regions increase and the crystallinity of the films decreases as a result of this blend [55].

The polymer blend ratio and the weight ratio of the salt used as an ion source affect the ionic conductivity. Nofal et al. observed that when they increased the salt concentration in the blend polymer matrix made with chitosan (CS) and PVA, ions agglomerated. As a result, he explained that ionic conductivity decreased with re-crystallization [54]. Polymer structures offer a very flexible structure as well as ion transport with the help of polymer chains. This structure increases the compatibility between the electrode surface and the electrolyte surface. This improves the contact

surfaces and facilitates ion transport. However, the low elastic modulus of polymers provides a favorable environment for dendrite growth. Therefore, inorganic additives are added to electrolytes to increase the strength of the electrolyte and suppress dendrite growths.

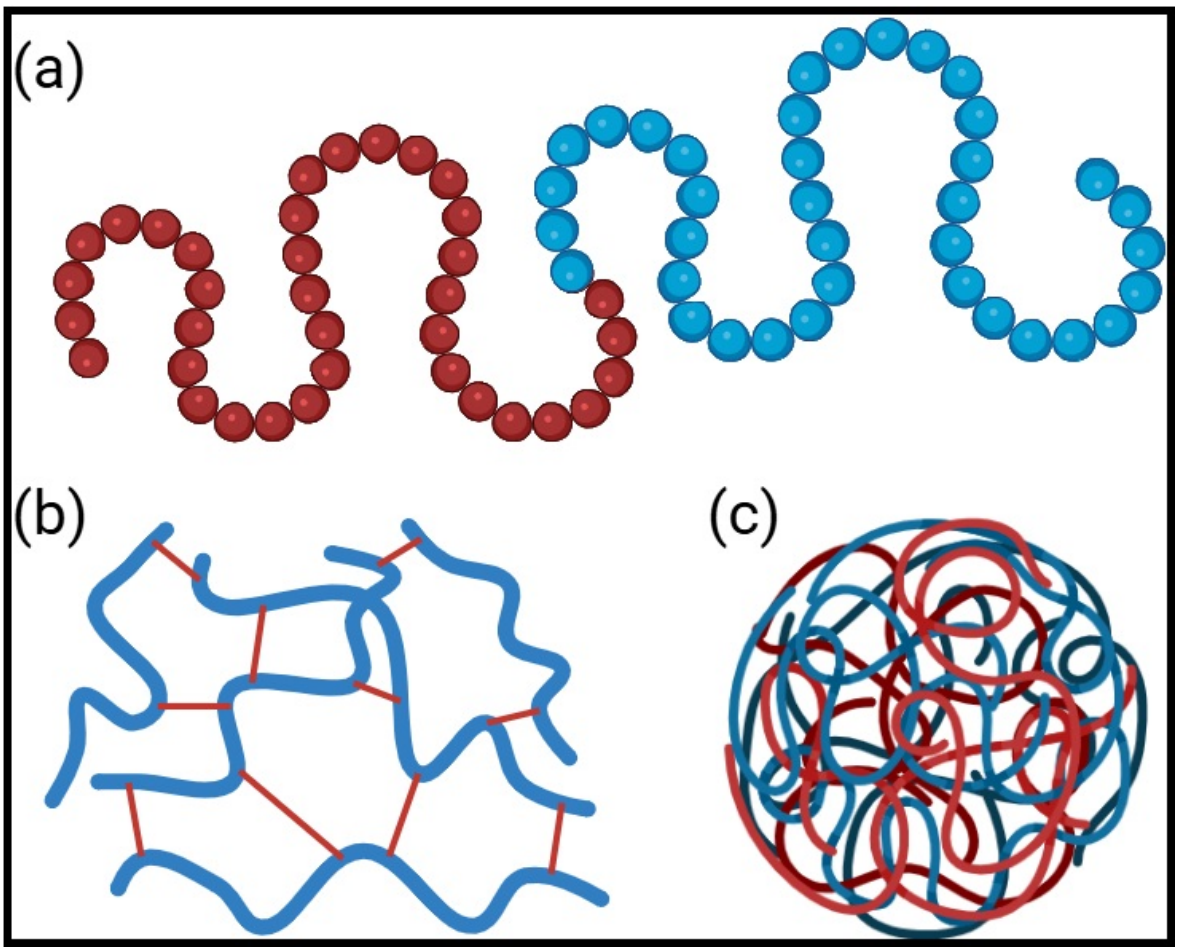

Figure 1.5. Schematic representation of the structures of (a) copolymer, (b) cross-linked polymer and (c) polymer blends.

1.4. Inorganic Additives

The ionic conductivity of polymer salt solid electrolytes ranges from 10^{-6} to 10^{-8} S cm^{-1} at room temperature. Song et al. suggested that ceramic additives can increase ionic conductivity in their study [56]. This recommendation is based on the view that ceramic fillers enrich the amorphous regions in the polymer.

Inorganic Solid Electrolytes (ISEs) are superior to polymer-based electrolytes in ionic conductivity and mechanical strength. High mechanical strength facilitates the suppression of dendrite growths, but due to low wettability and brittleness, an increase in electrolyte/electrode interfacial impedances is likely to occur [57]. Na-β/β''-Alumina and sodium superionic conductor (NASICON) salts are the most widely used inorganic additives for sodium ion electrolytes. These additives facilitate the passage of ions by forming corridors with their crystalline structures. Inorganic compounds contain defects such as Frenkel and Schottky. These defects improve the electrode-electrolyte interfacial conditions and form an efficient environment for ion transfer [58].

Na-β/β''-Alumina also provide an inhibitory environment for dendrite growths in the electrolyte by means of their low electronic conductivity. Na-β/β''-Alumina has two different crystal structures, single and polycrystal. Polycrystal structure cannot reach high ionic conductivity values compared to single due to its high grain boundary resistance [59]. Single crystal Na-β/β''-Alumina has high ionic conductivity but low thermal stability [51]. For this reason, stabilizers such as TiO_2, SiO_2, MnO_2 are used to enhance thermal stability [46], [60, 61]. Therefore, using two different crystal structures by mixing additives is essential to improve thermal stability in terms of ionic conductivity and mechanical strength.

The other inorganic filler is NASICON with the composition of $Na_3Zr_2Si_2PO_{12}$. NASICON is able to generate two phases, rhombohedral and monoclinic. These two phases contain corner-sharing tetrahedra and octahedra that form 3D channels through which sodium ions can pass. While the rhombohedral structure contains four sodium sites, one Na1 and three Na2 sites, these sites form different channels in the monoclinic structure with the splitting of Na2 sites into Na2 and Na3 sites. During these transitions between the rhombohedral structure and the monoclinic structure, the number of Na^+ ions and the number of vacancies through which the ions can pass increases, thus increasing the ionic conductivity [51]. NASICON has an ionic conductivity of 10^{-4} S cm^{-1} even at room temperatures in addition to its high mechanical strength and good chemical stability [62]. Due to its good compatibility with electrolyte/electrode

interfaces and low electronic conductivity, it has been widely studied. Figure 1.6 illustrates the rhombohedral and monoclinic phases of NASICON structure. The number of pathways through which Na^+ ions can migrate increases as the rhombohedral phase transitions to the monoclinic phase.

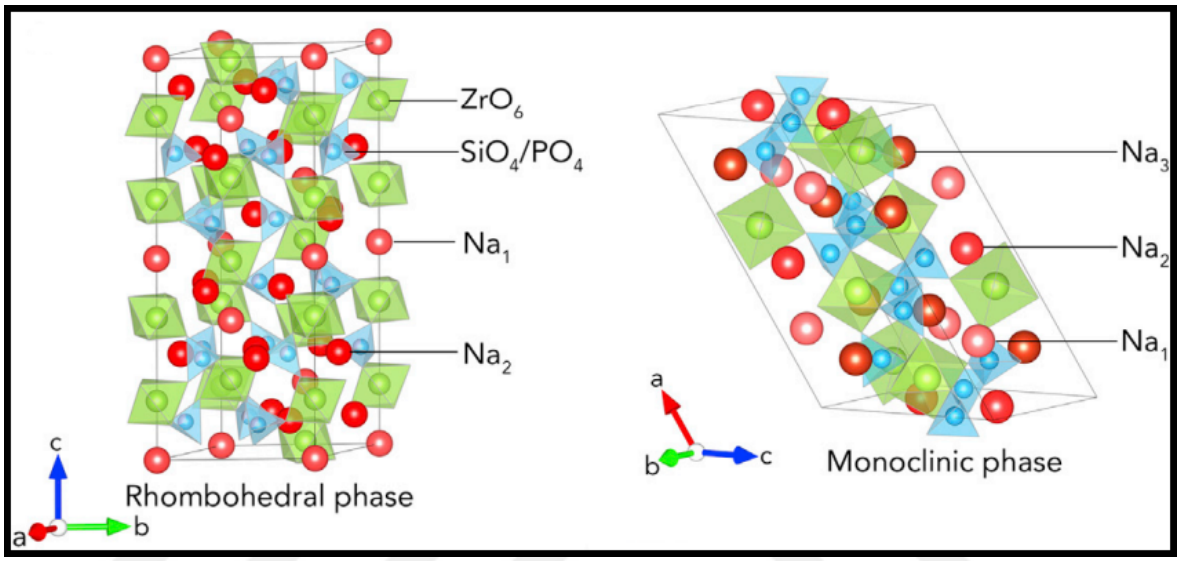

Figure 1.6. Rhombohedral and monoclinic phases of NASICON structure [59].

With the transitions between rhombohedral and monoclinic structures, the number of channels through which sodium ions can pass increases. As the regions through which the ions pass increase, the ion passage gains momentum [63]. In their study, Li et al. correlate ionic conductivity in solid electrolytes with carrier concentration, carrier mobility and charge of the transported ions [64]. While the number of channels in NASICON promotes the carrier mobility, the number of ions transported per unit of time boosts the ionic conductivity. These channels also contribute to ionic conductivity by reducing the effect of sodium ions accumulating and blocking ion transfer.

Channels are interrupted at grain boundaries. As a result, the activation energies of the ions increase and transitions become difficult. Li et al. explain NASICON's contribution to ion transfer within the grain by ion transfer through channels. They lower the activation energy of ions transferred through the electrolyte [64].

1.5. Composite Electrolytes

Composite Solid Electrolytes (CSEs) combine the following features: improved interfacial conditions and high ionic conductivity. CSEs have adequate wettability at the electrolyte/electrode interfaces due to the flexible characteristics of the polymers. Compared to the narrow contact areas caused by crystalline structures, ions can easily migrate across the polymer structure with its broad interfacial areas. The flexible structure of the polymer also has a mitigating effect on the volume change of the electrolyte during charge/discharge cycles. On the other hand, due to its low mechanical strength, the polymer cannot prevent dendrite growth through the electrolyte. The addition of inorganic additives suppresses dendrite growth. The crystal structure of inorganic compounds creates channels for ions to pass through. As a result, ionic conductivity is increased and the growth of dendrites, which can cause short circuits, is controlled. Figure 1.7 indicates how the properties from the polymer structure and inorganic fillers improve the ionic conductivity and interfacial contact conditions of the electrolyte.

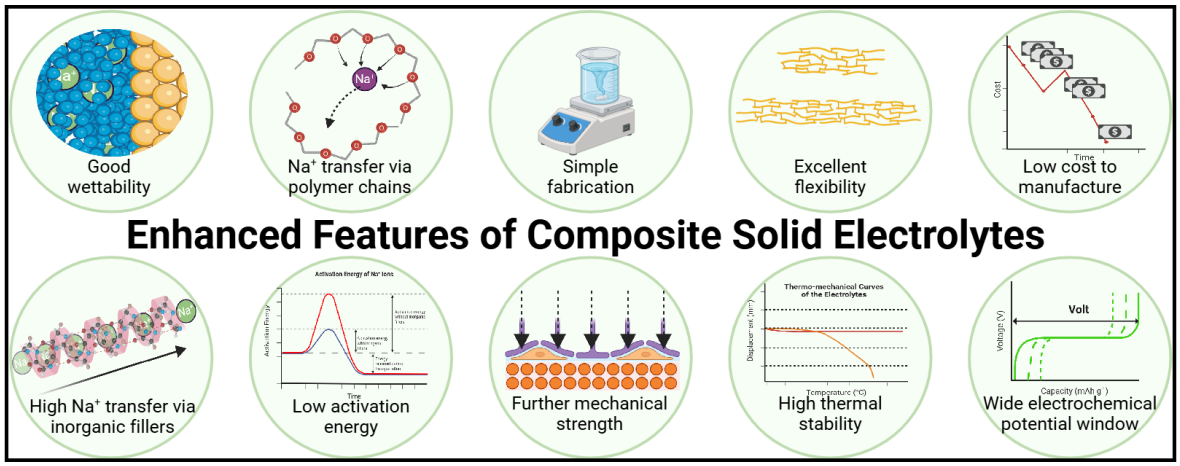

Figure 1.7. General characteristics of Composite Solid Electrolytes (CSEs).

Achieving the ionic conductivity of liquid electrolytes with ionic conductivities of 10^{-3} S cm^{-1}, NASICON-polymer composite electrolytes have a wide electromechanical voltage stability window (0 - 5 V) and enhanced thermal stability (from -40 °C to 150

°C) [65].

Many studies in the literature report that the ionic conductivity of NASICON polymer Na^+ ion composite solid electrolytes approaches the ionic conductivity of liquid electrolytes. Ran et al. report the ionic conductivity of the polymer-based composite electrolyte they produced as 4.13×10^{-4} S cm^{-1} at 30 °C [16]. Wang et al. doped the polymer-based ceramic composite electrolyte with Ce^{4+} and F^- ions and improved the ionic conductivity of the electrolyte to 1.07×10^{-3} S cm^{-1} at 25 °C. In addition, this electrolyte has a wide electrochemical stability window of 4.5 V [66]. Ruan et al. fabricate a flexible PVDF/$Na_3Zr_2Si_2PO_{12}$ composite polymer electrolyte membrane. Highlighting the contribution of the flexibility of the electrolyte to the contact on electrode surfaces, the researchers remark that the ionic conductivity is 1.07×10^{-4} S cm^{-1} at room temperature [47]. Neha and Dalvi manufacture a CSE by adding the PEO matrix with nano-sized $Na_3Zr_2Si_2PO_{12}$. The ionic conductivity increases by 2 orders of magnitude compared to the polymer electrolyte without $Na_3Zr_2Si_2PO_{12}$. Nano additives reduce the crystallinity of PEO and elevate the ionic conductivity [67]. Yu et al. add succinonitrile plasticizer to the composite electrolyte prepared using polyethylene glycol diacrylate as the polymer, sodium perchlorate as the sodium source, and NASICON as the inorganic filler. With the effect of plasticizer increasing the ionic conductivity, they achieve an ionic conductivity value of 4.50×10^{-4} S cm^{-1} at room temperature [68].

In Figure 1.8 the transport of Na^+ ions through ISE and SPE media and dendrite growths are represented. Na^+ ions are transferred in ISE with the help of inorganic fillers, whereas in SPE they are transferred by the movement of polymer chains. In ISE, the ion pathways are linear and represented with a dashed line. In SPE, the curved dashed lines indicate tortuous paths of ion transfer along the polymer chains. This difference symbolizes that the inorganic filler transfers Na^+ ions faster. Since the mechanical strength of ISEs is higher than SPEs, dendrite growth is suppressed in ISE. On the other hand, dendrite growth continues in SPE. Finally, the contact conditions at the SPE/electrode interface are much better than ISE/electrode contact conditions.

This leads to a decrease in the impedances encountered by ions in the SPE environment at the interfaces. Despite the excellent ionic conductivity and surface wettability of liquid electrolytes, solid electrolytes developed to replace liquid electrolytes have achieved the performance of liquid electrolytes in terms of ionic conductivity by strengthening with various additives.

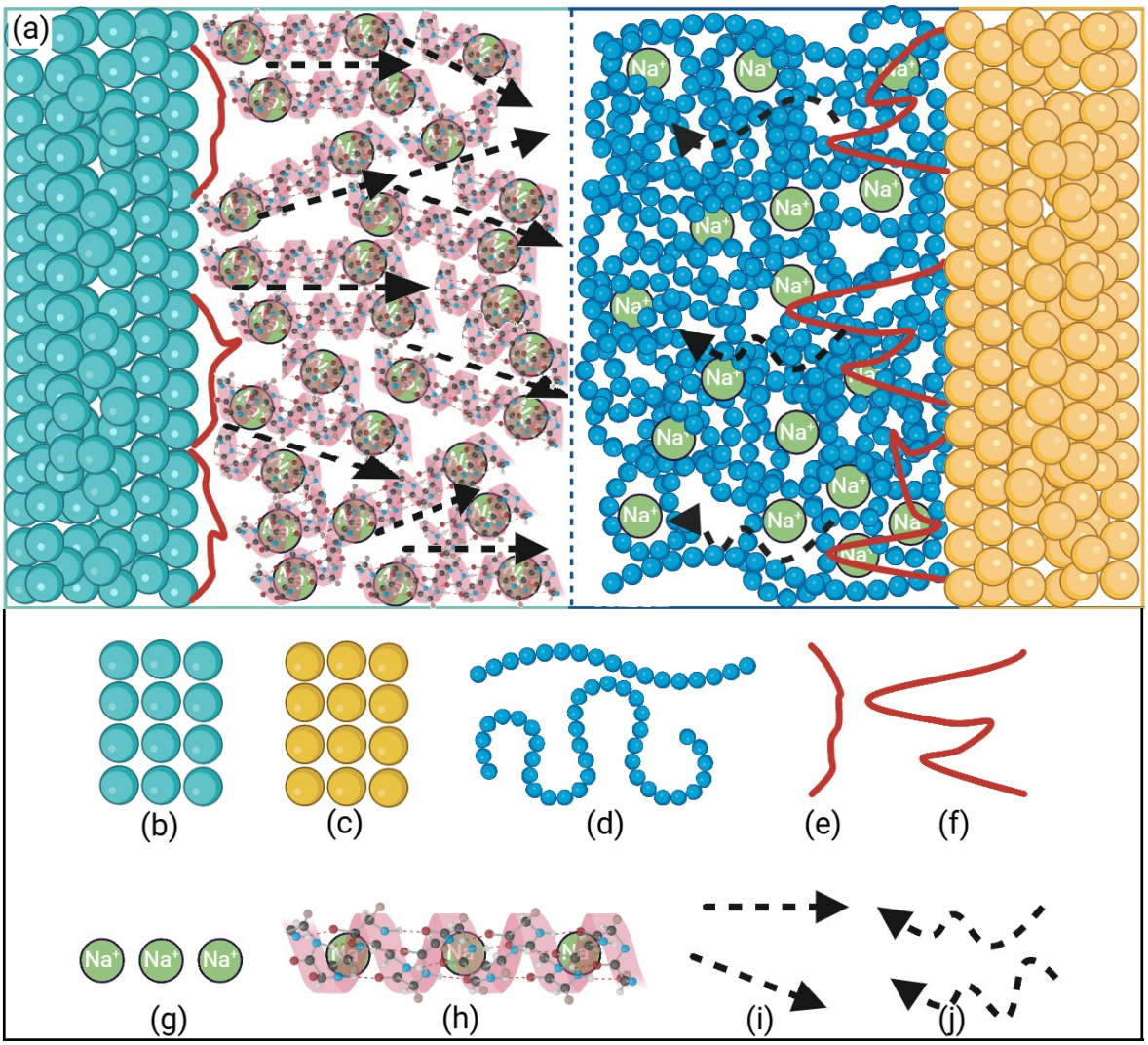

Figure 1.8. The representation of (a) Na^+ ion transfer and dendrite growths through ISE and SPE, (b) electrode for ISEs, (c) electrode for SPEs, (d) polymer chains, (e) suppressed dendrite, (f) developed dendrite, (g) Na^+ ions, (h) inorganic fillers and ion transport, (i) ion pathways across ISEs and (j) ion pathways across SPEs.

The ionic conductivity of solid electrolytes can be improved by using various additives. These additives enhance ionic conductivity and there is a growing body of literature on optimal composition ratios and suitable polymers for improving surface conditions. However, there are very few studies that investigate the contribution of the microstructure and mechanical properties of the electrolyte to the conductivity. In most studies of composite polymer electrolytes, the amount of inorganic filler to achieve optimum ionic conductivity was found to be 25 wt%, but the reason for this was not explained. Ions pass through electrolyte/electrode contact surfaces during charging and discharging. These surfaces are highly susceptible to mechanical effects. The mechanical structure of CSEs is also influenced by the compositional ratio of polymers and additives. The weight ratio of polymer and additives affects wettability, agglomeration and film thickness. Pressure and temperature can also contribute to ionic conductivity by mechanically improving the contact surface conditions as well as ionic mobility.

In the thesis study, the synthesis of CSE containing PEO, $NaClO_4$ and NASICON was carried out. The ideal mixing ratio of polymer and sodium salt in terms of ionic conductivity is determined. The ideal ratio of sodium and polymer was investigated. The contribution of different EO:Na^+ ratios to the ionic conductivity was investigated and the results were interpreted in terms of surface conditions. CSEs containing different weight ratios of NASICON were prepared and the ideal NASICON ratio was explored. The effect of different pressure levels on the ionic conductivity of electrolytes was investigated. The effects of preloading on the conductivity were studied, and the reasons for the mechanical improvements and deteriorations caused by preloading on the physical structure of the CSE thin film were revealed.

The weight ratio of inorganic fillers to be added to the SPE is optimized. XRD, SEM and FTIR studies are carried out for the characterization of the electrolyte. Potentiostatic tests are performed for its electrochemical performance. A test rig is designed and manufactured that can exert various levels of pressures and temperatures on the solid electrolyte. Activation energies of electrolytes at different temperatures

and composition ratios are determined. Experiments are carried out on the effect of temperature and pressure on ionic conductivity of CSE. A mechanism is proposed that explains how the pressure applied to the electrolyte alter interfacial conditions and increase ionic conductivities.

2. EXPERIMENTAL STUDY

The polymer-based NASICON-PEO composite electrolytes are manufactured using a solution casting method [69]. Polyethylene oxide (PEO, molecular weight $\approx 10^6$) and NASICON ($Na_3Zr_2Si_2PO_{12}$, 325 mesh) were purchased from MSE Supplies. Sodium perchlorate monohydrate ($NaClO_4$) was purchased from Merck and anhydrous acetonitrile (ACN) was purchased from Sigma Aldrich. No purification studies have been conducted on any of the chemicals. The amorphous structure of as received PEO can be seen in Figure 2.1 at different magnifications. The crystal structures of as received NASICON can be seen in Figure 2.2 at different magnifications.

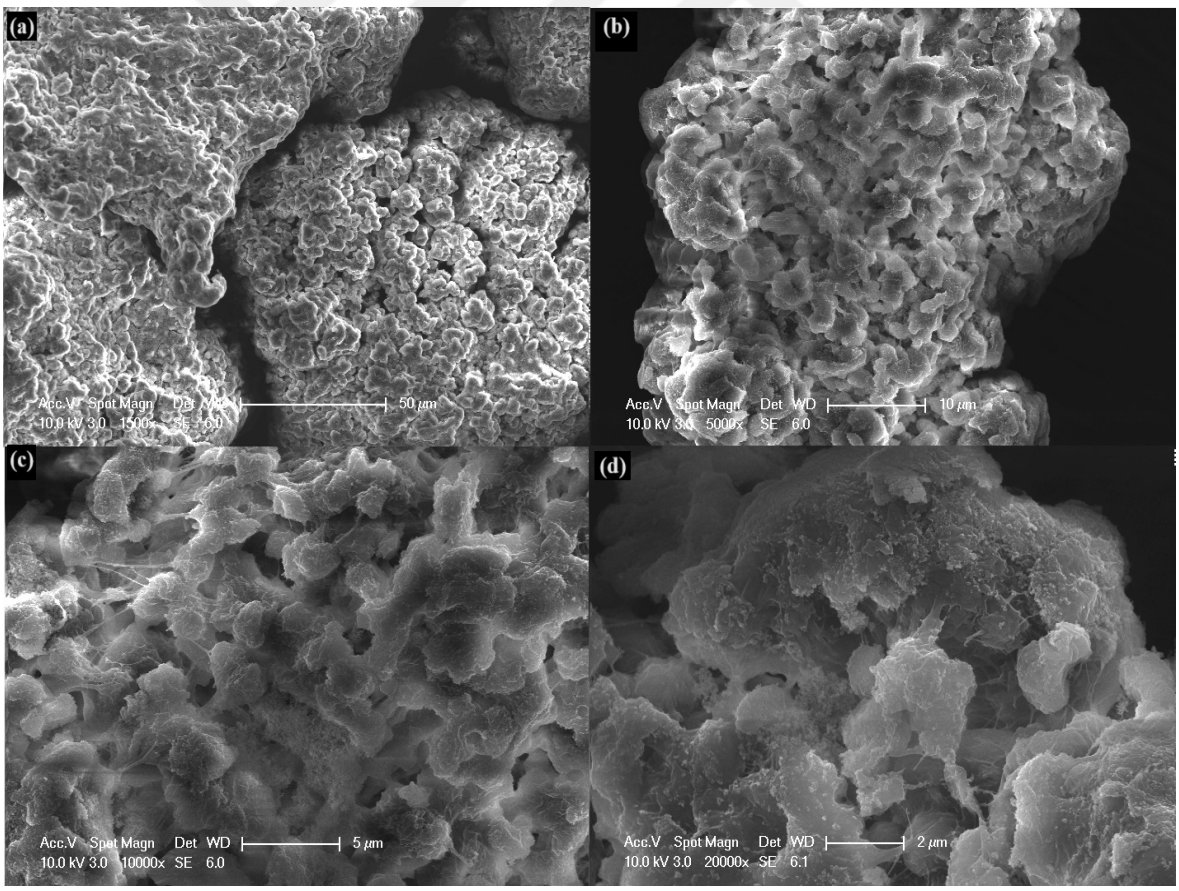

Figure 2.1. SEM images of as received PEO at (a) 1500 magnifications, (b) 5000 magnifications, (c) 10000 magnifications and (d) 20000 magnifications.

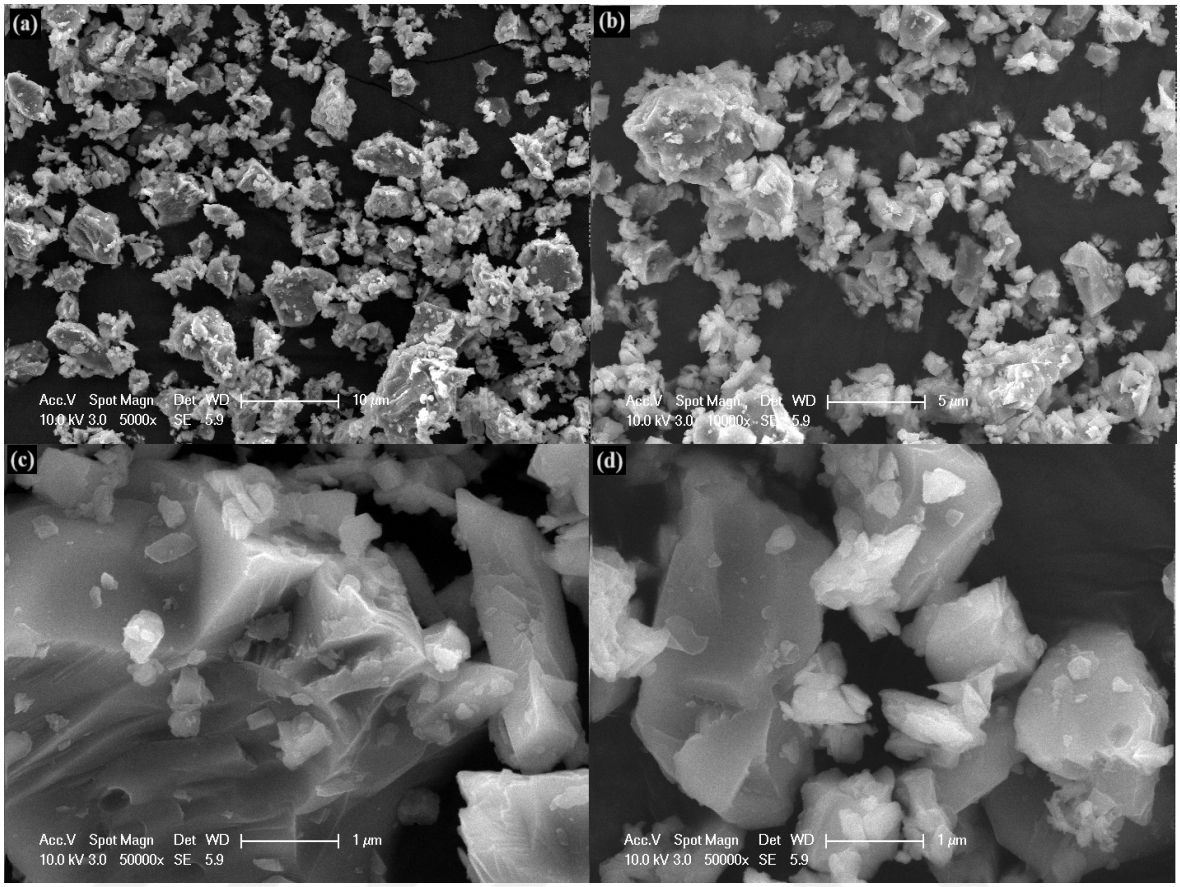

Figure 2.2. SEM images of as received NASICON at (a) 5000 magnifications, (b) 10000 magnifications, (c) 50000 magnifications and (d) 50000 magnifications.

2.1. Preparation of Solid Polymer Electrolytes (SPEs)

PEO and $NaClO_4$ were dried in a vacuum oven to remove moisture prior to mixing. PEO was dried at 50 °C and $NaClO_4$ was dried at 120 °C for 24 hours. The preparation process of SPE and CSE slurries and the equipment and methods used are illustrated in Figure 2.3.

PEO and $NaClO_4$ were dissolved in 50 mL of acetonitrile at different ratios of EO:Na^+ (10:1, 15:1, 20:1 and 25:1). The SPE with an EO:Na^+ ratio of 15:1 contained 2 g PEO and 0.371 g $NaClO_4$ [70]. The polymer and salt were mixed in a magnetic stirrer at room temperature until a homogeneous solution was obtained.

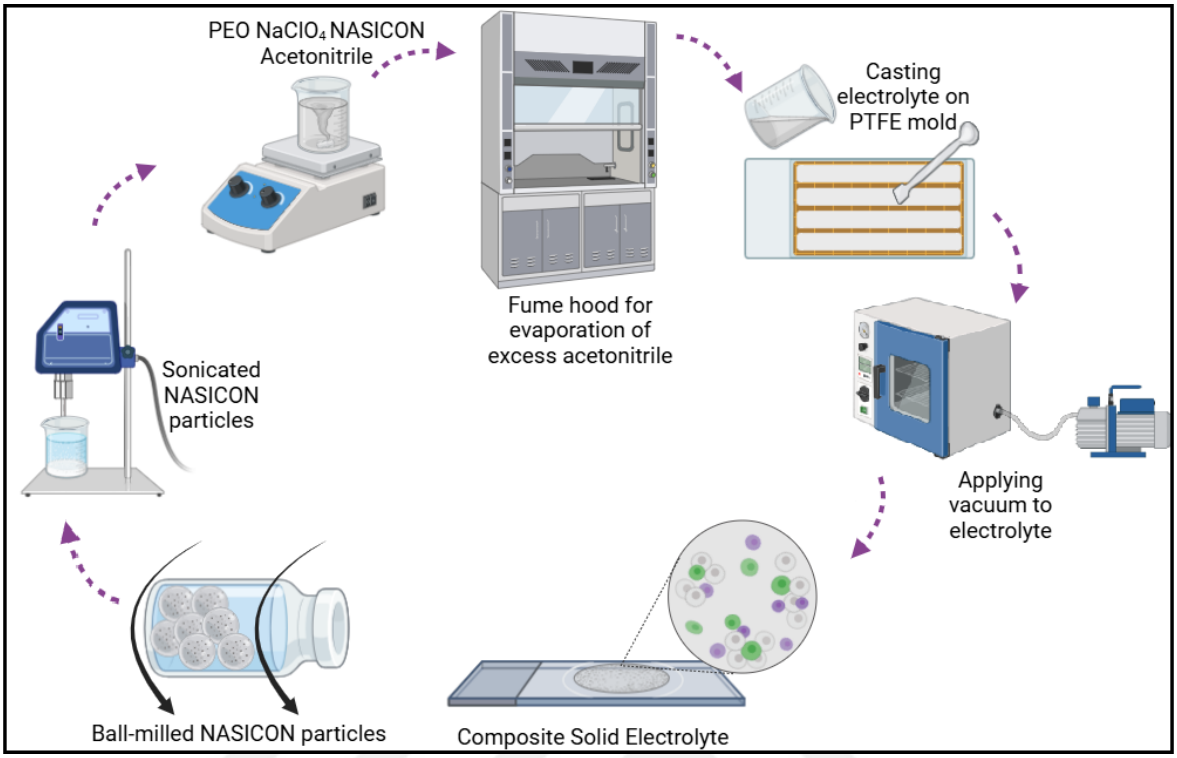

Figure 2.3. Schematic representation of the production process of the CSE.

The mixture was stirred for 5 hours on a magnetic stirrer under a fume hood to remove excess acetonitrile in the mixture. Since the total slurry volume was reduced to 20 mL, the electrolyte was largely free of acetonitrile. The SPE was stirred in a magnetic stirrer under a vacuum enclosure to remove air bubbles from the electrolyte slurry. Finally, the SPE slurry was poured into a mold made from PTFE tapes of 100 μm thick and kept at room temperature for solidification.

2.2. Preparation of NASICON-PEO Composite Solid Electrolytes (CSEs)

Initially, the size of NASICON particles was approximately 40 microns. However, the size of NASICON had to be reduced to nanoscale to increase ionic conductivity and improve interfacial contact. Therefore, NASICON was dispersed in acetonitrile and milled with zirconium balls in a roll mill machine.

The tube containing the solution was left one-third empty, one-third filled with 5 mm zirconia balls, and one-third filled with the solution. The critical speed formula was used for the speed of the tubes expressed as

$$N_c = 42.3 \times D^{-1/2}, \tag{2.1}$$

where N_c is the critical speed in rpm and D is the diameter of the tube in m. 75% of the value obtained from this formula was used [71].

At the end of 70 hours, the size of the NASICON particles was downsized to between 1 micron and 200 nm. The solution was sonicated in an ultrasonic mixer to prevent agglomeration of the NASICON particles and to evaporate the excess acetonitrile. It was then added to the PEO/$NaClO_4$ mixture, which was stirred in a magnetic stirrer for 24 hours. Composite polymer electrolyte samples with NASICON content of 20, 25, 30, 40 wt% were fabricated. The CSE slurry was placed in a fume hood to remove excess acetonitrile after obtaining a mixture in which the NASICON was well dispersed. The mixture was then poured into a PTFE mold and placed in a vacuum oven to remove air bubbles from the slurry. Finally, the CSE was placed in a glove box at room temperature.

2.3. Characterization of the CSEs

Scanning electron microscopy (SEM) and energy dispersive X-ray spectroscopy (EDX) were performed on a Thermo-Scientific Quattro S instrument for morphological and semi-quantitative analysis of SPEs and CSEs different weight percentage of NASICON.

X-ray diffraction (XRD) analyses of the chemical structure of CSEs containing different weight percentage of NASICON and SPEs were performed on Bruker D8 Discover XRD instrument using Cu-Kα irradiation as the photon source, a wavelength of 1.5418 Å, a voltage of 40 kV, and a current of 40 mA. All samples were analyzed at room temperature at 0.6 s time/step and 0.02° increment in the range of $2\theta = 3°$ - 90°.

Fourier Transform Infrared Spectroscopy (FTIR) analysis of CSEs was performed using a Thermo-Scientific Nicolet 380 spectrometer in the frequency range of 4000 to 500 cm^{-1}.

Electrochemical impedance spectroscopy (EIS) analysis of CSEs was performed with a Gamry Reference 3000 (Potentiostat/Galvanostat/ZRA) impedance meter under AC voltage of 50 mV. CSE films were placed between 10 mm diameter stainless steel rods and their impedance was measured at frequencies ranging from 1 MHz to 10 Hz.

Several equivalent circuit models, including resistance (R), capacitance (C), and constant phase element (CPE), were created using Gamry's Model Editor to model the Nyquist plots resulting from the EIS analysis. The Simplex Method from Gamry's Fitting Model tool was used for fitting.

The ionic conductivity of SPEs and CSEs is calculated by the following equation

$$\sigma_{ion} = t/(A_{contact}R), \tag{2.2}$$

where t and $A_{contact}$ represent the thicknesses of the SPEs and CSEs and the contact areas of the steel rods and electrolytes, respectively [72]. R represents the impedance obtained from the equivalent circuit modeling study.

The Arrhenius approach is used to calculate the activation energies of CSEs. The activation energy is calculated by the following equation

$$\sigma_{ion} = \sigma_0 exp(-E_A/(k_B T)), \tag{2.3}$$

where σ_{ion} is the Arrhenius pre-exponential factor, E_A is the activation energy, k_B is the Boltzman constant and T is the absolute temperature [73].

Impedance measurements were performed at temperatures ranging from 5 °C to 75 °C and pressures ranging from 60 kPa to 825 kPa. For temperature measurements, 15 minutes were allowed for temperature equilibration at each temperature change,

and for pressure measurements, 5 minutes were allowed at each step to stabilize the electrolyte/electrode surface contact.

For this research, a mechanism was designed to perform EIS measurements of CSEs under different temperature and pressure conditions. As shown in Figure 2.4, the pressure that is applied to the CSEs is controlled by a spring. The temperatures of the CSEs were controlled using a circulator.

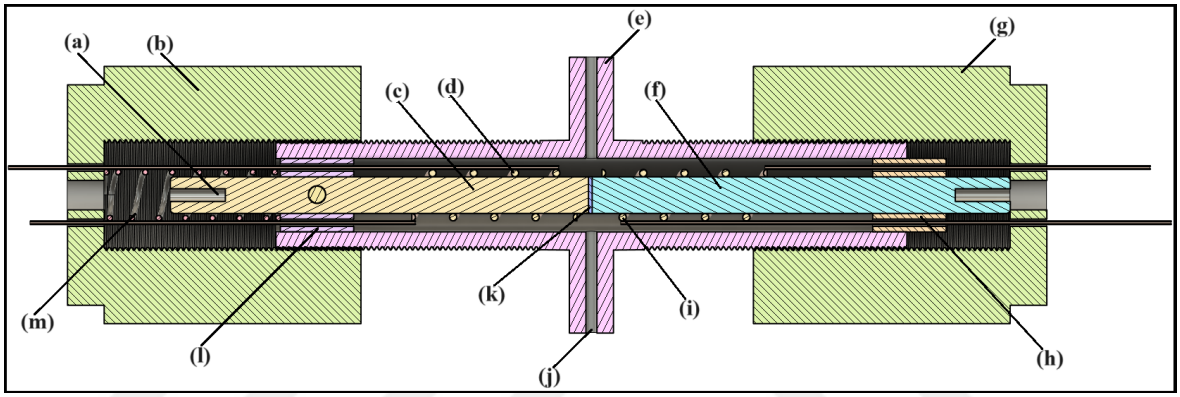

Figure 2.4. Cross-sectional view of the test rig. (a) Contact channel, (b) lid, (c) rod, (d) copper tube, (e) polyamide body, (f) rod, (g) lid, (h) centralizer, (i) copper tube, (j) probe channel, (k) CSE thin film, (l) centralizer, and (m) spring.

The contact surface for the probes of the potentiostat is the part marked with (a) in Figure 2.4. The lids of the device are indicated by (b) and (g). The temperature of the steel rods compressing the electrolyte is controlled by water supplied from a temperature controlled water bath and flowing through the copper tubes indicated by (d) and (i). The steel rods are indicated by (c) and (f). The body of the device is made of polyamide and is indicated by (e). The parts used to align the steel rods and to prevent them from slipping are indicated by (h) and (l). The channel in which the thermocouple probe is inserted to measure the temperature of the electrolyte is indicated by (j). CSE thin film is indicated by (k). The device is fixed with the lid indicated by (g) and the pressure is controlled by compression with the spring indicated by (m).

The pressure is increased by rotating the lids which have internal threads. The lids can move along the guide, which has external threads. As the lids move close to each other the springs of known spring constants are compressed and the pressure on the electrolyte can be controlled from the measured displacement.

The potentiostat and circulator connections for EIS measurements of CSE thin films at different temperatures are shown in Figure 2.5.

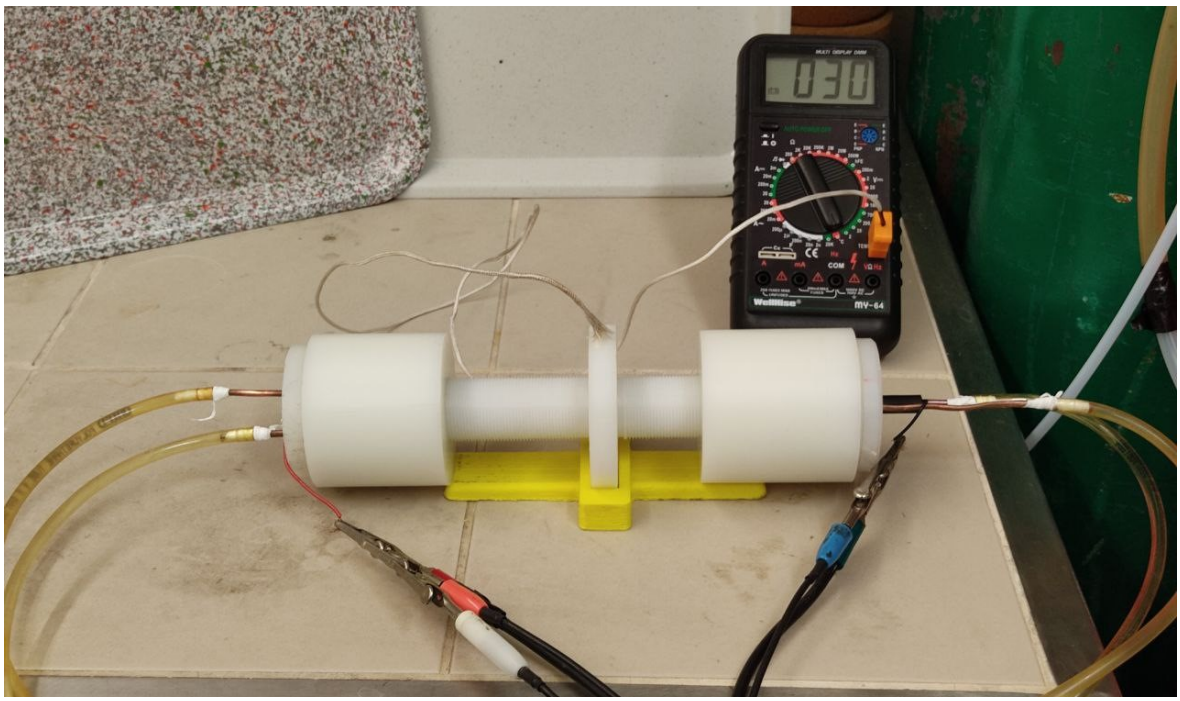

Figure 2.5. Representation of the test apparatus designed to measure impedance at different temperatures.

The temperature of the CSE thin film is monitored with the help of a thermocouple. The probe of the thermocouple is inserted along the channel on the test rig. This channel extends to the space where the steel rods compress the electrolyte. Thus, the temperature of the electrolyte is precisely determined. Figure 2.6 shows the parts of the test rig.

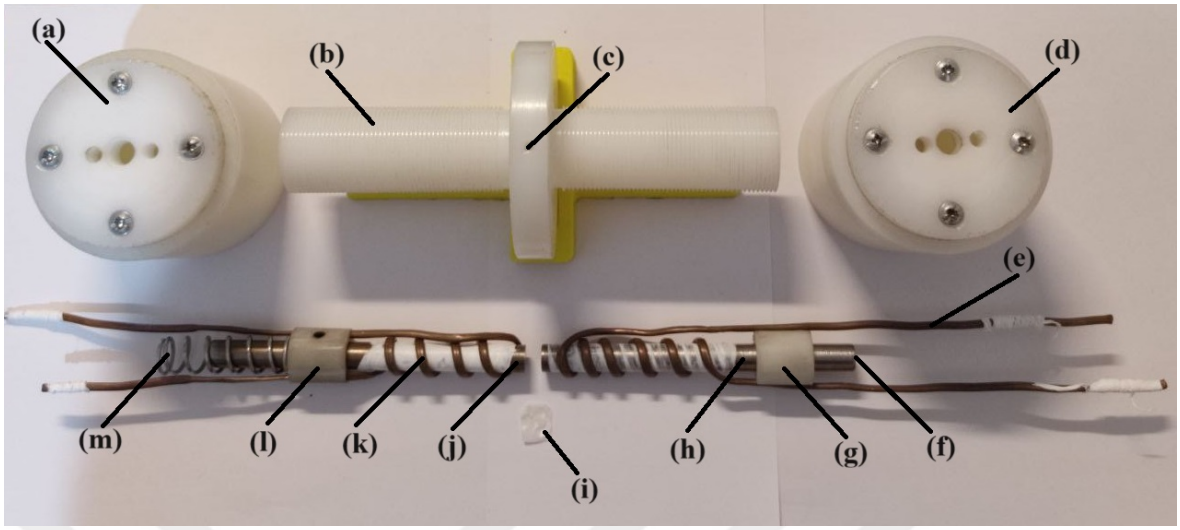

Figure 2.6. Disassembled view of the mechanical device. (a) Lid, (b) polyamide body, (c) probe channel (d) lid, (e) copper tube, (f) contact channel, (g) centralizer, (h) rod, (i) CSE thin film, (j) rod, (k) copper tube, (l) centralizer, and (m) spring.

3. RESULTS AND DISCUSSION

The EO:Na^+ ratio of PEO and $NaClO_4$ is an important parameter in the production of SPEs. Because EO:Na^+ ratio is highly effective on contact surface conditions and ionic conductivity. Ge et al. reported the optimum EO:Na^+ ratio as 20:1 in their polymer-based sodium ion electrolyte studies using NaTFSI salt as the ion source. Ni'mah et al. found the ideal EO:Na^+ ratio as 20:1 for polyethylene oxide based sodium ion solid polymer electrolyte with EO:Na^+ ratio of 10:1, 15:1, 20:1 and 30:1. Yu et al. also stated the EO:Na^+ ratio as 15:1 in composite polymer electrolyte in which they used sodium salt as the ion source. Zheng et al. reported the EO:Na^+ ratio as 16:1 in their fabricated SPE. Moreno et al. investigated the EO:Na^+ ratio in the SPE they fabricated in a wide range and expressed the ideal ratio as 20:1. Lee et al. prepared solid polymer electrolytes with EO:Na^+ ratios ranging from 10:1 to 30:1 and demonstrated that the best performance in terms of ionic conductivity was at an EO:Na^+ ratio of 20:1.

Therefore, in this study, SPEs with different EO:Na^+ ratios are fabricated and the optimal ratio is determined in terms of ionic conductivity and contact surface conditions. Figure 3.1 shows the ionic conductivity of SPEs with EO:Na^+ ratios of 10:1, 15:1, 20:1 and 25:1, as measured in this study. The best performing SPE in terms of ionic conductivity has an EO:Na^+ ratio of 15:1. The SPE with the highest ionic conductivity has an ionic conductivity of 4.15×10^{-6} S cm^{-1}. The ionic conductivity of the SPE thin film is in agreement with other studies in the literature. Mixing $NaClO_4$ and PEO at a ratio of 15:1 EO:Na^+, Ni'mah et al. obtained an ionic conductivity value of 1×10^{-5} S cm^{-1} [74] at 30 °C. Chandra et al. reported the highest ionic conductivity of solid polymer electrolytes prepared at different EO:Na^+ ratios as 7.07×10^{-7} S cm^{-1} [75]. Shindrov et al. measured the ionic conductivity of a solvent free PEO-$NaClO_4$ solid polymer electrolyte at 30 °C and stated it as 1×10^{-5} S cm^{-1} [76]. Kuila et al. evaluated the ionic conductivity of PEO and salt complex as 1.05×10^{-6} S cm^{-1} at room temperature [77].

While there is a 12% difference in ionic conductivity between an EO:Na^+ ratio of 10:1 and 15:1, there is a 75% drop in ionic conductivity from an EO:Na^+ ratio of 15:1 to 20:1.

When the ratio of EO:Na^+ increased from 20:1 to 25:1, the ionic conductivity continued to decrease. The rate of decrease in ionic conductivity was 20% when the EO:Na^+ ratio increased from 20:1 to 25:1. In conclusion, among the EO:Na^+ ratios, the most ideal EO:Na^+ ratio in terms of ionic conductivity is 15:1.

As the EO:Na^+ ratio decreases from the optimum 15:1 to 10:1, the $NaClO_4$ content in the SPE increases and the crystallinity of the electrolyte decreases. The electrolyte sticks to the stainless steel surface serving as the electrode and folds over, increasing the impedance and decreasing the ionic conductivity. It is observed that as the EO:Na^+ ratio increases, the SPE becomes more flexible and forms a good contact surface with the electrodes. Nevertheless, when the EO:Na^+ ratio reaches 25:1, the SPE becomes more rigid, the electrolyte does not adhere to the stainless steel electrodes, and the contact surface deteriorates, increasing the impedance at the interface and reducing the ionic conductivity to 18% of the optimum value.

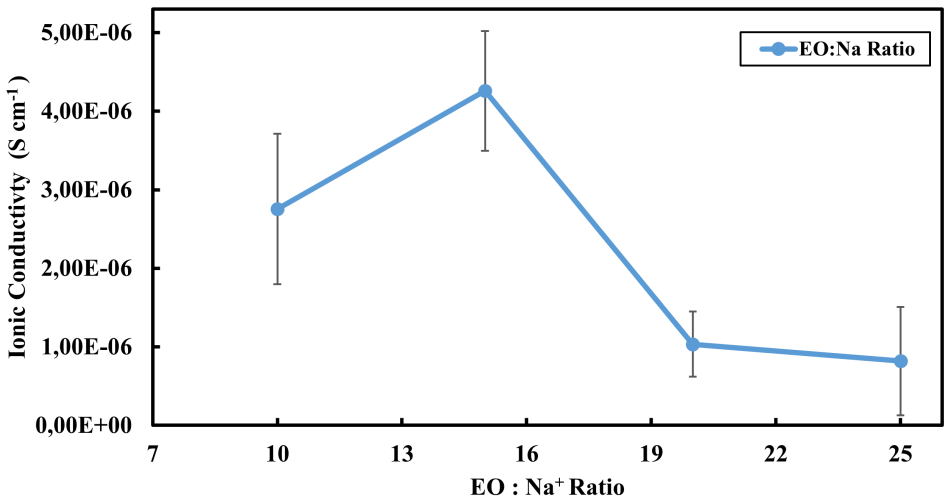

Figure 3.1. The ionic conductivity of SPEs with various EO:Na^+ ratios at room temperature.

Figure 3.2 demonstrates the SEM image of the surface of SPE containing PEO and 15.6 wt% $NaClO_4$. PEO with $NaClO_4$ decreased the crystalline regions and increased the amorphous regions in the polymer matrix. Sodium perchlorate is well dispersed in the polymer matrix, as shown in Figure 3.2a. Sodium salts added to the semi-crystalline structure of PEO disrupt the crystalline structure, causing an increase in the density of amorphous regions. This contributes to the ion mobility in the polymer.

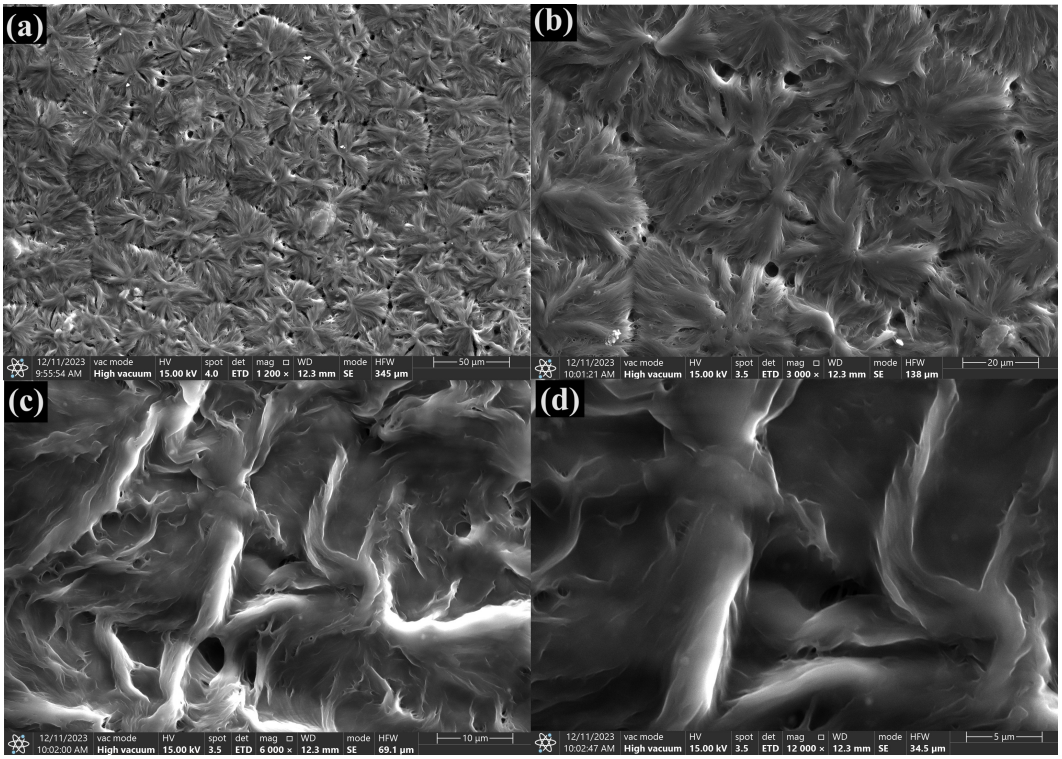

Figure 3.2. SEM images of SPE (PEO and 15.6 wt% $NaClO_4$) at (a) 1200 magnifications, (b) 3000 magnifications, (c) 6000 magnifications and (d) 12000 magnifications.

3.1. Effects of Ball-Milling on Conductivity and Surface Condition of CSE

PEO and $NaClO_4$ dissolve in acetonitrile but NASICON does not. Therefore, NASICON must be well-dispersed in CSE for high ionic conductivity [72]. Reducing the particle size is a suitable method to make NASICON well-dispersed both on the electrolyte surface and in the electrolyte cross-section. NASICON was ball milled for

70 hours to reduce its particle size. Figure 3.3 shows SEM images of the surface of CSE containing 25 wt% NASICON that has not been ball-milled. NASICON crystals are not homogeneously dispersed and are agglomerated in certain places.

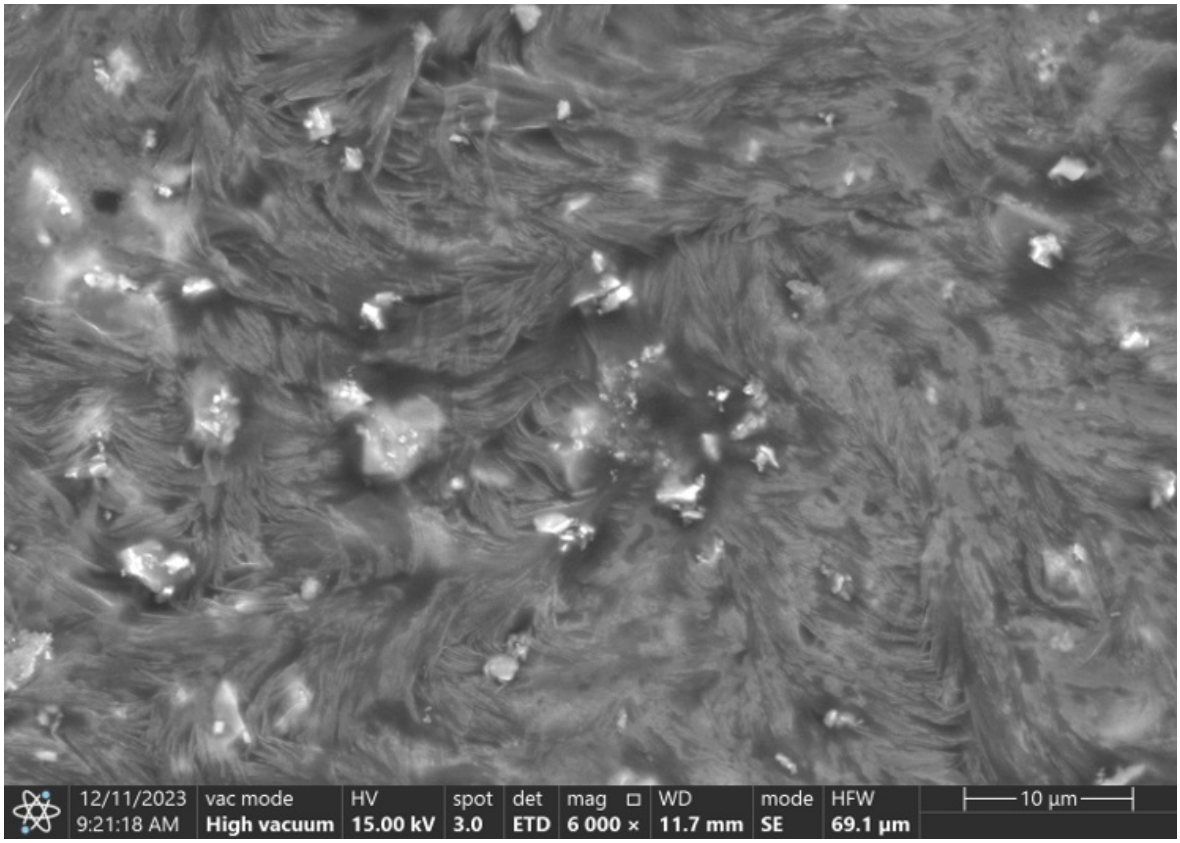

Figure 3.3. SEM images of the surface of CSE 25 wt% NASICON before ball-milling.

Figure 3.4 shows the elemental analysis of CSE containing 25 wt% NASICON that has not been ball-milled. Carbon, shown in green, is predominantly from PEO and is distributed throughout the electrolyte (Figure 3.4a). According to the results of the elemental analysis performed on the surface of the CSE thin film containing 25 wt% NASICON before grinding in the ball-mill, the carbon content of the electrolyte was measured as 35.7 wt%. The weight ratio of oxygen, another element of polyethylene oxide chains, on the electrolyte surface was found to be 42.7 wt%. Therefore, the polymer constitutes 78.4 wt% of the CSE thin film. Figure 3.4a and Figure 3.4b demonstrate that the polymer matrix covers the entire surface of the composite solid electrolyte. In Figure 3.4b, it can be seen that NASICON disperses into the poly-

mer matrix and distorts the semi-crystalline structure of the polymer, increasing the amorphous regions.

The zirconium and silicon atoms shown in yellow and pink, respectively, are from NASICON (Figure 3.4b). In addition to these, sodium and phosphorus are other elements in the structure of NASICON. According to the results of the elemental analyses, the weight percentage of these four elements is 16.4. Considering that the weight percentage of NASICON in the composite solid electrolyte is 25 percent, it is apparent that 16.4 percent of NASICON is well dispersed on the surface of the electrolyte. Figure 3.4b displays that NASICON is well dispersed on the surface of the composite electrolyte.

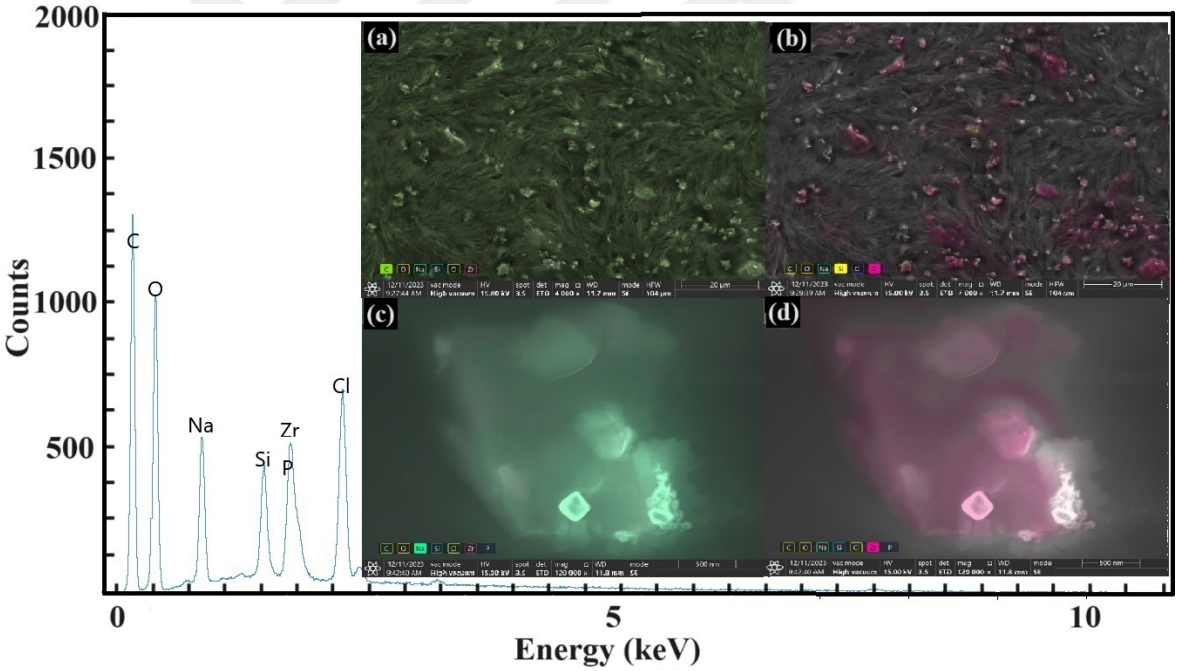

Figure 3.4. EDX analysis of the surface of CSE 25 wt% NASICON before ball-milling in terms of (a) oxygen, (b) zirconium and silicon, (c) sodium and (d) zirconium.

Sodium crystals appear turquoise green in Figure 3.4.c and zirconium crystals appear pink in Figure 3.4.d. Accordingly, NASICON crystals, the source of zirconium, remained much larger than sodium. This prevents NASICON from being uniformly distributed throughout the electrolyte cross section.

Figure 3.5 shows a cross-section of a CSE containing NASICON an average particle size of 44 microns. According to SEM analysis of the surface and cross-section of the electrolyte, the size of the NASICON particles varies between 30 microns and 55 microns.

Elemental analysis is carried out to determine the distribution of NASICON particles along the cross-section of the composite solid electrolyte. Silicon, one of the elements contained in NASICON, is selected for elemental analysis. The results are evaluated on the basis of the distribution of the silicon on the surface of the composite electrolyte and in the inner region. According to the results of the elemental analysis, the weight ratio of NASICON particles at two points on the surface of the composite electrolyte was measured to be 0.8 wt% and 0.5 wt%. However, it was not possible to observe any NASICON particles in the cross section of the composite electrolyte. According to the elemental analysis carried out near the surface of the composite solid electrolyte, the sodium element content of the electrolyte is 1.6 wt%. In the centre of the cross-section of the electrolyte, no sodium element can be detected. Therefore, it can be concluded that sodium perchlorate and NASICON cannot reach the middle regions of the electrolyte based on the elemental analysis results on the surface of the composite solid electrolyte.

Therefore, NASICON with an average particle size of 44 microns remained on the surface of the composite electrolyte as it was added to the mixture of PEO, $NaClO_4$ and acetonitrile without grinding.

As can be seen from the SEM image, the NASICON crystals were unable to disperse evenly throughout the polymer matrix and agglomerated in the top layer. The thickness of the CSE thin film is approximately 100 microns. Since the unground NASICON particles remain on the upper surface of the composite solid electrolyte, there are large deviations in the film thickness of the electrolyte. Variable film thickness provides insufficient contact area at electrolyte/electrode interfaces. This increases the impedance and leads to a decrease in ionic conductivity.

As a result, unmilled NASICON causes deviations in the film thickness of the electrolyte, cannot be well-dispersed across the electrolyte cross-section and causes an impedance increase. It accumulates on the surface and prevents the complexation of polymer and sodium perchlorate.

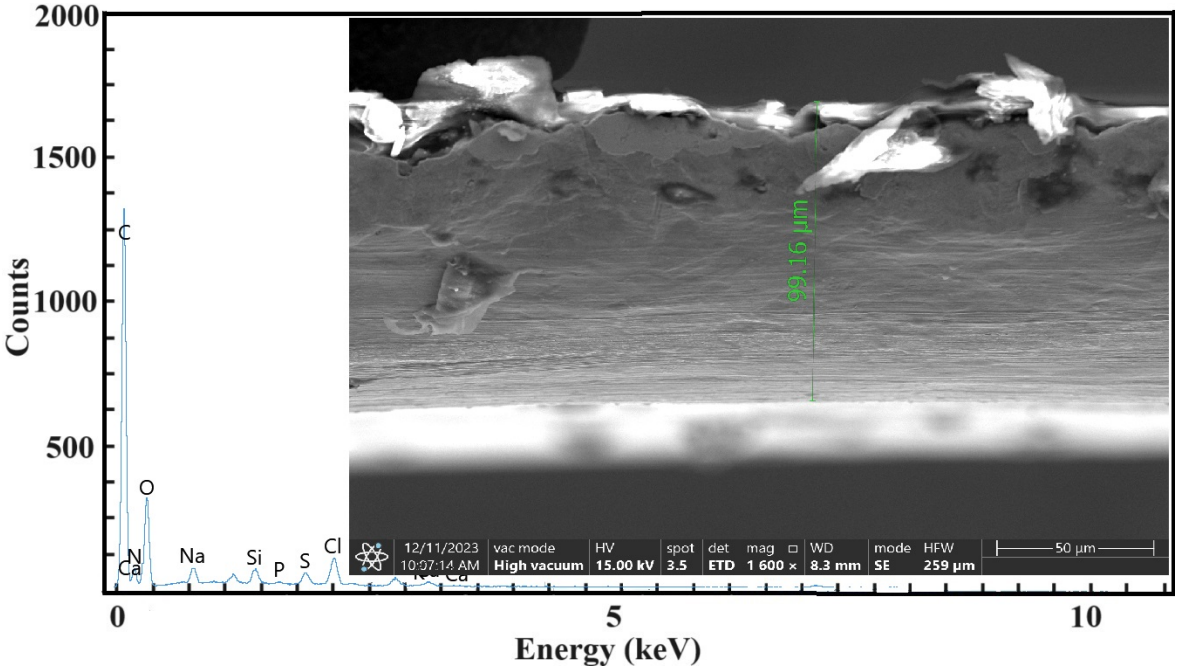

Figure 3.5. Cross-sectional view of CSE containing 25 wt% NASICON before ball-milling.

NASICON crystals are ball-milled to reduce the particle size. As can be seen in the surface images taken from different regions in Figure 3.6, reducing the particle size resulted in a more homogeneous distribution of the crystals along the CSE surface. NASICON particles were ground for 70 hours using zirconium balls in tubes filled with acetonitrile. After grinding, a reduction of up to 95% in the particle size of NASICON was observed. This reduction reduced the particle size of NASICON from microns to nanometres. As a result, the electrolyte acquired the character of a nanocomposite. Nano-sized NASICON particles contributed to the ionic conductivity by increasing the amorphous regions of the electrolyte. In addition, NASICON particles below 1 micron in size were better distributed throughout the electrolyte, which improved ionic conductivity.

Figure 3.7 shows the elemental analysis of CSE containing 25 wt% NASICON that has been ball-milled. Oxygen, shown in yellow, is predominantly from PEO (Figure 3.7a). The sodium atom shown in green is from both $NaClO_4$ and NASICON (Figure 3.7b). The zirconium and silicon shown in Figure 3.7c and Figure 3.7d are from NASICON only. As can be seen from the SEM image, they are homogeneously dispersed throughout the electrolyte compared to unground NASICON.

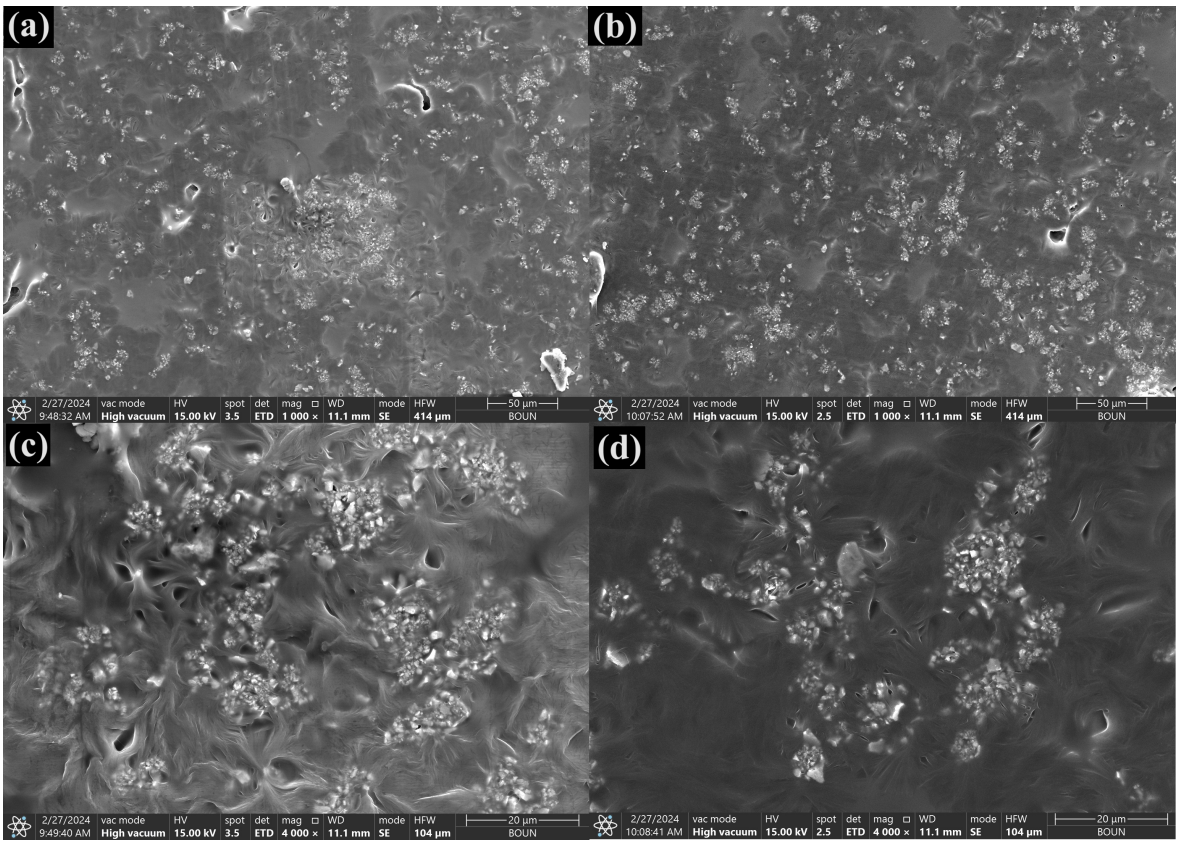

Figure 3.6. SEM images of the surface of CSE 25 wt% NASICON after ball-milling at (a) 1000 magnifications, (b) 1000 magnifications, (c) 4000 magnifications and (d) 4000 magnifications.

After 70 hours of ball-milling, the size of NASICON was reduced to between 1 micron and 200 nm (Figure 3.8). Grinding and homogeneous distribution of NASICON into the polymer also reduced the thickness of the CSE by 20% to 80 microns (Figure 3.9). EDX analysis of the CSE cross section based on measurements taken from two points and one region showed that the weight percentages of zirconium were 35.7, 19.3,

11.1 at the surfaces and mid-region, respectively. These results indicate that the milled NASICON in the electrolyte concentrates at the upper and lower surfaces (Figure 3.10).

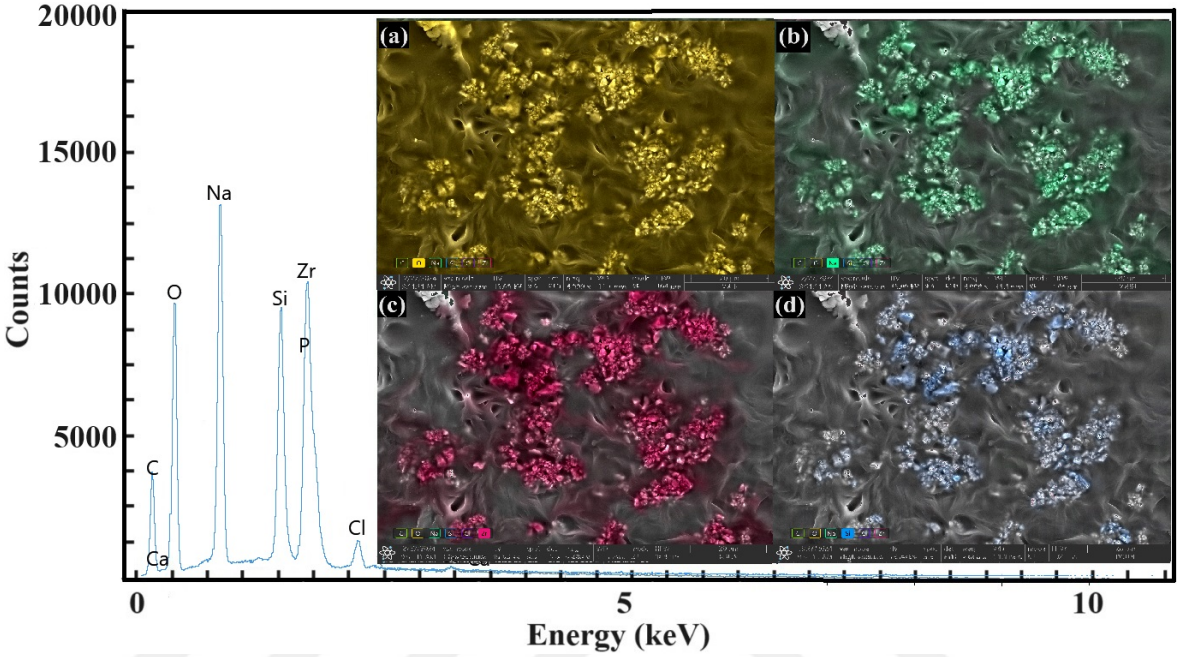

Figure 3.7. EDX Analysis of the surface of CSE 25 wt% NASICON in terms of (a) oxygen, (b) sodium, (c) zirconium and (d) silicon.

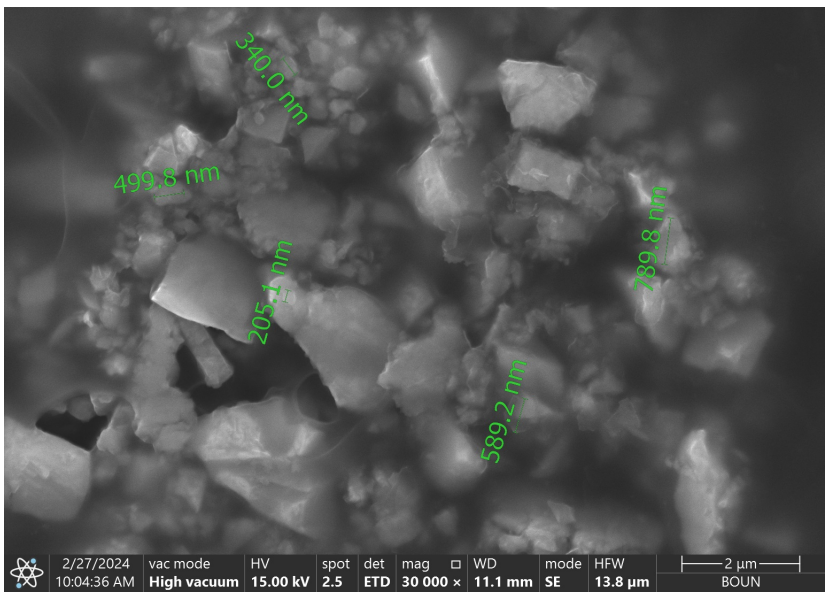

Figure 3.8. Particle size of NASICON after 70 hours ball-milling.

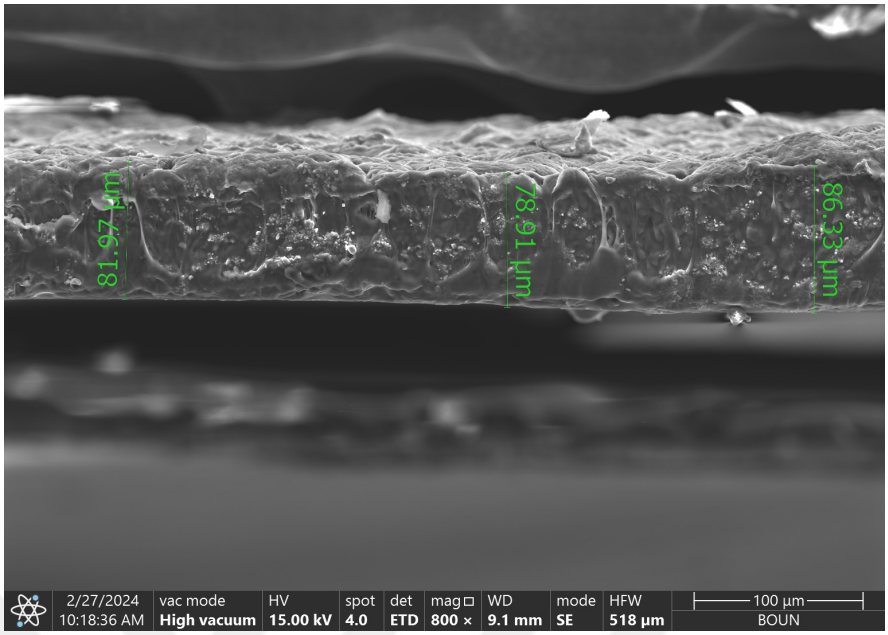

Figure 3.9. Cross-sectional view of CSE containing 25 wt% NASICON after ball-milling.

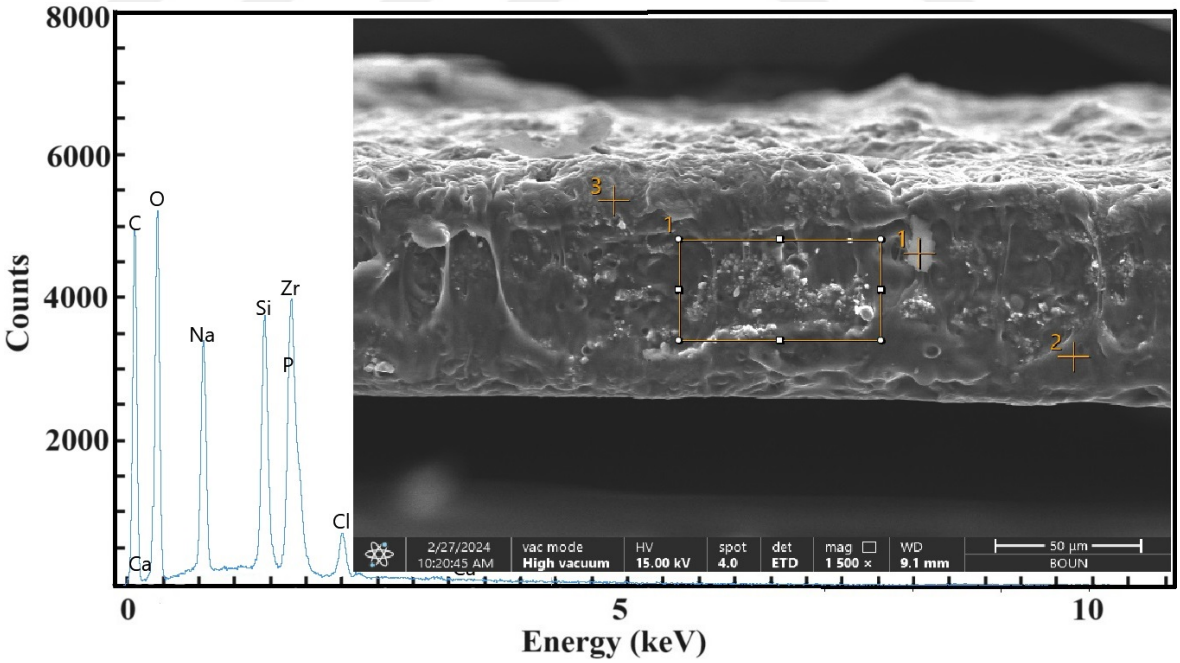

Figure 3.10. Cross-sectional view of CSE containing 25 wt% NASICON after ball-milling at 1500 magnification showing the locations of two points and one region where the weight percentages of zirconium are shown.

3.2. Effects of the Weight Percent of NASICON on Ionic Conductivity

Effects of the weight percent of NASICON on ionic conductivity is analyzed with EIS measurements. NASICON is added to the SPE at an EO:Na^+ ratio of 15:1 at 20, 25, 30 and 40% by weight. The ionic conductivities of the CSE containing different proportions by weight of NASICON have been measured at 30 °C, 45 °C, 60 °C and 75 °C. SEM/EDX analysis has been performed to determine the effect of varying amounts of NASICON on the microstructure of the electrolyte.

Figure 3.11 demonstrates the ionic conductivities of CSEs containing different amounts of NASICON at various temperatures ranging from 30 °C to 75 °C. According to this graph, the CSE containing 25 wt% NASICON performed better in terms of ionic conductivity at all temperatures tested. The ionic conductivity of CSE thin film containing 25 wt% NASICON was measured as 5.19×10^{-5} S cm^{-1} and 3.64×10^{-4} S cm^{-1} at 30 °C and 75 °C, respectively.

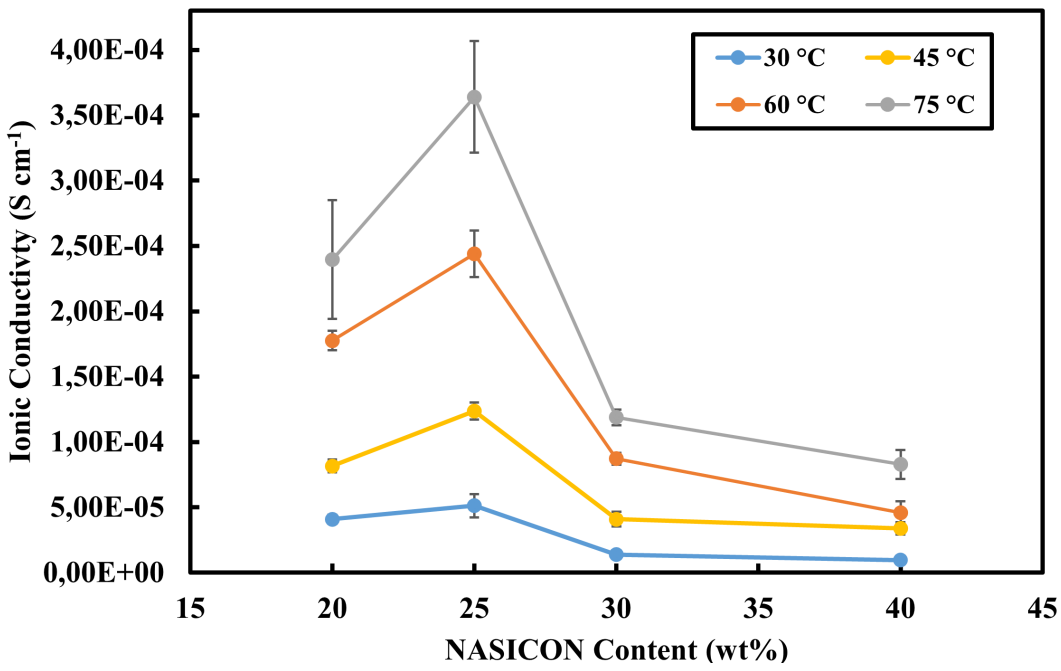

Figure 3.11. Ionic conductivity of CPE with different NASICON content at different temperatures.

The ionic conductivity of CSE thin films is consistent with other studies in the literature. Goodenough et al. presented the ionic conductivities of composite polymer electrolyte containing NASICON at 30 °C and 75 °C as 2.1×10^{-5} S cm^{-1} and 7.8×10^{-4} S cm^{-1} [20]. Shindrov et al. reported the ionic conductivity of the composite solid electrolyte prepared at different NASICON ratios as 3.56×10^{-5} S cm^{-1} at 30 °C [76]. Wang et al. reported the ionic conductivity of NASICON containing composite solid electrolyte as 1.4×10^{-4} S cm^{-1} at room temperature [42]. Singh et al. measured the ionic conductivity of nanocomposite solid electrolytes containing PEO, NaI and NASICON as 4×10^{-5} S cm^{-1} at 40 °C [78]. Ran et al. calculated the ionic conductivity of composite solid electrolyte containing scandium and germanium doped NASICON as 4×10^{-5} S cm^{-1} at 30 °C [40].

A decrease in ionic conductivity is observed at 30 and 40 wt% NASICON at all temperatures. This decrease is more prominent at higher temperatures. As the temperature of the electrolyte increases, the activation energy of the ions decreases and the ionic conductivity rises as the energy required for the ions to move decreases [79]. The high NASICON percentage had an adverse effect on the ionic conductivity. Increasing the amount of NASICON too much raised the concentration of sodium in the electrolyte to excessive levels. As the temperature increased, more sodium ions mobilized with less energy, but their movement was hindered by the density. This raises the impedance and lowers the ionic conductivity. Another negative effect is due to grain boundaries [80]. The abundance of NASICON crystals increased the number of grain boundaries through which the sodium ions had to pass, creating a large impedance.

The effect of weight percent NASICON on the microstructure of CSE thin films can be observed by SEM/EDX analysis. The elemental composition of each CSE's top and bottom surfaces and the middle region is analyzed to determine the weight ratio of NASICON using zirconium. Figure 3.12, Figure 3.13, and Figure 3.14 shows the SEM images of NASICON crystals are dispersed along the cross sections of CSE films containing 20%, 25% and 30% NASICON.

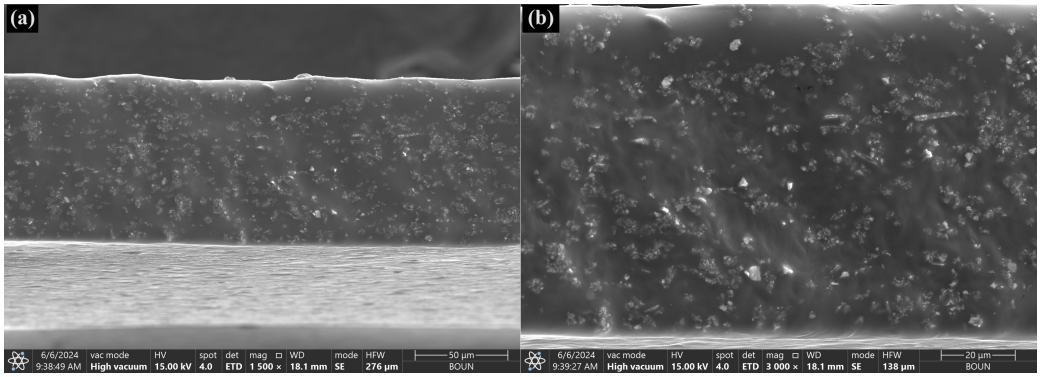

Figure 3.12. Cross-sectional image of CSE containing 20 wt% NASICON at (a) 1500 magnifications and (b) 3000 magnifications.

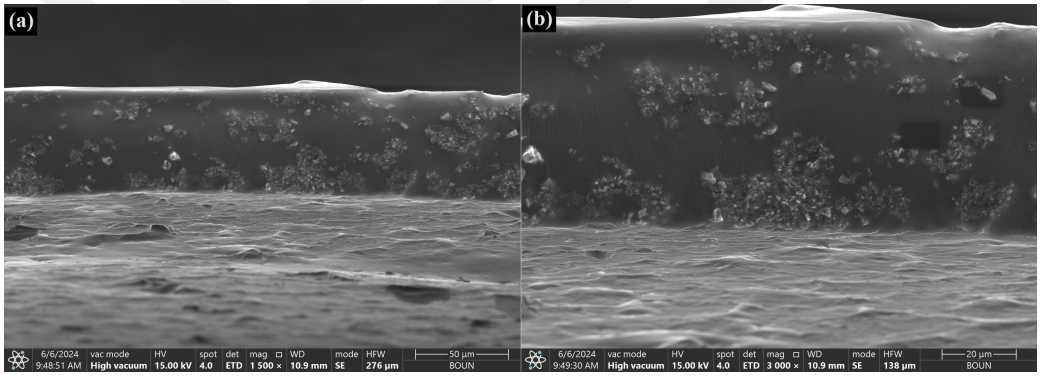

Figure 3.13. Cross-sectional image of CSE containing 25 wt% NASICON at (a) 1500 magnifications and (b) 3000 magnifications.

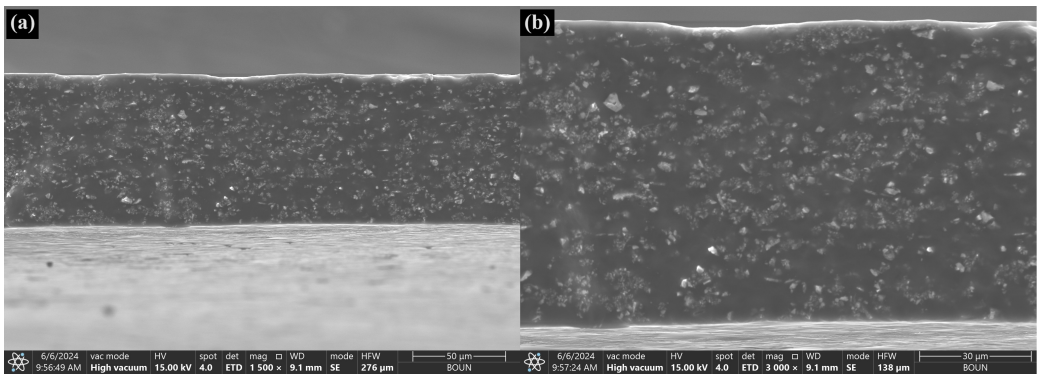

Figure 3.14. Cross-sectional image of CSE containing 30 wt% NASICON at (a) 1500 magnifications and (b) 3000 magnifications.

The EDX results reveal that the optimal distribution of NASICON on the top and bottom surfaces as well as in the middle region of the CSE is found in the electrolyte containing 25% NASICON by weight (Table 3.1). The amount of NASICON in the middle region of the CSE containing 20 wt% NASICON is 8 wt%, while the amount of NASICON in the middle region of the CSE containing 30 wt% NASICON is 10 wt%.

Additionally, the Zr content in the middle region of the CSE containing 40% NASICON is 27.7%. Except for the 25% CSE thin film, the distribution concentration of Zr in the other samples was insufficient in the middle regions of the electrolyte. There are two reasons why the NASICON ratios in the middle regions of composite solid electrolytes containing 20, 30 and 40 wt% NASICON are not satisfactory. The first of these is that the film could not be well dispersed on the surface of the electrolyte and could not penetrate into the inner regions because the 20 wt% NASICON ratio was insufficient. The second reason is that agglomerations increase as the NASICON ratio increases above 25 per cent. This increase causes NASICON to accumulate on the surface of the electrolyte, not well-dispersed and therefore not well-dispersed towards the inner regions of the electrolyte.

Table 3.1. Percentage by weight of NASICON in the top, bottom and middle regions.

		Top Surface (wt%)	Middle Region (wt%)	Bottom Surface (wt%)
NASICON ratio by weight (wt%)	20	22	8	19.4
	25	24	15	22.8
	30	32.8	9.8	25.3
	40	37.2	27.7	50.4

As can be seen from Figure 3.15, NASICON crystals in the 40% CSE thin film are agglomerated because of the high weight percentage of NASICON crystals and nano-sized particles. These local clusters increased the impedance by increasing grain boundaries, making it difficult for ions to pass through. Moreover, these accumula-

tions in various regions throughout the film caused significant variations in film thickness, leading to a decrease in ionic conductivity due to incomplete contact at the electrolyte/electrode interfaces.

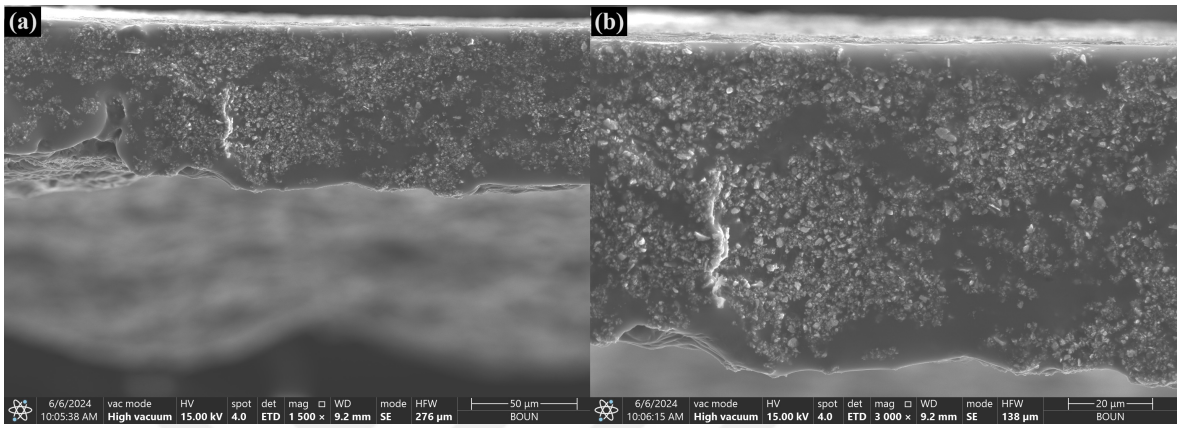

Figure 3.15. Cross-sectional image of CSE containing 40 wt% NASICON at (a) 1500 magnifications and (b) 3000 magnifications.

The ionic conductivity of the composite solid electrolyte containing 40 wt% NASICON decreased from 1.23×10^{-4} S cm^{-1} to 3.42×10^{-5} S cm^{-1} at 30 °C. The rate of decrease in ionic conductivity is 72%. This rate increased with increasing temperature and reached 77% at 75 °C.The activation energy of sodium ions decreases with increasing temperature. Ions with decreasing activation energy migrate more with less energy. However, highly agglomerated NASICON particles prevent the passage of ions. Thus, there is a significant increase in sodium concentration. The agglomeration of nano-sized NASICON crystals leads to local thickness increases and with increasing density of inorganic fillers there is an increase in the number of grain boundaries. This leads to high impedance at the grain boundaries and highly reduces the ionic conductivity.

Figure 3.16 shows the thickness measurements at various locations made on CSE films containing various amounts of NASICON. According to Table 3.2, which shows the thickness measurements, the thinnest film is with 25% NASICON additive. Furthermore, low standard deviation in the thickness measurements show that a more uniform thickness can be obtained with lower NASICON content.

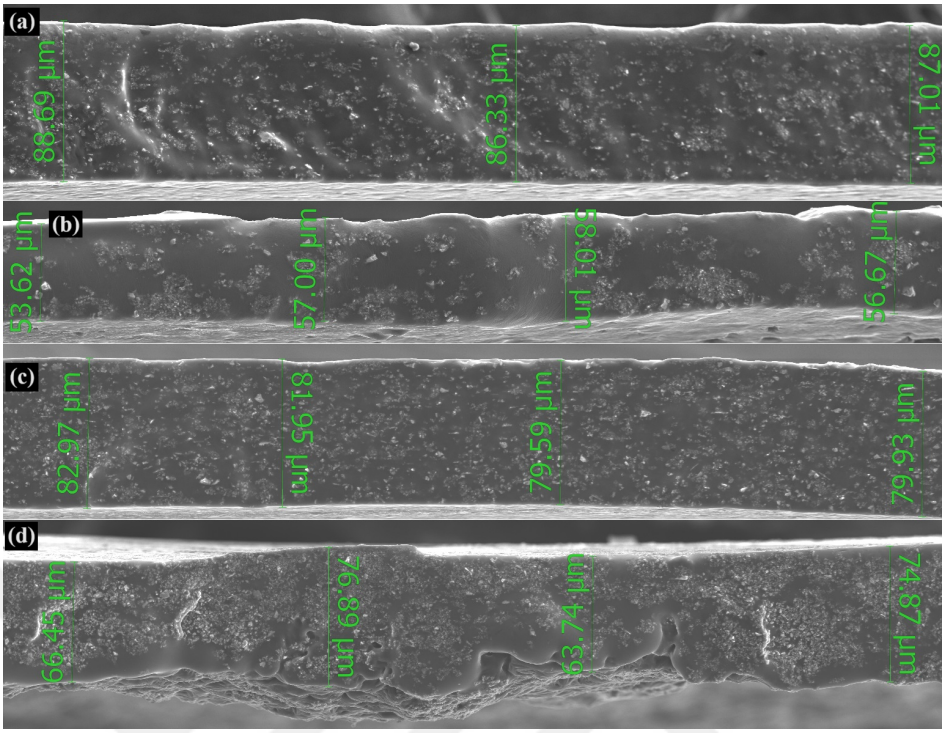

Figure 3.16. Thickness of CSE thin films with (a) 20 wt% NASICON, (b) 25 wt% NASICON, (c) 30 wt% NASICON and (d) 40 wt% NASICON.

Table 3.2. Average, maximum, minimum thickness and standard deviation of films.

		Average Value (μm)	Maximum Value (μm)	Minimum Value (μm)	Standard Deviation (σ)
NASICON ratio by weight (wt%)	20	87.34	88.69	86.33	0.99
	25	56.32	58.01	53.62	1.64
	30	81.11	82.97	79.59	1.41
	40	70.49	76.89	63.74	5.52

3.3. XRD Studies of the CSE Thin Films

EDX information on the elemental composition of the electrolyte is confirmed by XRD analysis. Figure 3.17 indicates the characteristic peaks of PEO, $NaClO_4$ and NASICON. $NaClO_4$ and NASICON contain many more peaks than PEO due to

their crystalline structure. Since PEO is semi-crystalline, it contains fewer peaks than $NaClO_4$ and NASICON.

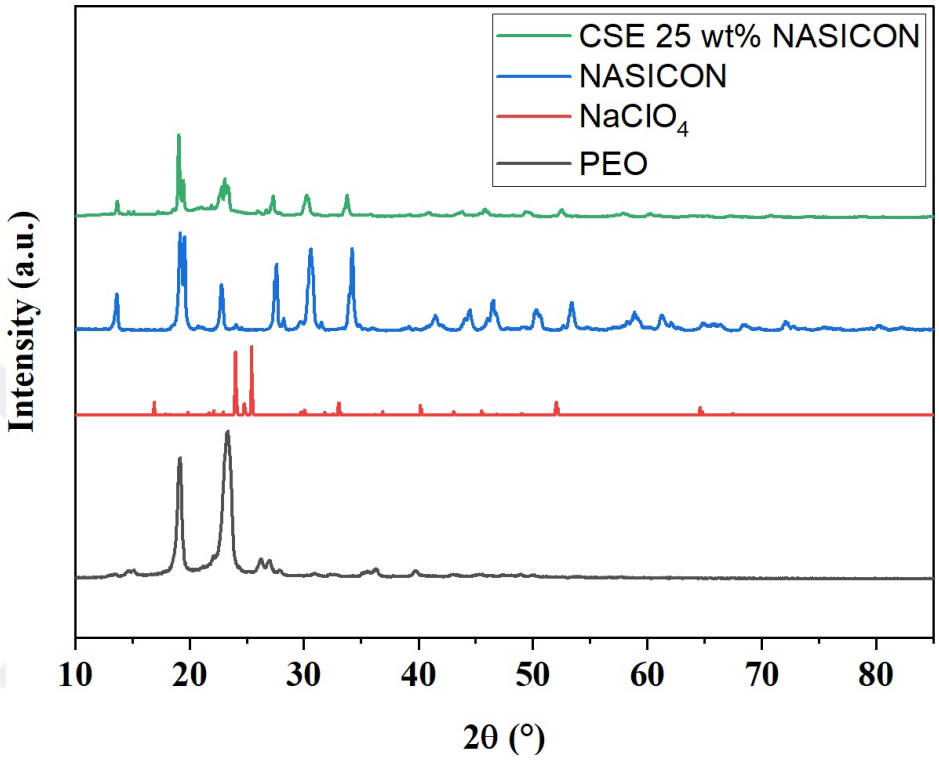

Figure 3.17. X-ray diffraction (XRD) patterns of the PEO, $NaClO_4$, NASICON and CSE.

The number of peaks in the XRD plots indicates the crystallinity of the polymer matrix. The addition of salt and NASICON crystals to the polymer will further increase the amorphous nature of the CSE's structure [81]. The decrease in crystallinity and the increase in amorphous regions directly contribute to the ionic conductivity. PEO has a semi-crystalline structure. These peaks at 19° and 23° are the characteristic peaks of PEO. As salt is added, the intensity of the peaks decreases and becomes broader. These broadening and decreasing in the intensity of the peaks in the XRD plot of the thin films after salt addition coincide with the results obtained by Bhide et al. by adding sodium metaphosphate salt to PEO [69]. This indicates an increase in the amorphous regions. The double peaks of pure NASICON between 23° and 24° degrees were transformed into triple peaks in the XRD plot of CSE. Zhang et al. explained this

transformation by the transition of NASICON from rhombohedral phase to monoclinic phase [82]. The monoclinic phase of NASICON has more channels for Na^+ ions to pass through than the rhombohedral phase. For this reason, the ionic conductivity of the CSE thin film increases with this phase transformation.

When salt and NASICON are added to the polymer, the intensity of peaks in the structure of CSE are significantly reduced. The intensity of the peaks of NASICON at 15°, 20°, 23°, 27°, 30° and 33° were reduced by half, while the 10 peaks between 40° and 70° almost disappeared. The fact that the XRD pattern of the CSE thin film does not show any peak separate from the characteristic peaks of polymer, salt and NASICON indicates that no extraneous phase has formed. Tanibata et al. analysed XRD plots of glass-ceramics containing sodium tetrasulfidosilicate and sodium thiophosphate and found that up to a certain percentage of sodium tetrasulfidosilicate no new peak was reported and attributed this to the absence of other crystalline phases [83]. Therefore, the CSE thin film containing 25% by weight of NASICON is an electrolyte with a highly amorphous character, without an unknown crystalline phase, and with an increased ionic conductivity compared to polymer.

Figure 3.18 shows the XRD patterns of SPE and CSE containing 20, 25 and 30 wt% NASICON. The addition of $NaClO_4$ to the polymer reduced the intensity of the characteristic peaks of polymer. During the addition of sodium perchlorate salt to the polyethylene oxide, distortions are observed between the ordered polymer chains of the semi-crystalline PEO. These distortions caused by the salt lead to the expansion of the amorphous regions of the polymer and a decrease in crystallinity. As a result, the mobility of the polymer chains increases and this leads to an increase in ionic conductivity.

As the NASICON content increased from 20% to 25%, the peak intensities decreased and the XRD plot shifted slightly to the right, as observed in the study by Anantha et al. [84]. Singh et al. explain this slight shift in the XRD plot by the strain at the polymer-salt interface [78]. However, as the NASICON concentration reached

to 30%, the peaks re-developed to their characteristic degrees and increased in intensity. The crystallinity of the CSE containing 30 wt% NASICON increased again as the intensity of the peaks in the XRD plot rose again.

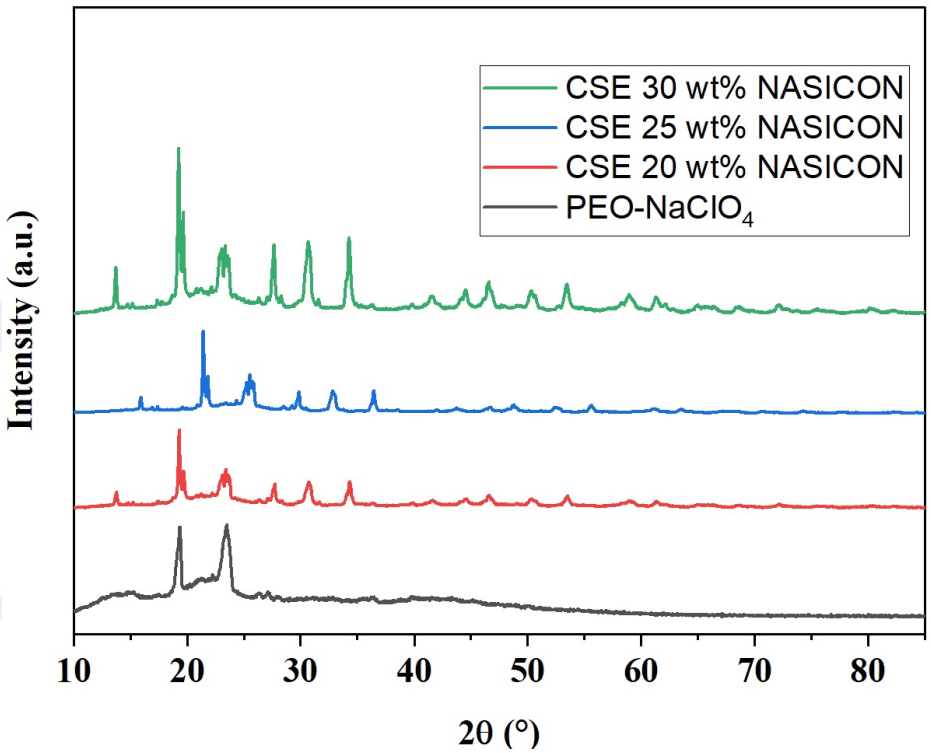

Figure 3.18. X-ray diffraction (XRD) patterns of the CSE with 0, 20, 25, 30 wt% NASICON.

3.4. FTIR Studies of the CSE Thin Films

FTIR analysis provides information about the bonds formed by the salt mixed into the polymer matrix with the polymer chains [74]. When sodium perchlorate salt is added to the polymer matrix, there is an interaction between the cations of the salt and the polar groups of polyethylene oxide. This is called complexation. This effect affects the local structure in the back-bone of the polymer and the active vibrational modes between the molecules [85]. The carbon, hydrogen and oxygen atoms in PEO chains perform a variety of oscillations. These include stretching, bending and twisting as they form bonds. The prominent band structure at 2880 cm^{-1} indicates CH_2 stretching

mode as in Neha's study [67]. The band at 1470 cm^{-1} in PEO chains shows the CH_2 bending mode. The defined band at 1340 cm^{-1} depicts deformation wagging of CH_2 bond in PEO as observed in the study by Shen et al [86]. The single peak at 1340 cm-1 shows the swinging vibration of CHs in the CH_2 groups in the amorphous phase of PEO and proves that the amorphous character of the polymer-salt complex increases as observed in the study by Dey et al [87]. The CH_2 twist mode can be seen in the band at 1280 cm^{-1}. The CH_2 stretching mode at 962 cm^{-1} in pure PEO shifted to 945 cm^{-1} when salt was added to the polymer matrix as can be seen in Figure 3.19.

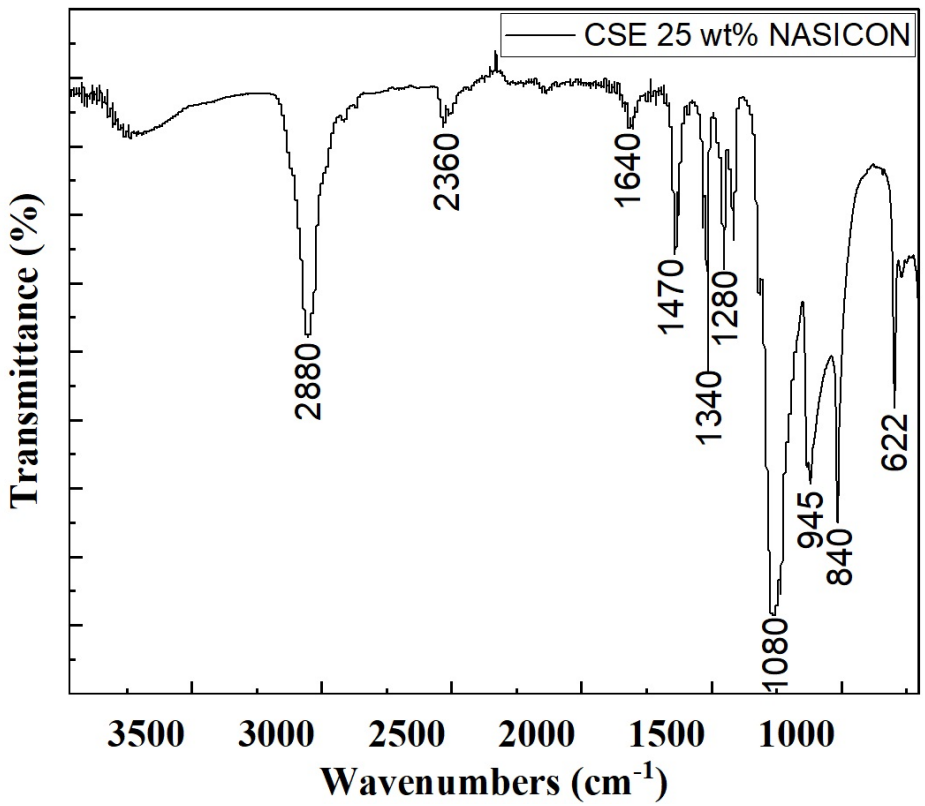

Figure 3.19. FTIR analysis of CSE 25 wt% NASICON.

The C-O-C stretching bands seen at 1110 cm^{-1} in pure PEO shifted to 1080 cm^{-1} in the presence of $NaClO_4$. This indicates the formation of a polymer-salt complex and coordination of EO and Na^+ ions [85]. The band formation at 622 cm^{-1} upon addition of salt, which is not present in pure PEO, also indicates the formation of $\nu(ClO_4^-)$ ion. This shows ion-ion interaction at the molecular level [74]. The band observed

between 900 cm^{-1} and 1000 cm^{-1} is typical for monoclinic symmetry and is due to the stretching patterns of phosphate ions, as observed in the study on NASICON by Giarola et al [88].

Figure 3.20 illustrates the FTIR analysis of CSE containing 20, 25 and 30 wt% NASICON. When the NASICON ratio reached 25 wt%, the band at 1080 cm^{-1} became widest. This broadening indicates an increase in the amorphous phase of PEO. It means that NASICON forms conduction lines along the CSE thin film and prevents crystallisation of the polymer-salt complex. The NASICON 25% sample has more defined and broad bands at 2880 cm^{-1}, 1340 cm^{-1} and 1080 cm^{-1}, attributing the higher ionic conductivity. In all three samples, the $\nu(ClO_4^-)$ ion was formed at 622 cm^{-1}. In CSEs containing 20 and 30 wt% NASICON, the C-O-C stretching bands shifted slightly away from 1080 cm^{-1}. The band at 945 cm^{-1} in the CSE containing 25% NASICON, representing the CH_2 stretching mode, appeared at 923 cm^{-1} in the CSE containing 30% NASICON.

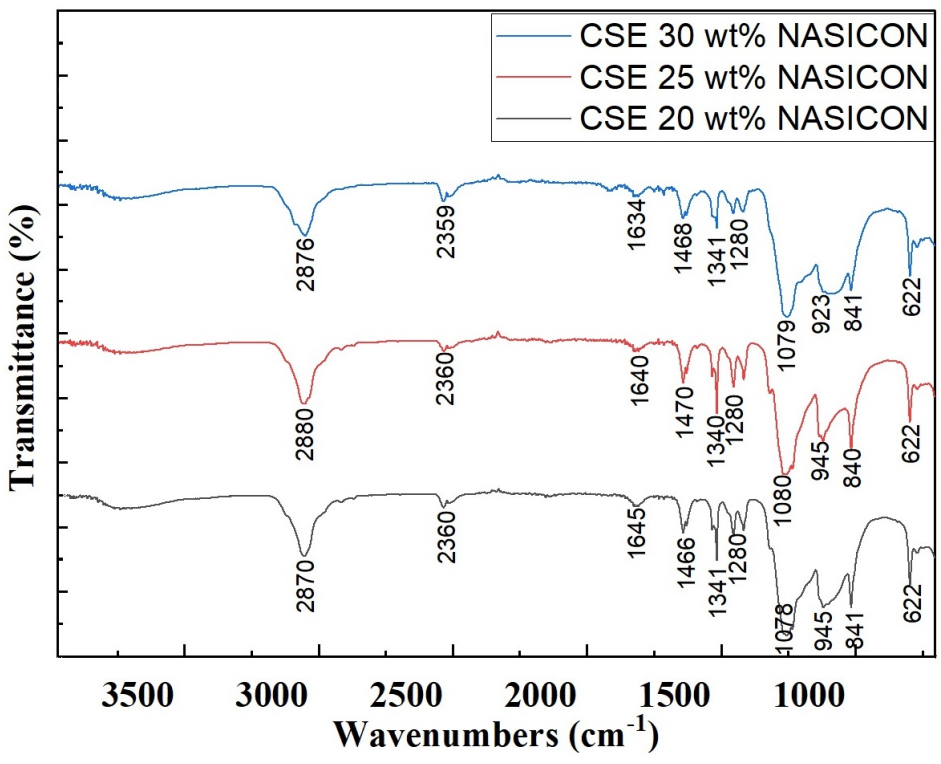

Figure 3.20. FTIR analysis of CSEs with 20-25-30 wt% NASICON.

3.5. Ionic Conductivity Studies of the CSE Thin Films

Nyquist plots obtained as a result of EIS analysis of CSEs containing 20, 25, 30 and 40 wt% NASICON at 25 °C and CSEs containing 25 wt% NASICON at various temperatures are shown in Figure 3.21 and Figure 3.22, respectively.

In order to calculate the ionic conductivity of CSE, it is necessary to know the thickness and impedance of the films and the surface area of the electrodes. The surface area of the electrodes used in this study is 0.7854 cm^2. CSE film electrolytes were sandwiched between electrodes of the same surface area from two sides and their ionic conductivities were measured. Therefore, the contact area in Equation 2.2 is 0.7854 cm^2. However, the thickness of each CSE thin film is different. The thicknesses of CSE thin films containing 20, 25, 30 and 40 wt% NASICON were measured to be 88, 60, 80 and 70 microns respectively. Therefore, the film thicknesses in Equation 2.2 vary according to the NASICON content of the CSEs.

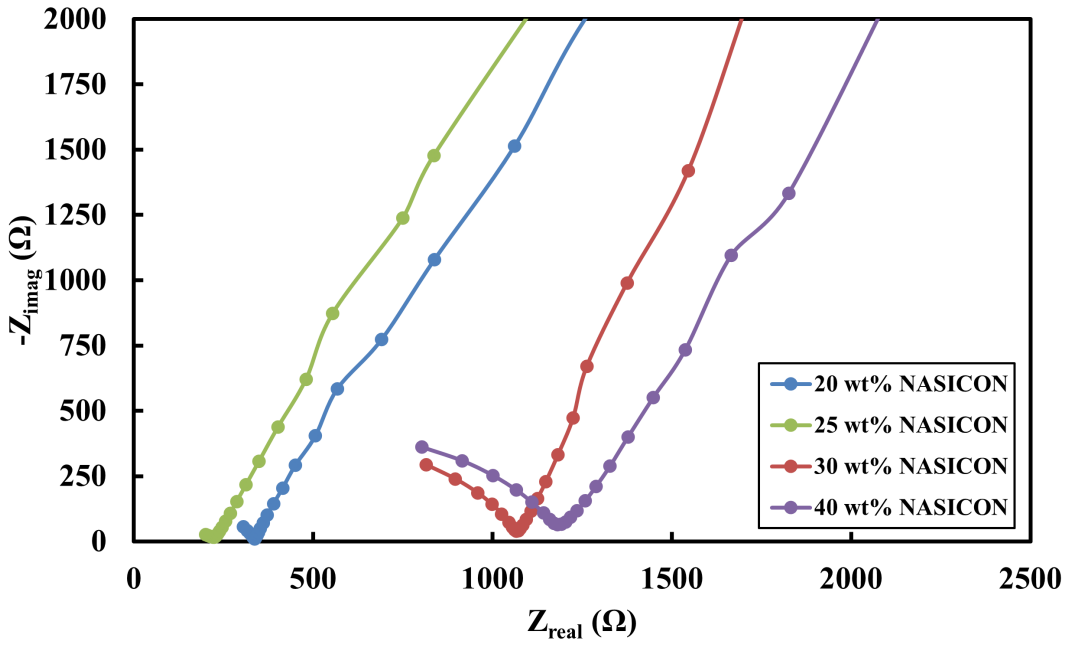

Figure 3.21. Nyquist plots of the CSEs containing 20, 25, 30 and 40 wt% NASICON at 25 °C.

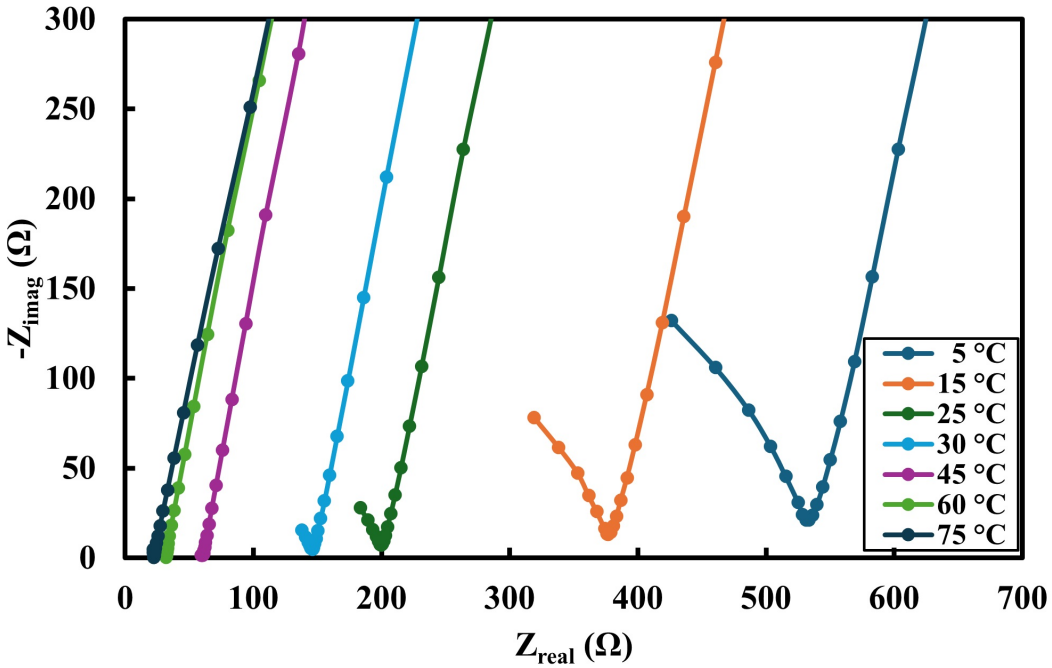

Figure 3.22. Nyquist plots of the CSEs at different temperatures.

In order to calculate the ionic conductivities, the impedances of CSE thin films must be measured accurately. For this purpose, it is necessary to construct the most suitable equivalent circuit diagram for Nyquist plots. In order to fit the Nyquist plots, different equivalent circuit models were tried, and the best model was determined.

Established models and fitting curve are shown in Figure 3.23 and Figure 3.24, respectively. In Figure 3.23c, an R and a CPE element are connected in parallel and a CPE circuit element is connected in series. In this model, resistance R represents the sum of two different types of impedances that ions encounter across the electrolyte. The first represents the resistance within the grains, and the second represents the resistance between the grain boundaries.

Among the equivalent circuit models tested, in Figure 3.23d, bulk and grain boundary resistances are modeled with two R's added to the model. According to this model, the bulk resistance is less than one percent of the grain boundary resistance. For this reason, in order to reduce the error rate, the bulk and grain boundary resistance are modeled with a single R in the equivalent circuit model. And with the circuit in

Figure 3.23c, the error rate in the circuit was reduced from 1.5% to 1%. The error rates of the parameters of the CPEs and resistors in the equivalent circuits are shown in Figure A.2.

Figure 3.24 displays the fitting study of a composite solid electrolyte with EIS analysis. The circuit in Figure 3.23a is not a proper model for fitting. This is because by creating a straight line only, it cannot provide a proper semicircle and a line that coincide with the values in the Nyquist plot. The circuit in Figure 3.23b was able to model the semicircle, but not the peak.

The model in Figure 3.23c is a perfect model for the Nyquist plot of the CSE. This equivalent circuit model coincides exactly with the semicircle and peak of the Nyquist plot of CSE.

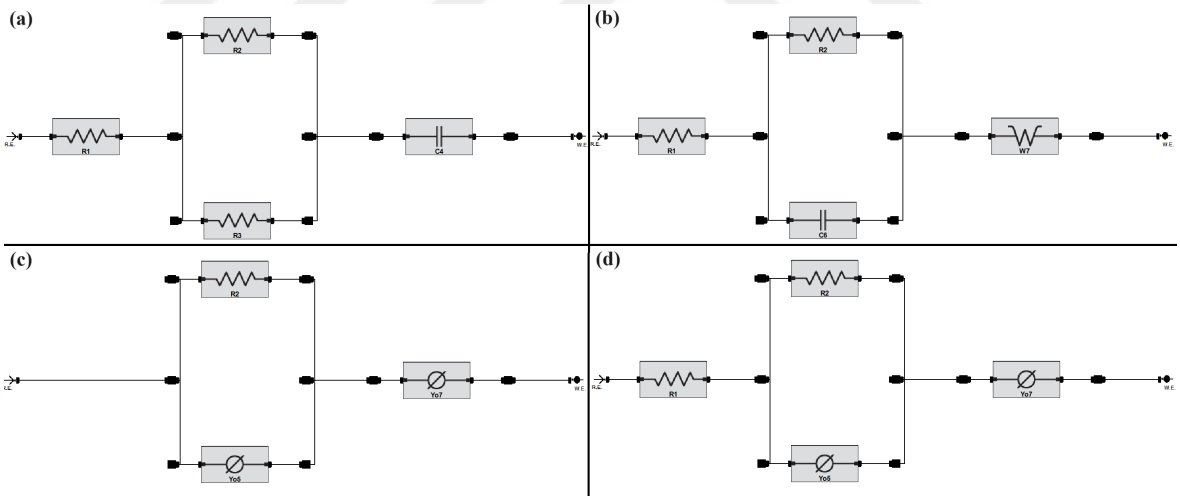

Figure 3.23. Equivalent circuit models for fitting studies of EIS in terms of (a) R's and C, (b) R's, C and W, (c) R and CPE's, and (d) R's and CPE's.

All subsequent fits were based on the model in Figure 3.23c. Using the equivalent circuit model in Figure 3.23c, CSE ionic conductivities were determined by substituting impedances from Nyquist plots into the impedance in Equation 2.2. The ionic conductivity values are reported in Figure 3.11. After fitting according to the equivalent

circuit model in Figure 3.23c for each Nyquist plot, the impedances of the CSE thin films are found.

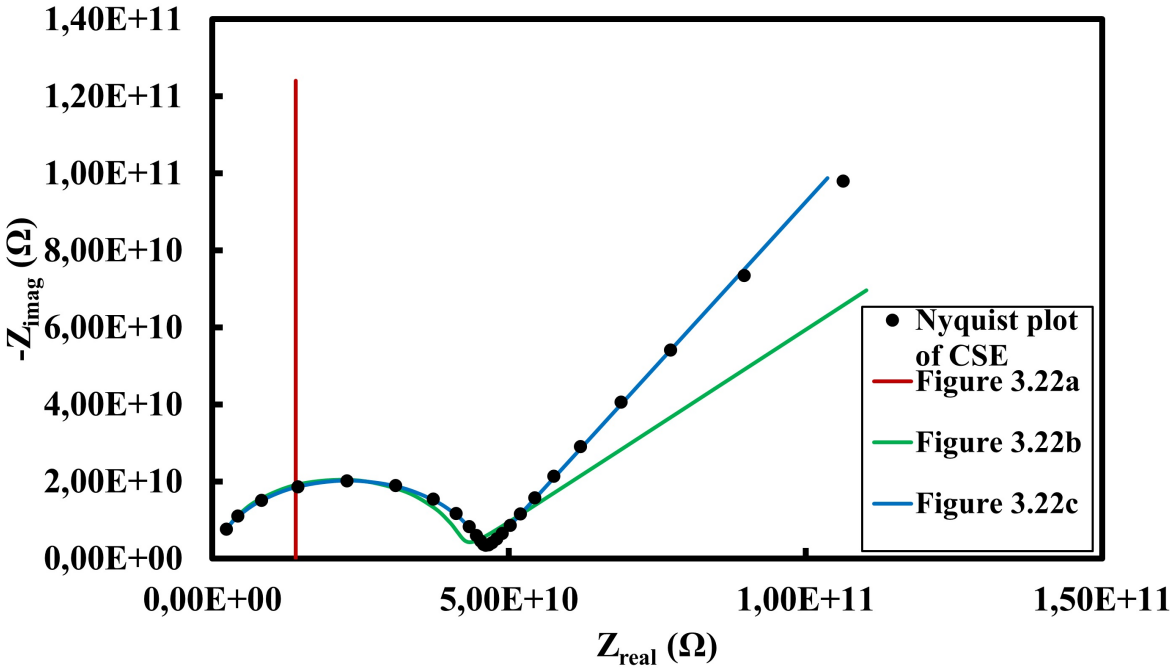

Figure 3.24. Fitting studies of equivalent circuit models.

Since the film thickness, contact area and impedances of each composite solid electrolyte are known, the ionic conductivities of CSE thin films can be calculated. Figure 3.21 shows the impedance values obtained after fitting the Nyquist plots of CSEs containing 20, 25, 30 and 40 wt% NASICON in Figure A.3.

For example, the impedance of the CSE thin film containing 20 wt% NASICON was measured as 330 ohms. The average thickness of the CSE thin film is 88 microns. The contact area of the electrodes is 0.7854 cm^2. Substituting these values into Equation 2.2, the ionic conductivity is measured to be 3.39×10^{-5} S cm^{-1}.

The higher the NASICON content, the higher the impedance. For example, when the NASICON ratio of the composite solid electrolyte reaches 40 wt%, the impedance of the electrolyte increases and reaches 1206 ohms. The thickness of the electrolyte containing 40% NASICON by weight is approximately 70 microns. Since the surface

area does not change, the ionic conductivity of the electrolyte is 7.39×10^{-6} S cm^{-1} at room temperature.

Figure 3.25 presents Arrhenius plots of CSEs containing different percentages of NASICON by weight.

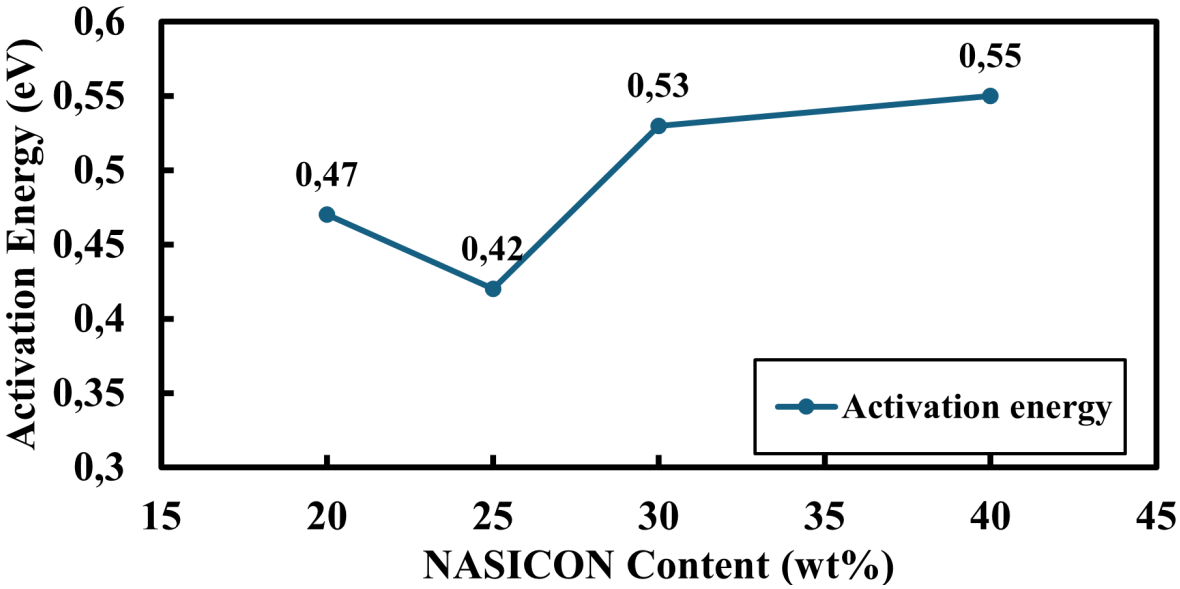

Figure 3.25. Arrhenius plots of the CSEs with 20-25-30-40 wt% NASICON.

The activation energy of the CSE containing 20 wt% NASICON was calculated to be 0.47 eV. When the NASICON ratio reached 25%, the activation energy reached its lowest value of 0.42 eV.

As can be seen from Figure 3.24, the linear fit line of the CSE containing 25 wt% NASICON has a much better distribution than the other samples. Almost all the ionic conductivity values are above the fit line.

The activation energies of sodium ion solid electrolytes calculated from studies in the literature vary between 0.10 eV and 0.54 eV. Wang et al. reduced the activation energy of a magnesium-doped sodium sulphate fluoride solid electrolyte from 0.32 eV to 0.099 eV [89]. Olson et al. reported that the activation energy of sodium ion glassy

solid electrolyte varied between 0.41 eV and 0.54 eV [90]. Chong et al. reported the activation energy of NASICON solid electrolyte enriched with sodium dihydrogen phosphate to be 0.11 eV [91]. Wang et al. showed that the activation energy of magnesium-doped NASICON solid electrolyte varied between 0.29 eV and 0.40 eV [92]. Gebi et al. explained the activation energy of NASICON solid electrolyte produced by high energy milling as 0.20 eV [93].

Therefore, the activation energy value of 0.42 eV found in this study is consistent with other studies in the literature. It is possible to reduce the activation energy from 0.42 eV to 0.20 eV by increasing the number of channels through which Na^+ ions pass by adding additives such as magnesium and phosphate to NASICON.

Figure 3.26 shows that since the ratio of NASICON continued to increase, the impedance became larger and the ionic conductivity began to decrease as the density of sodium ions and grain boundaries in the CSE grew.

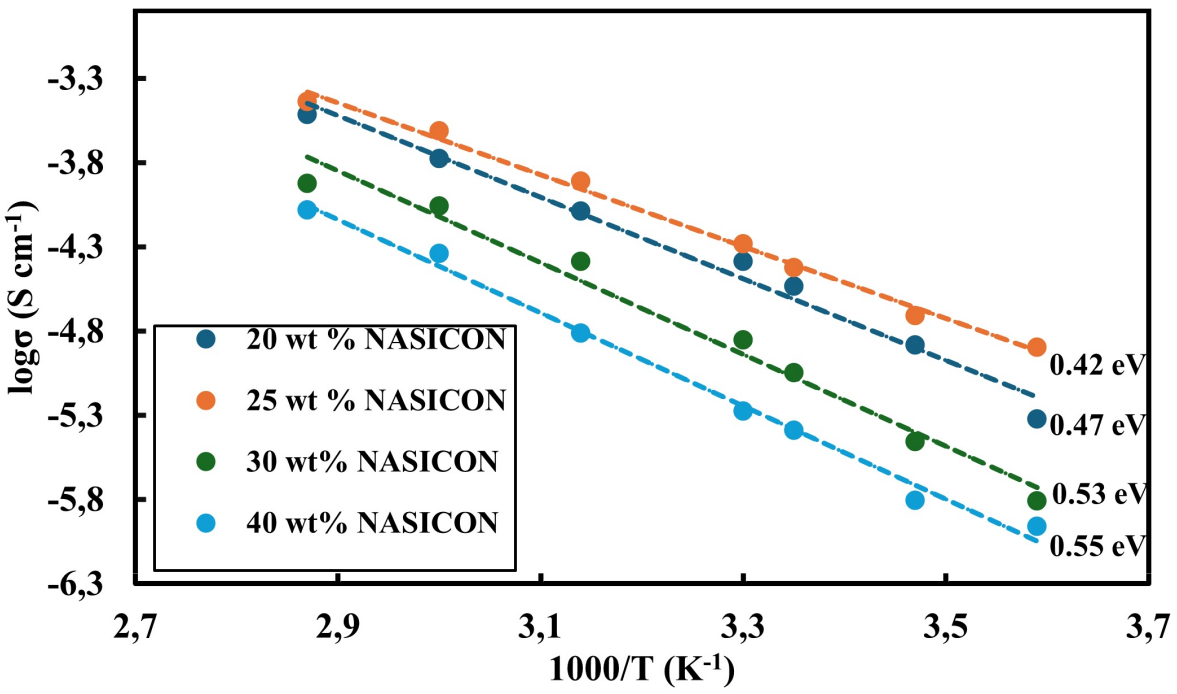

Figure 3.26. Activation energy of CSEs with 20, 25, 30 and 40 wt% NASICON.

The activation energy of CSE containing 25 wt% NASICON is 12.5 percent lower than the activation energy of pure PEO [94]. The ionic conductivities of CSEs were measured over a wide range from 5 °C to 75 °C. The activation energies of sodium ions, which attach to the polymer chains along the electrolyte and move through the channels formed by the amorphous regions of the polymer and the crystal structure of the NASICON particles, vary greatly with temperature. For this reason, the ionic conductivities of the composite solid electrolyte samples were measured over a wide temperature range from 5 °C to 75 °C. This wide range facilitated the calculation of activation energies more accurately.

Increasing temperature increases the chain mobility of the polymer as well as the mobility of Na^+ ions resulting in a reduction in activation energy. The activation energy of CSEs is less than 30% of the activation energy of pure NASICON [5]. The improvement in electrolyte/electrode interface contact conditions is one reason for the increase in ionic conductivity with increasing temperature. The elasticity provided by the polymer chains to the CSE thin film provides better wettability at high temperature and increases ionic conductivity by reducing the impedance at the contact surfaces.

3.6. Effect of Pressure and Preload on Ionic Conductivity

The only way to increase the ionic conductivity of electrolytes is not to change the inorganic fillers or their weight percentages. Ionic conductivity can also be increased by physical and mechanical effects such as temperature and pressure.

Temperature can contribute positively to ionic conductivity by lowering the activation energy required for ions to move through the electrolyte. Nonetheless, as the temperature increases, the components in the electrolyte can begin to react with each other in undesirable ways [95]. As the temperature changes, different phases may appear that are difficult to stabilize [96]. Since the temperature rise affects the electronic conductivity of the electrolyte, it can also cause a short circuit by increasing the electronic conductivity due to dendrite growth extending into the electrolyte.

The pressure effect contributes to ionic conductivity mainly by improving the interfacial contact conditions. However, the mechanical structure of the electrolyte must also be pressure compatible. Solid electrolytes with a polymer structure are compliant because the polymer matrix imparts flexibility to the electrolyte, which improves contact conditions. Without a polymer matrix, electrolytes with NASICON-type or alumina-type inorganic active ceramics or oxide ceramics such as TiO_2, ZrO_2 are inherently brittle. Therefore, the ionic conductivity of polymer-based solid electrolytes can be increased by pressure without any undesirable reaction.

The ionic conductivities of CSE were measured in the pressure range of 60 kPa to 900 kPa using the device designed and manufactured in this study. The pressure was increased to the limit of 900 kPa because the scattering in the Nyquist plate was too high to perform fitting studies. To study the pressure effect, CSEs placed between the steel electrodes were compressed and released in one, two and three cycles. During each compression and relaxation process, ionic conductivities were measured and plotted during the compression-relaxation cycles. Figure 3.27 represents the ionic conductivity plot of a once-compressed and relaxed CSE.

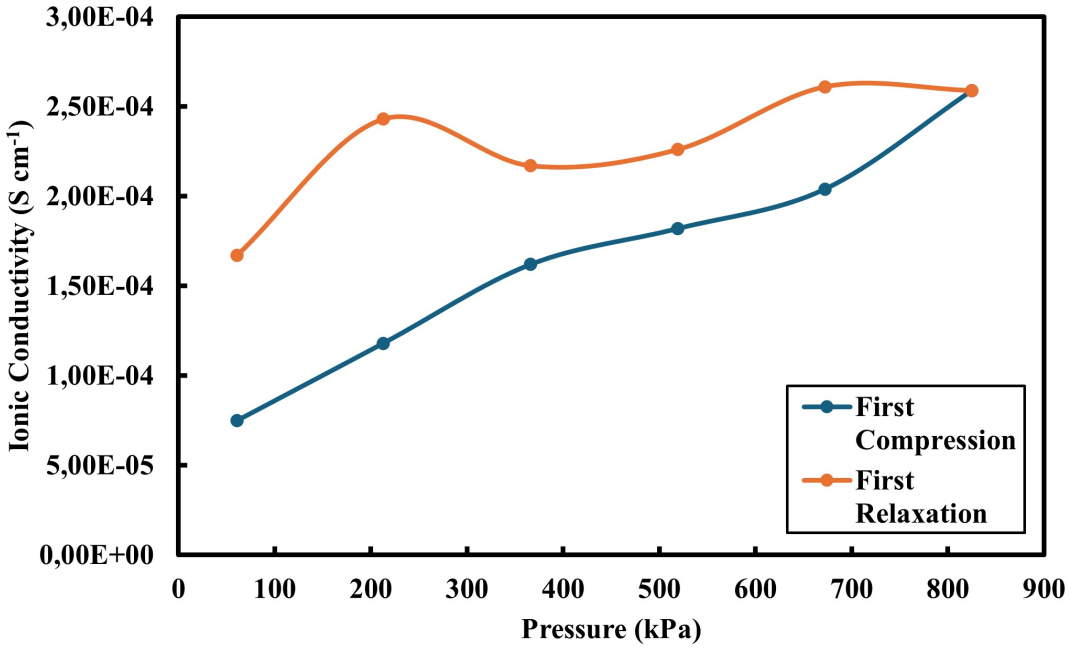

Figure 3.27. One cycle compression-relaxation plot of CSE.

The ionic conductivity of CSE was measured to be 7.49×10^{-5} S cm^{-1} at an initial pressure of 60 kPa. When the CSE was compressed to 825 kPa and then reduced to 60 kPa, the ionic conductivity increased to 1.67×10^{-4} S cm^{-1}. The ionic conductivity of CSE containing 25 wt% NASICON increased by 120% after a preload of 825 kPa indicating better contact between the electrode and the electrolyte. In addition, the ionic conductivity values were higher than the initial state when the pressure on the electrolyte was released indicating that there is a permanent sticking at the interface.

The compression work on the CSEs is continued with a two-cycle compression-relaxation test. In the two-cycle compression-relaxation test shown in Figure 3.28, the ionic conductivity increases during relaxation after the first compression. The ionic conductivity, which increased to 3.87×10^{-5} S cm^{-1} in the first compression, was recorded as 5.17×10^{-5} S cm^{-1} at 825 kPa after the second compression.

According to these measurements, the ionic conductivity of CSE compressed twice to 825 kPa increased from 1.02×10^{-5} S cm^{-1} to 5.17×10^{-5} S cm^{-1}. This means a 4-times increase in ionic conductivity. After two cycles, the ionic conductivity of the electrolyte was recorded as 2.11×10^{-5} S cm^{-1} at 60 kPa. Consequently, the ionic conductivity doubled after two compression-relaxation process.

The effect of pressure on electrolytes increases wettability at interfaces, and decreases impedance [46, 97]. Therefore, increasing pressure reduces the impedance of the entire electrolyte and enhances ionic conductivity.

Another effect of the pressure that has a direct effect on conductivity is the reduction of the film thickness. After the first compression-relaxation cycle, the CSE thin film thickness decreased by approximately 10%. After the second compression-relaxation cycle, the CSE thin film thickness decreased by approximately 25% compared to the initial value. After the third compression-relaxation cycle, the thickness of the CSE thin film decreased by approximately 35% of the initial thickness. However, the initial thickness of the CSE thin films was taken into account when calculating the

ionic conductivities at each pressure value. The reason for this is not to determine the exact ionic conductivity values caused by the pressure applied to the CSE thin films, but to investigate the effect of compression-relaxation cycles on ionic conductivities. In addition, a compression-relaxation cycle starts at 60 kPa, increases by 150 kPa up to 825 kPa and decreases by the same amount back down to 60 kPa. Since the initial thickness of the CSE thin film is 60 microns, it is necessary to examine the electrolyte under SEM to determine the change in thickness after each pressure increase and decrease. For this, the electrolyte must be removed from the test rig. However, this will make it difficult to obtain accurate test data as the effect of loading and unloading on the electrolyte at the electrolyte/electrode contact surfaces will disappear. At the beginning of the first compression-relaxation cycle, the ionic conductivity calculated with the initial CSE thin film thickness was 7.62×10^{-6} S cm^{-1} at 60 kPa and 1.63×10^{-5} S cm^{-1} at 825 kPa. The decreasing effect of a decrease in thickness on ionic conductivity is about 13 per cent, whereas the increasing effect of pressure on ionic conductivity by decreasing impedance is about 115 per cent. There is a large difference in the increase in ionic conductivity in favour of the enhancement of ionic conductivity. Furthermore, this difference is the effect of the thickness measured after the first compression-relaxation cycle. After the second compression-relaxation cycle, this difference grows even more in the favour of the increase in ionic conductivity.

According to Equation 2.2, a decrease in film thickness would generally lead to a decrease in ionic conductivity. In Inorganic Solid Electrolytes, the film thickness increases, the grain size increases. Large grains provide a more regular conduction path for ions than small grains. As the film thickness increases, the ionic conductivity increases because more conduction channels are formed for the ion carriers. In composite films containing nanoparticles, ionic conductivity increases to a specific thickness called the percolation threshold [43]. As the film thickness increases, the carriers travel longer in the electrolyte before they are scattered. In thin films, defects such as grain boundary irregularities and voids cause more frequent carrier scattering, which reduces ionic conductivity [98]. However, it can be said that the increase in ionic conductivity after the first two cycles and the improved interfacial contact conditions overcome the

decrease of ionic conductivity by decreasing thickness.

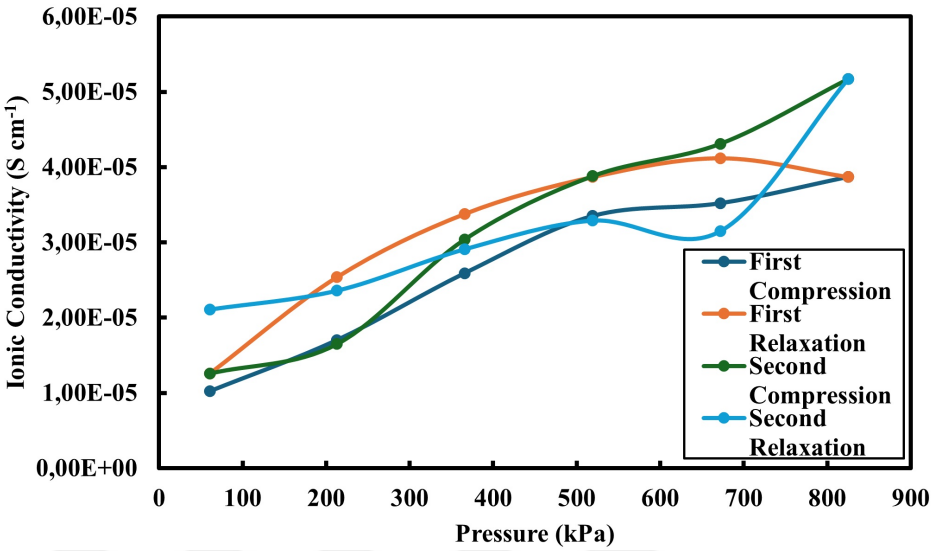

Figure 3.28. Two cycles compression-relaxation plot of CSE.

After the third cycle, there was no increase in ionic conductivity, unlike what was observed in the one and two-cycle tests. Figure 3.29 was plotted by averaging the pressure and ionic conductivity values of CSE thin films.

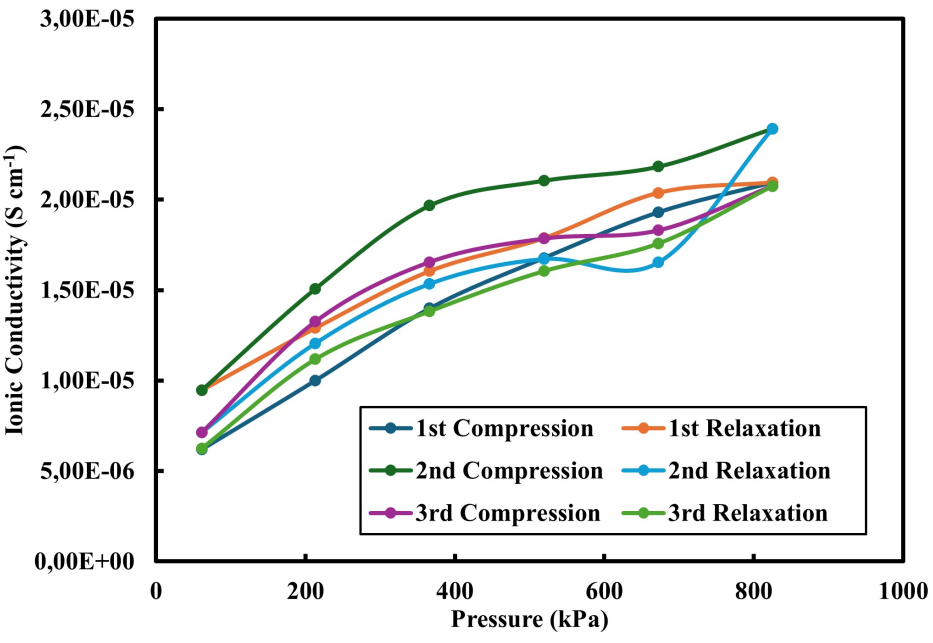

Figure 3.29. Three cycles compression-relaxation plot of CSE.

Figure 3.30 indicates that the ionic conductivity after the third cycle is more or less equal to the start of the first cycle indicating that the gain in ionic conductivity after the first and second cycles are completely lost.

The plot of the second and third compression test is shown in Figure 3.31. The purple curve, which represents the third compression, is in most cases below the green curve, which represents the second compression. In most cases, the ionic conductivity values obtained with the third compression of CSE thin films were lower than those obtained with the second compression.

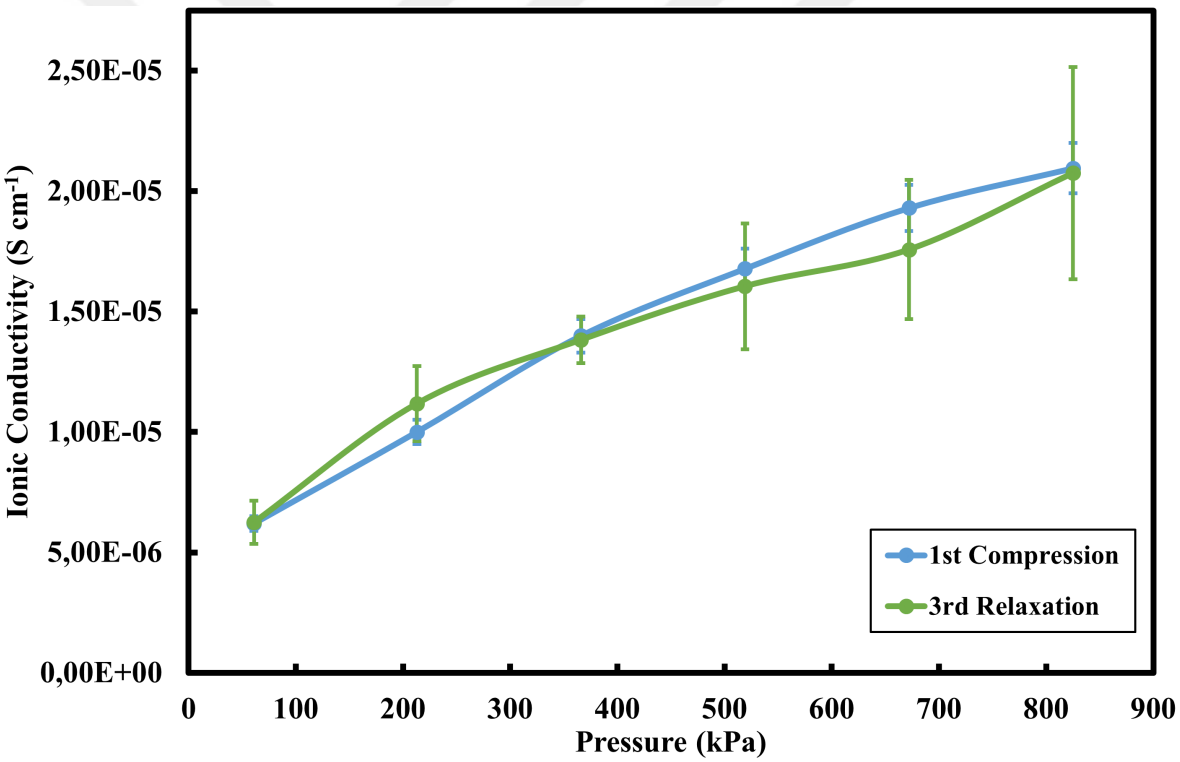

Figure 3.30. First compression and third relaxation of CSE.

Therefore, an increase in the ionic conductivity of the CSE thin films was observed only after the first two compression cycles. However, a decrease in the ionic conductivity of the electrolyte is observed after three cycles of compression. This can be explained in terms of the mechanical structure of the electrolyte. As a result of the first two preloads, a sufficient adhesion of the electrolyte on the electrode surfaces was

ensured by the adhesion of the film to the solid surface of the electrode provided by the flow of the polymer matrix. As a result, the wettability of the electrolyte reached the maximum level.

However, during the third load, the strength of the CSE thin film gradually decreased and discontinuities formed on the contact surfaces. With the onset of the third load, the stability of the CSE thin films, which became thinner in the cross-section, also deteriorated.

With the third compression, two main problems were observed in the CSE thin films. The first is the flow of electrolyte towards the periphery of the electrodes and the other is the onset of tearing in the middle region of the electrolyte.

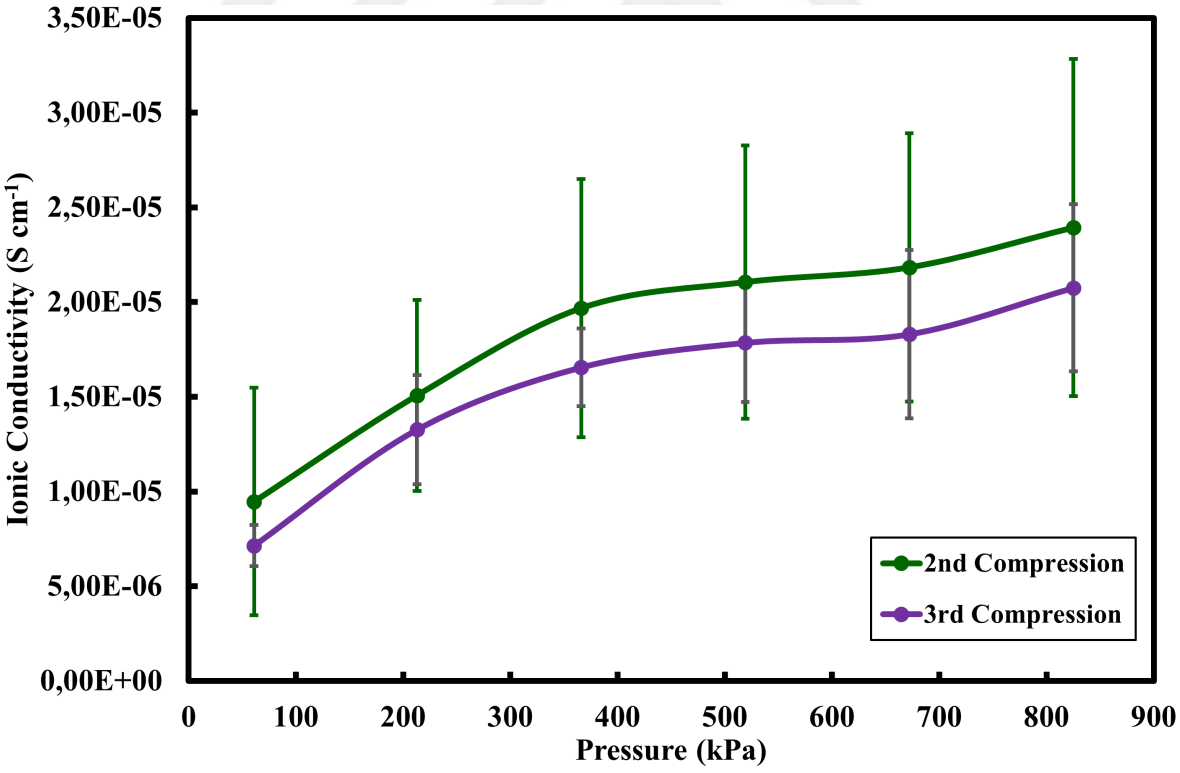

Figure 3.31. Second and third compression of CSE.

Figure 3.32 displays photographs of electrolytes compressed three times and one of the electrodes removed after impedance measurements. Figure 3.32 represents that

the inner region of the CSE film is more transparent than the edge. The thickness of the electrolyte gradually decreased in the inner region and thickened towards the periphery due to flow of the polymer matrix.

The region through which sodium ions travel through the electrolyte narrows from the entire area of the electrode to the periphery. As a result, the ions must pass through a narrower area at the periphery of the contact region and the impedance increases. At the same time, the central region of the electrolyte is slightly thinner as a result of the third compression. As a result of the irregularity in the thickness of the electrolyte, the ionic conductivity decreases significantly.

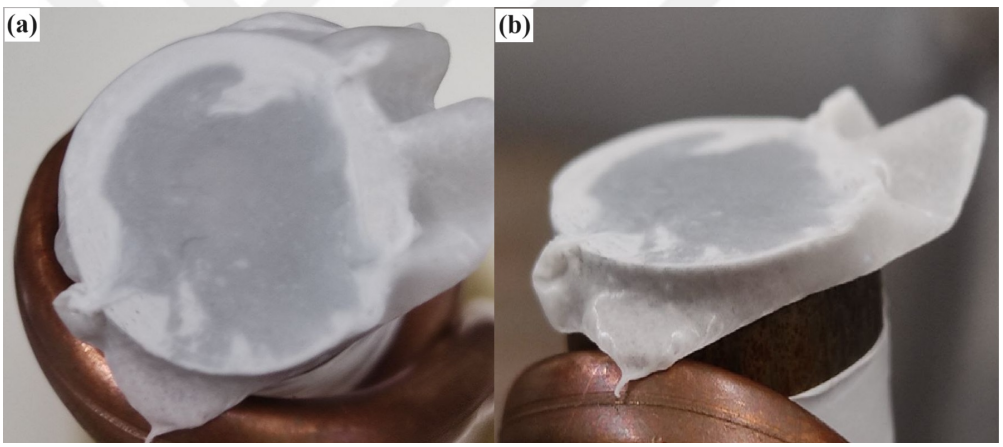

Figure 3.32. Thinning of CSE film at the centre after the third compression cycle.

Figure 3.33 demonstrates the onset of tearing on the electrolyte surface with the third cycle. In Figure 3.34, complete tears are represented. NASICON particles insoluble in the polymer develop localized agglomerates. The average modulus of elasticity of NASICON is 80 GPa and 320 MPa for PEO. The modulus of elasticity of NASICON is therefore 250 times greater than that of PEO [99, 100].

NASICON, which has more rigidity as compared to the polymer, resists pressure much more than polymer. As the compression-relaxation cycles continue, the thickness of the electrolyte decreases and NASICON particles cause tears in the polymer matrix.

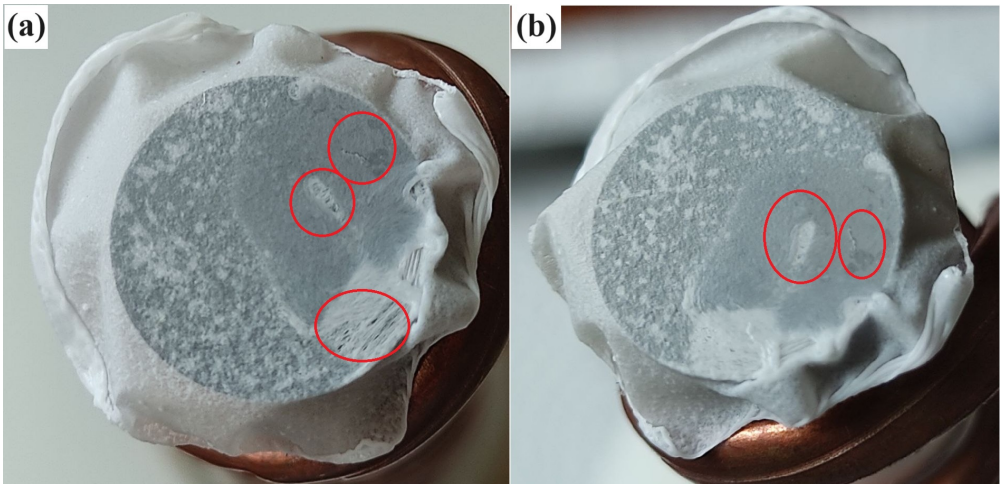

Figure 3.33. The onset of tearing of CSE thin film with the third compression.

The elastic moduli of the electrolyte components are very different, which can cause significant degradation after more than two compression-relaxation cycles. Thus, strengthening the mechanical structure of the polymer matrix with cross-linking or reducing the particle size of inorganic fillers to much smaller sizes and preventing agglomeration can improve the integrity of CSE thin films [101].

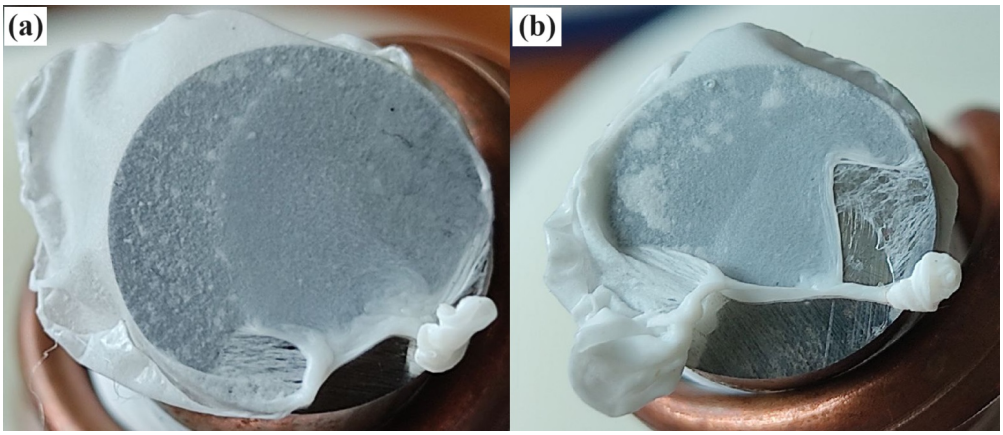

Figure 3.34. Tearing of CSE thin film with third compression.

The cross-sectional thicknesses of the CSE thin film after the first compression are shown in Figure 3.35a and Figure 3.35b. Accordingly, the average film thickness is 71 microns.

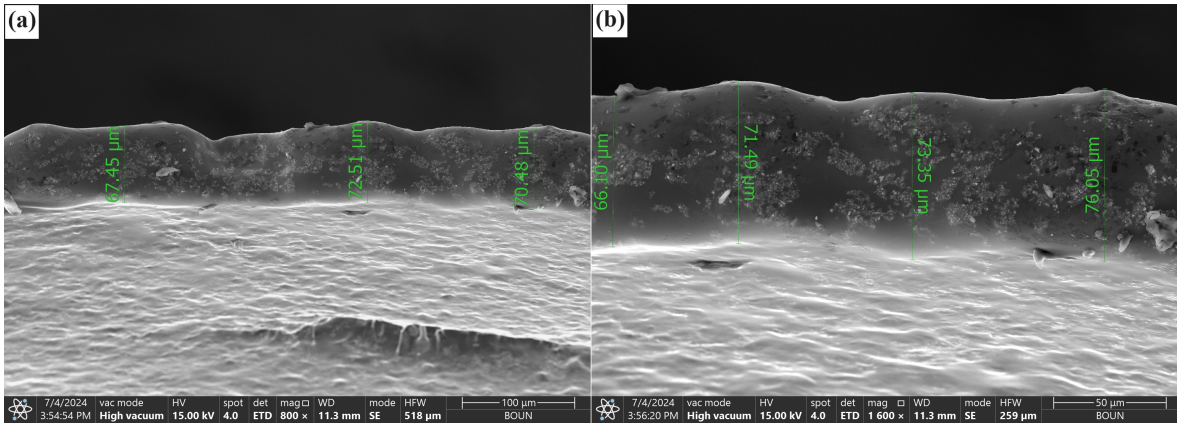

Figure 3.35. Cross-sectional image of CSE after first compression at (a) 800 magnifications and (b) 1600 magnifications.

After the first compression-relaxation cycle, the electrolytes have a wavy structure. The electrolyte/electrode contact surface conditions are not satisfactory. The impedance across the electrolyte is high due to the undulations on the surface. After the second compression-relaxation cycle, the average film thickness decreased to 60.88 microns (Figure 3.36a and Figure 3.36b).

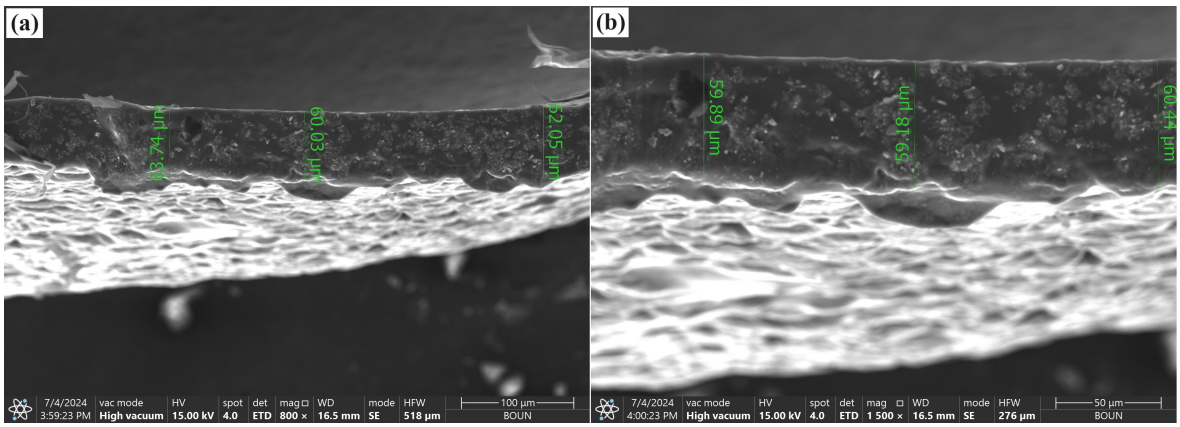

Figure 3.36. Cross-sectional image of CSE after second compression at (a) 800 magnifications and (b) 1500 magnifications.

The undulations observed after the first compression were reduced and the electrolyte/electrode contact surface conditions improved. The NASICON crystals were

more homogeneously dispersed in the electrolyte as it flows after the second compression. Although the thickness of the CSE film decreased, the ionic conductivity increased to its maximum level due to the increase in contact areas.

After the third compression, the average thickness of the CSE thin films was 54.27 microns (Figure 3.37a and Figure 3.37b). In the third compression, the film thickness decreased by approximately 35% compared to the initial thickness. The wavy structure seen after the first compression were again observed.

The NASICON crystals resist the reduction of thickness at the regions they are concentrated. The polymer rich thinner areas and thicker regions with higher concentration of NASICON caused the undulation in thickness resulting in the deterioration of the surfaces as well as tearing of the electrolyte film, resulting in lower ionic conductivity. The irregularity of the film thickness and the tearing of the polymer structure increased the impedance across the electrolyte and decreased the ionic conductivity.

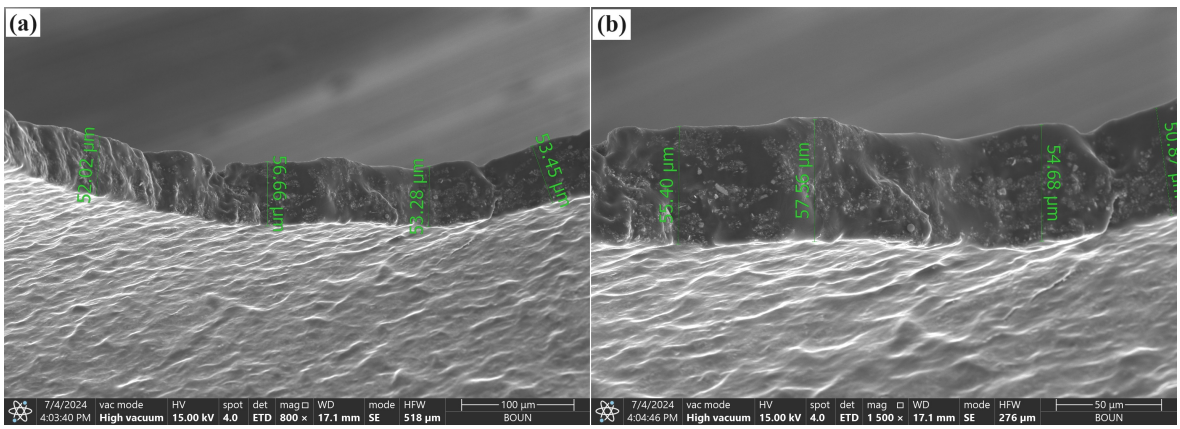

Figure 3.37. Cross-sectional image of CSE after third compression at (a) 800 magnifications and (b) 1500 magnifications.

4. CONCLUSION

We have manufactured NASICON containing polymer-based sodium ion solid electrolytes by solution casting method. The ideal combination ratio of polymer to $NaClO_4$ is determined to be [EO:Na^+] 15:1. We have conducted SEM and EDX analysis to investigate how NASICON particles can impact the microstructure of the composite electrolyte after ball milling. The ideal weight percentage of NASICON added to the polymer electrolyte has been determined to be 25%. This is the percentage by weight of NASICON contained in the CSE thin film with the highest ionic conductivity. As the NASICON content in the CSE increased, the NASICON particles agglomerated due to the high density. These localized clusters made it difficult for ions to pass through the film by increasing the impedance due to increased grain boundaries. Additionally, the agglomeration caused significant film thickness variations, resulting in decreased ionic conductivity due to incomplete contact at electrolyte/electrode interfaces.

It is found that inorganic fillers such as NASICON facilitate the passage of ions through the channels provided by their crystal structure and increase the ionic conductivity from 4.00×10^{-6} S cm^{-1} to 5.00×10^{-5} S cm^{-1}. By XRD study on CSE, we observed how the addition of NASICON increases the density of the amorphous regions of the polymer. The stretching, bending and twisting motions in the polymer chains were revealed by FTIR study and correlated with ionic conductivity measurements. The temperatures of the CSEs have been adjusted in a controlled manner by means of a circulator with a mechanism designed for this research. The ionic conductivities of CSEs have been measured over a wide range from 5 °C to 75 °C. EIS study has been used to investigate the temperature dependence of the ionic conductivity. Different equivalent circuit models were developed for the Nyquist plots and performed fitting studies. The lowest activation energy of the CSE is calculated to be 0.42 eV.

One, two and three-cycle compression-relaxation tests have been conducted on the CSE. With the pressure applied to the CSE, the ionic conductivity is measured at

7.49×10^{-5} S cm^{-1} at 60 kPa and 1.67×10^{-4} S cm^{-1} at 825 kPa. It is demonstrated that applying two preloads to the electrolytes results in the maximum ionic conductivity value. Additionally, it is shown that the mechanical structure of the electrolyte deteriorates when a three-cycle preloading is applied resulting in a decrease in ionic conductivity.

The contribution of mechanical effects to the ionic conductivity of CSE thin films has not been sufficiently investigated in the literature. In this thesis, the contribution of mechanical effects to the ionic conductivity of CSE thin films has been revealed. The enhancement effect of pressure on the mechanical structure of CSE thin films and electrolyte/electrode contact surfaces was demonstrated. The changes in the microstructure of CSE thin films caused by cyclic compression-relaxation tests were investigated in terms of ionic conductivity and interfacial contact conditions. As part of this work, a mechanical test rig was constructed to measure the temperature and pressure of CSE thin films. With this test rig it was possible to heat only the electrolyte and the steel rods acting as electrodes instead of the furnaces that heat the whole system. The unique design of the test rig allowed the temperature of the electrolyte to be measured directly and the activation energy to be calculated with very low error. The test rig's threading mechanism enabled precise calculation of the spring's compression on the electrolyte, thereby accurately assessing the pressures exerted on it. The displacement-controlled system allowed for the comprehensive study of pressures applied to the electrolyte across a broad spectrum.

5. FUTURE WORK

In the synthesis of CSE thin films, PEO is used as the polymer matrix, $NaClO_4$ as the sodium source and NASICON as the inorganic filler. In addition, plasticizers can be used to increase the ionic conductivity or the polymer matrix can be improved by polymer blends, copolymerization or crosslinking. Plasticizers increase chain mobility by reducing the degree of crystallinity. However, they reduce the mechanical strength of the electrolyte. This hinders the suppression of dendrite growth. On the other hand, the use of crosslinkers contributes to ionic conductivity by decreasing crystallinity and increasing mechanical strength, but can also decrease chain mobility by causing the formation of a rigid polymer structure. This can impede the passage of ions through the electrolyte.

Stainless steel rods have been used as electrodes for EIS analysis of CSE thin films. However, to investigate the interfacial conditions during charge and discharge cycles in a battery system, it is necessary to coat the composite electrolyte with anode and cathode materials. This allows the composite solid electrolyte structure to be better studied in terms of dendrite growth, surface wettability, and mechanical strength. Graphite and sodium metal can be used as anode materials and prussian blue derivatives and metal oxides can be used as cathode materials in sodium ion composite electrolytes.

A coin cell can be produced by using anode and cathode suitable for the CSE thin film and electrolyte produced within the scope of the research. Commercially available CR2032 packages have conical springs 16 mm in diameter and 1 mm in height. These springs provide contact by compressing the anode/electrolyte/cathode system. In this work, the pressure value that provides optimal ionic conductivity is determined. Conical or wave springs that can create this pressure in the CR2032 system can be manufactured and their effect on the capacity of the battery can be investigated.

The ionic conductivity of electrolytes increases with temperature. By using shape memory alloy springs that can generate the optimum pressure as a function of temperature, the expansion/contraction effects that occur in the anode/electrolyte/cathode system as batteries heat up and cool down can be minimized. Thus, dendrite growth and impedance increases at the electrolyte/electrode interfaces can be suppressed by improving the contact surface conditions. Furthermore, if the solid electrolytes produce during this study can be combined with appropriate anode and cathode materials an encapsulated to form a battery cell, life cycle test can be performed to asses the long term performance and durability of the electrolytes and Na^+ ion based solid state batteries.

REFERENCES

1. Liang, Y. and Y. Yao, "Designing Modern Aqueous Batteries", *Nature Reviews Materials*, Vol. 8, No. 2, pp. 109–122, 2022.

2. Zhao, Y., Y. Kang, J. Wozny, J. Lu, H. Du, C. Li, T. Li, F. Kang, N. Tavajohi, and B. Li, "Recycling of Sodium-Ion Batteries", *Nature Reviews Materials*, Vol. 8, No. 9, pp. 623–634, 2023.

3. Zhu, P., D. Gastol, J. Marshall, R. Sommerville, V. Goodship, and E. Kendrick, "A Review of Current Collectors for Lithium-Ion Batteries", *Journal of Power Sources*, Vol. 485, p. 229321, 2021.

4. Liu, W., T. Placke, and K. Chau, "Overview of Batteries and Battery Management for Electric Vehicles", *Energy Reports*, Vol. 8, pp. 4058–4084, 2022.

5. Uchida, Y., G. Hasegawa, K. Shima, M. Inada, N. Enomoto, H. Akamatsu, and K. Hayashi, "Insights into Sodium Ion Transfer at the Na/NASICON Interface Improved by Uniaxial Compression", *ACS Applied Energy and Materials*, Vol. 2, No. 4, pp. 2913–2920, 2019.

6. Yu, R., J.-J. Bao, T.-T. Chen, B.-K. Zou, Z.-Y. Wen, X.-X. Guo, and C.-H. Chen, "Solid Polymer Electrolyte Based on Thermoplastic Polyurethane and Its Application in All-Solid-State Lithium Ion Batteries", *Solid State Ionics*, Vol. 309, pp. 15–21, 2017.

7. Sun, J., H. Yuan, J. Yang, Y.-W. Zhang, and J. Wang, "Electrolytes for Better and Safer Batteries: Liquid, Solid or Frameworked, What's Next?", *Next Materials*, Vol. 1, No. 3, p. 100024, 2023.

8. Wang, H., G. Zhao, S. Wang, D. Liu, Z. Mei, Q. An, J. Jiang, and H. Guo, "Enhanced Ionic Conductivity of a $Na_3Zr_2Si_2PO_{12}$ Solid Electrolyte with Na_2SiO_3

Obtained by Liquid Phase Sintering for Solid-State Na^+ Batteries", *Nanoscale*, Vol. 14, No. 3, pp. 823–832, 2022.

9. Yang, H. and N. Wu, "Ionic conductivity and Ion Transport Mechanisms of Solid-State Lithium-Ion Battery Electrolytes: A Review", *Energy Science and Engineering*, Vol. 10, No. 51, pp. 1643–1671, 2022.

10. Yoshida, K., M. Nakamura, Y. Kazue, N. Tachikawa, S. Tsuzuki, S. Seki, K. Dokko, and M. Watanabe, "Oxidative-Stability Enhancement and Charge Transport Mechanism in Glyme–Lithium Salt Equimolar Complexes", *Journal of the American Chemical Society*, Vol. 133, No. 33, pp. 13121–13129, 2011.

11. Karimi, N., M. Zarrabeitia, A. Mariani, D. Gatti, A. Varzi, and S. Passerini, "Non-fluorinated Ionic Liquid Electrolytes for Lithium Metal Batteries: Ionic Conduction, Electrochemistry, and Interphase Formation", *Advanced Energy Materials*, Vol. 11, No. 4, p. 2003521, 2021.

12. Matsumoto, K., E. Nishiwaki, T. Hosokawa, S. Tawa, T. Nohira, and R. Hagiwara, "Thermal, Physical, and Electrochemical Properties of $Li[N(SO_2F)_2]$-[1-Ethyl-3-methylimidazolium][$N(SO_2F)_2$] Ionic Liquid Electrolytes for Li Secondary Batteries Operated at Room and Intermediate Temperatures", *The Journal of Physical Chemistry C*, Vol. 121, No. 17, pp. 9209–9219, 2017.

13. Lee, S., K. Park, B. Koo, C. Park, M. Jang, H. Lee, and H. Lee, "Safe, Stable Cycling of Lithium Metal Batteries with Low-Viscosity, Fire-Retardant Locally Concentrated Ionic Liquid Electrolytes", *Advanced Functional Materials*, Vol. 30, No. 35, p. 2003132, 2020.

14. Brutti, S., E. Simonetti, M. D. Francesco, A. Sarra, A. Paolone, O. Palumbo, S. Fantini, R. Lin, A. Falgayrat, H. Choi, M. Kuenzel, S. Passerini, and G. Appetecchi, "Ionic Liquid Electrolytes for High-Voltage, Lithium-Ion Batteries", *Journal of Power Sources*, Vol. 479, p. 228791, 2020.

15. Tikekar, M. D., S. Choudhury, Z. Tu, and L. A. Archer, "Design Principles for Electrolytes and Interfaces for Stable Lithium-Metal Batteries", *Nature Energy*, Vol. 1, No. 9, p. 16114, 2016.

16. Ran, L., M. Li, E. Cooper, B. Luo, I. Gentle, L. Wang, and R. Knibbe, "Enhanced Safety and Performance of High-Voltage Solid-State Sodium Battery through Trilayer, Multifunctional Electrolyte Design", *Energy Storage Materials*, Vol. 41, pp. 8–13, 2021.

17. Liu, L., X. Qi, S. Yin, Q. Zhang, X. Liu, L. Suo, H. Li, L. Chen, and Y.-S. Hu, "In Situ Formation of a Stable Interface in Solid-State Batteries", *ACS Energy Letters*, Vol. 4, No. 7, pp. 1650–1657, 2019.

18. Lin, Y., X. Li, W. Zheng, Y. Gang, L. Liu, X. Cui, Y. Dan, L. Chen, and X. Cheng, "Effect of SiO_2 Microstructure on Ionic Transport Behavior of Self-Healing Composite Electrolytes for Sodium Metal Batteries", *Journal of Membrane Science*, Vol. 672, p. 121442, 2023.

19. Boschin, A. and P. Johansson, "Characterization of NaX (X: TFSI, FSI)–PEO Based Solid Polymer Electrolytes for Sodium Batteries", *Electrochimica Acta*, Vol. 175, pp. 124–133, 2015.

20. Goodenough, J. B. and K.-S. Park, "The Li-Ion Rechargeable Battery: A Perspective", *Journal of the American Chemical Society*, Vol. 135, No. 4, pp. 1167–1176, 2013.

21. Zhao, L., Y. Li, M. Yu, Y. Peng, and F. Ran, "Electrolyte-Wettability Issues and Challenges of Electrode Materials in Electrochemical Energy Storage, Energy Conversion, and Beyond", *Advanced Science*, Vol. 10, No. 17, p. 2300283, 2023.

22. Ji, W., B. Luo, Q. Wang, G. Yu, Z. Liu, Z. Zhao, R. Zhao, S. Wang, X. Wang, B. Zhang, J. Zhang, F. Hou, and J. Liang, "Revealing the Influence of Surface

Microstructure on Li Wettability and Interfacial Ionic Transportation for Garnet-Type Electrolytes", *Advanced Energy Materials*, Vol. 13, No. 21, p. 2300165, 2023.

23. Gebert, F., J. Knott, R. Gorkin, S.-L. Chou, and S.-X. Dou, "Polymer Electrolytes for Sodium-Ion Batteries", *Energy Storage Materials*, Vol. 36, pp. 10–30, 2021.

24. Westover, A. S., N. J. Dudney, R. L. Sacci, and S. Kalnaus, "Deposition and Confinement of Li Metal along an Artificial Lipon–Lipon Interface", *ACS Energy Letters*, Vol. 4, No. 3, pp. 651–655, 2019.

25. Park, S., R. Chaudhary, S. A. Han, H. Qutaish, J. Moon, M.-S. Park, and J. H. Kim, "Ionic Conductivity and Mechanical Properties of the Solid Electrolyte Interphase in Lithium Metal Batteries", *Energy Materials*, Vol. 3, p. 300005, 2023.

26. Pang, Y., J. Pan, J. Yang, S. Zheng, and C. Wang, "Electrolyte/Electrode Interfaces in All-Solid-State Lithium Batteries: A Review", *Electrochemical Energy Reviews*, Vol. 4, No. 2, pp. 169–193, 2021.

27. Cao, D., X. Sun, Q. Li, A. Natan, P. Xiang, and H. Zhu, "Lithium Dendrite in All-Solid-State Batteries: Growth Mechanisms, Suppression Strategies, and Characterizations", *Matter*, Vol. 3, No. 1, pp. 57–94, 2020.

28. Liu, H., X.-B. Cheng, J.-Q. Huang, H. Yuan, Y. Lu, C. Yan, G.-L. Zhu, R. Xu, C.-Z. Zhao, L.-P. Hou, C. He, S. Kaskel, and Q. Zhang, "Controlling Dendrite Growth in Solid-State Electrolytes", *ACS Energy Letters*, Vol. 5, No. 3, pp. 833–843, 2020.

29. Huo, H., Y. Chen, J. Luo, X. Yang, X. Guo, and X. Sun, "Rational Design of Hierarchical "Ceramic-in-Polymer" and "Polymer-in-Ceramic" Electrolytes for Dendrite-Free Solid-State Batteries", *Advanced Energy Materials*, Vol. 9, No. 17, p. 1804004, 2019.

30. Zhao, C.-Z., X.-Q. Zhang, X.-B. Cheng, R. Zhang, R. Xu, P.-Y. Chen, H.-J. Peng,

J.-Q. Huang, and Q. Zhang, "An Anion-Immobilized Composite Electrolyte for Dendrite-Free Lithium Metal Anodes", *Proceedings of the National Academy of Sciences*, Vol. 114, No. 42, pp. 11069–11074, 2017.

31. Chen, Y.-T., A. Jena, W. K. Pang, V. K. Peterson, H.-S. Sheu, H. Chang, and R.-S. Liu, "Voltammetric Enhancement of Li-Ion Conduction in Al-Doped $Li_{7-x}La_3Zr_2O_{12}$ Solid Electrolyte", *The Journal of Physical Chemistry C*, Vol. 121, No. 29, pp. 15565–15573, 2017.

32. Han, F., A. S. Westover, J. Yue, X. Fan, F. Wang, M. Chi, D. N. Leonard, N. J. Dudney, H. Wang, and C. Wang, "High Electronic Conductivity as the Origin of Lithium Dendrite Formation within Solid Electrolytes", *Nature Energy*, Vol. 4, No. 3, pp. 187–196, 2019.

33. Zhu, Y., J. C. Gonzalez-Rosillo, M. Balaish, Z. D. Hood, K. J. Kim, and J. L. M. Rupp, "Lithium-Film Ceramics for Solid-State Lithionic Devices", *Nature Reviews Materials*, Vol. 6, No. 4, pp. 313–331, 2020.

34. Usiskin, R., Y. Lu, J. Popovic, M. Law, P. Balaya, Y.-S. Hu, and J. Maier, "Fundamentals, Status and Promise of Sodium-Based Batteries", *Nature Reviews Materials*, Vol. 6, No. 11, pp. 1020–1035, 2021.

35. Mousavinezhad, S., S. Nili, A. Fahimi, and E. Vahidi, "Environmental Impact Assessment of Direct Lithium Extraction from Brine Resources: Global Warming Potential, Land Use, Water Consumption, and Charting Sustainable Scenarios", *Resources, Conservation and Recycling*, Vol. 205, p. 107583, 2024.

36. Yang, X., H. Wen, Y. Liu, Y. Huang, Q. Zhang, W. Wang, H. Zhang, J. Fu, G. Li, Q. Liu, and G. Jiang, "Lithium Pollution and Its Associated Health Risks in the Largest Lithium Extraction Industrial Area in China", *Environmental Science and Technology*, Vol. 58, pp. 11637–11648, 2024.

37. Yang, J., G. Liu, M. Avdeev, H. Wan, F. Han, L. Shen, Z. Zou, S. Shi, Y.-S. Hu, C. Wang, and X. Yao, "Ultrastable All-Solid-State Sodium Rechargeable Batteries", *ACS Energy Letters*, Vol. 5, No. 9, pp. 2835–2841, 2020.

38. Desai, A. V., R. E. Morris, and A. R. Armstrong, "Advances in Organic Anode Materials for Na-/K-Ion Rechargeable Batteries", *ChemSusChem*, Vol. 13, No. 18, pp. 4866–4884, 2020.

39. Vaalma, C., D. Buchholz, M. Weil, and S. Passerini, "A Cost and Resource Analysis of Sodium-Ion Batteries", *Nature Reviews Materials*, Vol. 3, No. 4, p. 18013, 2018.

40. Ran, L., S. Tao, I. Gentle, B. Luo, M. Li, M. Rana, L. Wang, and R. Knibbe, "Stable Interfaces in a Sodium Metal-Free, Solid-State Sodium-Ion Battery with Gradient Composite Electrolyte", *ACS Applied Materials and Interfaces*, Vol. 13, No. 33, pp. 39355–39362, 2021.

41. Ling, W., N. Fu, J. Yue, X. Zeng, Q. Ma, Q. Deng, Y. Xiao, L. Wan, Y. Guo, and X. Wu, "A Flexible Solid Electrolyte with Multilayer Structure for Sodium Metal Batteries", *Advanced Energy Materials*, Vol. 10, No. 9, p. 1903966, 2020.

42. Wang, Y., Z. Wang, J. Sun, F. Zheng, M. Kotobuki, T. Wu, K. Zeng, and L. Lu, "Flexible, Stable, Fast-Ion-Conducting composite electrolyte composed of nanostructured Na-super-ion-conductor framework and continuous Poly(ethylene oxide) for all-solid-state Na battery", *Journal of Power Sources*, Vol. 454, p. 227949, 2020.

43. Yu, W., Y. Zhai, G. Yang, J. Yao, S. Song, S. Li, W. Tang, N. Hu, and L. Lu, "A Composite Electrolyte with $Na_3Zr_2Si_2PO_{12}$ Microtube for Solid-State Sodium-Metal Batteries", *Ceramics International*, Vol. 47, No. 8, pp. 11156–11168, 2021.

44. Koo, B., S. Hwang, K. H. Ahn, C. Lee, and H. Lee, "Low Solvating Power of

Acetonitrile Facilitates Ion Conduction: A Solvation–Conductivity Riddle", *The Journal of Physical Chemistry Letters*, Vol. 15, No. 12, pp. 3317–3322, 2024.

45. Ji, Y., Y.-H. Zhang, F.-N. Shi, and L.-N. Zhang, "UV-Derived Double Crosslinked PEO-Based Solid Polymer Electrolyte for Room Temperature", *Journal of Colloid and Interface Science*, Vol. 629, pp. 492–500, 2023.

46. Chai, S., Q. He, J. Zhou, Z. Chang, A. Pan, and H. Zhou, "Solid-State Electrolytes and Electrode/Electrolyte Interfaces in Rechargeable Batteries", *ChemSusChem*, Vol. 17, No. 3, p. 2023012, 2023.

47. Ruan, Y., X. Huang, H. Lei, Y. Liu, J. Wang, W. Sun, and S. Song, "A Flexible and Free-Standing Composite Solid Electrolyte with a Pomegranate-Like Structure for Solid-State Sodium-Ion Batteries", *Solid State Ionics*, Vol. 403, p. 116406, 2023.

48. Wang, X., Y. Fang, X. Yan, S. Liu, X. Zhao, and L. Zhang, "Highly Conductive Polymer Electrolytes Based on PAN-PEI Nanofiber Membranes with In Situ Gelated Liquid Electrolytes for Lithium-Ion Batteries", *Polymer*, Vol. 230, p. 124038, 2021.

49. Yang, J.-M., N.-C. Wang, and H.-C. Chiu, "Preparation and Characterization of Poly(vinyl alcohol)/Sodium Alginate Blended Membrane for Alkaline Solid Polymer Electrolytes Membrane", *Journal of Membrane Science*, Vol. 457, pp. 139–148, 2014.

50. Dua, K., P. Kumbhar, S. Nadaf, A. Manjappa, P. Karade, U. Mali, S. K. Singh, J. Disouza, and V. Patravale, *Polymer Dissolution*, Elsevier, Cambridge, 2024.

51. Zhao, C., L. Liu, X. Qi, Y. Lu, F. Wu, J. Zhao, Y. Yu, Y. Hu, and L. Chen, "Solid-State Sodium Batteries", *Advanced Energy Materials*, Vol. 8, No. 17, p. 1703012, 2018.

52. Quartarone, E. and P. Mustarelli, "Electrolytes for Solid-State Lithium Rechargeable Batteries: Recent Advances and Perspectives", *Chemical Society Reviews*, Vol. 40, No. 5, p. 2525, 2011.

53. Zhao, Y., L. Wang, Y. Zhou, Z. Liang, N. Tavajohi, B. Li, and T. Li, "Solid Polymer Electrolytes with High Conductivity and Transference Number of Li Ions for Li-Based Rechargeable Batteries", *Advanced Science*, Vol. 8, No. 7, p. 2003675, 2021.

54. Nofal, M. M., S. B. Aziz, J. M. Hadi, R. T. Abdulwahid, E. M. A. Dannoun, A. S. Marif, S. Al-Zangana, Q. Zafar, M. A. Brza, and M. F. Z. Kadir, "Synthesis of Porous Proton Ion Conducting Solid Polymer Blend Electrolytes Based on PVA: CS Polymers: Structural, Morphological and Electrochemical Properties", *Materials*, Vol. 13, No. 21, p. 4890, 2020.

55. Reddy, M. R., M. J. Reddy and A. R. Subrahmanyam, "Structural, Thermal and Optical Properties of PMMA, PEO and PMMA/PEO/$LiClO_4$ Polymer Electrolyte Blends", *Material Science Research India*, Vol. 14, No. 2, pp. 123–127, 2017.

56. Song, S., M. Kotobuki, F. Zheng, C. Xu, S. V. Savilov, N. Hu, L. Lu, Y. Wang, and W. D. Z. Li, "A Hybrid Polymer/Oxide/Ionic-Liquid Solid Electrolyte for Na-Metal Batteries", *Journal of Materials Chemistry A*, Vol. 5, No. 34, pp. 6424–6431, 2017.

57. Khurana, R., J. L. Schaefer, L. A. Archer, and G. W. Coates, "Suppression of Lithium Dendrite Growth Using Cross-Linked Polyethylene/Poly(ethylene oxide) Electrolytes: A New Approach for Practical Lithium-Metal Polymer Batteries", *Journal of the American Chemical Society*, Vol. 136, No. 20, pp. 7395–7402, 2014.

58. Zheng, Y., Y. Yao, J. Ou, M. Li, D. Luo, H. Dou, Z. Li, K. Amine, A. Yu, and Z. Chen, "A Review of Composite Solid-State Electrolytes for Lithium Batter-

ies: Fundamentals, Key Materials and Advanced Structures", *Chemical Society Reviews*, Vol. 49, No. 23, pp. 8790–8839, 2020.

59. Lu, Y., L. Li, Q. Zhang, Z. Niu, and J. Chen, "Electrolyte and Interface Engineering for Solid-State Sodium Batteries", *Joule*, Vol. 2, No. 9, pp. 1747–1770, 2018.

60. Dong, Y., P. Wen, H. Shi, Y. Yu, and Z. Wu, "Solid-State Electrolytes for Sodium Metal Batteries: Recent Status and Future Opportunities", *Advanced Functional Materials*, Vol. 34, No. 5, p. 2213584, 2024.

61. Zhou, C., S. Bag, and V. Thangadurai, "Engineering Materials for Progressive All-Solid-State Na Batteries", *ACS Energy Letters*, Vol. 3, No. 9, pp. 2181–2198, 2018.

62. Anantharamulu, N., K. K. Rao, G. Rambabu, B. V. Kumar, V. Radha, and M. Vithal, "A Wide-Ranging Review on Nasicon Type Materials", *Journal of Materials Science*, Vol. 46, No. 9, pp. 2821–2837, 2011.

63. Zhang, Z., Z. Zou, K. Kaup, R. Xiao, S. Shi, M. Avdeev, Y. Hu, D. Wang, B. He, H. Li, X. Huang, L. F. Nazar, and L. Chen, "Correlated Migration Invokes Higher Na^+-Ion Conductivity in NASICON-Type Solid Electrolytes", *Advanced Energy Materials*, Vol. 9, No. 42, p. 1902373, 2019.

64. Li, Y., M. Li, Z. Sun, Q. Ni, H. Jin, and Y. Zhao, "Recent Advance on NASICON Electrolyte in Solid-State Sodium Metal Batteries", *Energy Storage Materials*, Vol. 56, pp. 582–599, 2023.

65. Maurya, D. K., R. Dhanusuraman, Z. Guo, and S. Angaiah, "Composite Polymer Electrolytes: Progress, Challenges, and Future Outlook for Sodium-Ion Batteries", *Advanced Composites and Hybrid Materials*, Vol. 5, No. 4, pp. 2651–2674, 2022.

66. Wang, W., W. Yuan, Z. Zhao, P. Zhou, P. Zhang, M. Ding, J. Bai, and J. Weng, "Sandwiched Composite Electrolyte with Excellent Interfacial Contact for High-Performance Solid-State Sodium-Ion Batteries", *Journal of Colloid and Interface Science*, Vol. 652, pp. 132–141, 2023.

67. Neha, A. D., "Fast Ionic PEO-$NaCF_3SO_3$-$Na_3Zr_2Si_2P_3O_{12}$ Membranes for All-Solid-State Energy Storage Devices", *Materials Science and Engineering: B*, Vol. 289, p. 116252, 2023.

68. Yu, X., L. Xue, J. B. Goodenough, and A. Manthiram, "All-Solid-State Sodium Batteries with a Polyethylene Glycol Diacrylate–$Na_3Zr_2Si_2PO_{12}$ Composite Electrolyte", *Advanced Energy and Sustainability Research*, Vol. 2, No. 1, p. 2000061, 2021.

69. Bhide, A. and K. Hariharan, "Composite Polymer Electrolyte Based on $(PEO)_6$:$NaPO_3$ Dispersed with $BaTiO_3$", *Polymer International*, Vol. 57, No. 3, pp. 523–529, 2008.

70. Ban, X., W. Zhang, N. Chen, and C. Sun, "A High-Performance and Durable Poly(ethylene oxide)-Based Composite Solid Electrolyte for All Solid-State Lithium Battery", *The Journal of Physical Chemistry C*, Vol. 122, No. 18, pp. 9852–9858, 2018.

71. Shin, H., S. Lee, H. S. Jung, and J.-B. Kim, "Effect of Ball Size and Powder Loading on the Milling Efficiency of a Laboratory-Scale Wet Ball Mill", *Ceramics International*, Vol. 39, No. 8, pp. 8963–8968, 2013.

72. Yu, X., L. Xue, J. B. Goodenough, and A. Manthiram, "A High-Performance All-Solid-State Sodium Battery with a Poly(ethylene oxide)–$Na_3Zr_2Si_2PO_{12}$ Composite Electrolyte", *ACS Materials Letters*, Vol. 1, No. 1, pp. 132–138, 2019.

73. Moradipour, F., A. Markert, T. Rudszuck, N. Röttgen, G. Dück, M. Finsterbusch,

F. Gerbig, H. Nirschl, and G. Guthausen, "Na^+ Mobility in PEO-Based Composite Solid-State Electrolytes by NMR", *Journal of Energy and Power Technology*, Vol. 5, No. 4, pp. 1–21, 2023.

74. Ni'mah, Y. L., M.-Y. Cheng, J. H. Cheng, J. Rick, and B.-J. Hwang, "Solid-State Polymer Nanocomposite Electrolyte of TiO_2/PEO/$NaClO_4$ for Sodium Ion Batteries", *Journal of Power Sources*, Vol. 278, pp. 375–381, 2015.

75. Chandra, A., A. Chandra, and K. Thakur, "Synthesis and Characterization of Hot Pressed Ion Conducting Solid Polymer Electrolytes: (1-x)PEO:x$NaClO_4$", *The European Physical Journal Applied Physics*, Vol. 69, No. 2, p. 20901, 2015.

76. Shindrov, A. A., K. V. Mishchenko, O. A. Podgornova, A. A. Shapovalova, and N. V. Kosova, "Solvent Free PEO-$NaClO_4$:$Na_3Zr_2Si_2PO_{12}$ Composite Solid Polymer Electrolytes: Comparison of Conductive Properties of "Ceramics-in-Polymer" and "Polymer-in-Ceramics"", *Solid State Ionics*, Vol. 406, p. 116485, 2024.

77. Kuila, T., H. Acharya, S. Srivastava, B. Samantaray, and S. Kureti, "Enhancing the Ionic Conductivity of PEO Based Plasticized Composite Polymer Electrolyte by $LaMnO_3$ Nanofiller", *Materials Science and Engineering: B*, Vol. 137, No. 1-3, pp. 217–224, 2007.

78. Singh, M. D., A. Dalvi, and D. Phase, "Electrical Transport in PEO-NaI-NASICON Nanocomposites: An Assessment Using Impedance and X-Ray Absorption Spectroscopy", *Materials Research Bulletin*, Vol. 118, p. 110485, 2019.

79. Moreno, J. S., M. Armand, M. Berman, S. Greenbaum, B. Scrosati, and S. Panero, "Composite PEO_n:NaTFSI Polymer Electrolyte: Preparation, Thermal and Electrochemical Characterization", *Journal of Power Sources*, Vol. 248, pp. 695–702, 2014.

80. Tang, B., P. W. Jaschin, X. Li, S.-H. Bo, and Z. Zhou, "Critical Interface Between

Inorganic Solid-State Electrolyte and Sodium Metal", *Materials Today*, Vol. 41, pp. 200–218, 2020.

81. Bhide, A. and K. Hariharan, "A New Polymer Electrolyte System $(PEO)_n$:$NaPO_3$", *Journal of Power Sources*, Vol. 159, No. 2, pp. 1450–1457, 2006.

82. Zhang, L., Y. Liu, J. Han, C. Yang, X. Zhou, Y. Yuan, and Y. You, "Al Doped into Si/P Sites of $Na_3Zr_2Si_2PO_{12}$ with Conducted Na_3PO_4 Impurities for Enhanced Ionic Conductivity", *ACS Applied Materials and Interfaces*, Vol. 15, No. 38, pp. 44867–44875, 2023.

83. Tanibata, N., K. Noi, A. Hayashi, and M. Tatsumisago, "Preparation and Characterization of Highly Sodium Ion Conducting Na_3PS_4–Na_4SiS_4 Solid Electrolytes", *RSC Advances*, Vol. 4, No. 33, pp. 17120–17123, 2014.

84. Anantha, P. and K. Hariharan, "Physical and Ionic Transport Studies on Poly(ethylene oxide)-$NaNO_3$ Polymer Electrolyte System", *Solid State Ionics*, Vol. 176, pp. 155–162, 2005.

85. Duraikkan, V., A. B. Sultan, N. Nallaperumal, and A. Shunmuganarayanan, "Structural, Thermal and Electrical Properties of Polyvinyl Alcohol/Poly(vinyl pyrrolidone)–Sodium Nitrate Solid Polymer Blend Electrolyte", *Ionics*, Vol. 24, No. 1, pp. 139–151, 2018.

86. Shen, Z., G. P. Simon, and Y.-B. Cheng, "Comparison of Solution Intercalation and Melt Intercalation of Polymer–Clay Nanocomposites", *Polymer*, Vol. 43, No. 15, pp. 4251–4260, 2002.

87. Dey, A., K. Das, S. Karan, and S. De, "Vibrational Spectroscopy and Ionic Conductivity of Polyethylene Oxide–$NaClO_4$–CuO Nanocomposite", *Spectrochimica Acta Part A: Molecular and Biomolecular Spectroscopy*, Vol. 83, No. 1, pp. 384–391, 2011.

88. Giarola, M., A. Sanson, F. Tietz, S. Pristat, E. Dashjav, D. Rettenwander, G. J. Redhammer, and G. Mariotto, "Structure and Vibrational Dynamics of NASICON-Type $LiTi_2(PO_4)_3$", *The Journal of Physical Chemistry C*, Vol. 121, No. 7, pp. 3697–3706, 2017.

89. Wang, X., X. Xu, Y. Li, W. Chen, G. Zhao, H. Wang, Y. Tang, P. Wu, and L. Tang, "Effects of Sodium Vacancies and Concentrations in Na_3SO_4F Solid Electrolyte", *ACS Omega*, Vol. 2, No. 11, pp. 13051–13058, 2024.

90. Olson, M., S. Kmiec, N. Riley, N. Oldham, K. Krupp, A. Manthiram, and S. W. Martin, "Structure and Properties of Na_2S–SiS_2–P_2S_5–$NaPO_3$ Glassy Solid Electrolytes", *Inorganic Chemistry*, Vol. 63, No. 20, pp. 9129–9144, 2024.

91. Chong, M. K., Z. Zainuddin, F. S. Omar, M. H. H. Jumali, and M. Ansari, "Influence of Excess Sodium and Phosphorus on the Ionic Conductivity of NASICON-Structured $Na_3Zr_2(SiO_4)_2PO_4$ Ceramic Solid Electrolyte", *Journal of Energy Storage*, Vol. 90, p. 111873, 2024.

92. Wang, J., J. Kang, X. Guo, S. Hu, Y. Tang, L. Jin, and X. Wei, "Enhanced Ionic Conductivity in $Na_3Zr_2Si_2PO_{12}$ NASICON-Type Solid Electrolytes by Adding Mg^{2+}-ions", *Journal of Alloys and Compounds*, Vol. 988, p. 174327, 2024.

93. Gebi, A. I., O. Dolokto, L. Mereacre, U. Geckle, H. Radinger, M. Knapp, and H. Ehrenberg, "Characterization and Comparative Study of Energy Efficient Mechanochemically Induced NASICON Sodium Solid Electrolyte Synthesis", *ChemSusChem*, Vol. 17, No. 2, p. 2023008, 2024.

94. Johan, M. R., O. H. Shy, S. Ibrahim, S. M. M. Yassin, and T. Y. Hui, "Effects of Al_3O_3 Nanofiller and EC Plasticizer on the Ionic Conductivity Enhancement of Solid PEO–$LiCF_3SO_3$ Solid Polymer Electrolyte", *Solid State Ionics*, Vol. 196, No. 1, pp. 41–47, 2011.

95. Wang, C., C. Wang, M. Li, S. Zhang, C. Zhang, S. Chou, J. Mao, and Z. Guo, "Design of Thin Solid-State Electrolyte Films for Safe and Energy-Dense Batteries", *Materials Today*, Vol. 72, pp. 235–254, 2024.

96. Baranowski, L. L., C. M. Heveran, V. L. Ferguson, and C. R. Stoldt, "Multi-Scale Mechanical Behavior of the Li_3PS_4 Solid-Phase Electrolyte", *ACS Applied Materials and Interfaces*, Vol. 8, No. 43, pp. 29573–29579, 2016.

97. Dixit, M., N. Muralidharan, A. Bisht, C. J. Jafta, C. T. Nelson, R. Amin, R. Essehli, M. Balasubramanian, and I. Belharouak, "Tailoring of the Anti-Perovskite Solid Electrolytes at the Grain-Scale", *ACS Energy Letters*, Vol. 8, No. 5, pp. 2356–2364, 2023.

98. Hu, C., K. Xia, C. Fu, X. Zhao, and T. Zhu, "Carrier Grain Boundary Scattering in Thermoelectric Materials", *Energy and Environmental Science*, Vol. 15, No. 4, pp. 1406–1422, 2022.

99. Jee, A.-Y., H. Lee, Y. Lee, and M. Lee, "Determination of the Elastic Modulus of Poly(ethylene oxide) Using a Photoisomerizing Dye", *Chemical Physics*, Vol. 422, pp. 246–250, 2013.

100. Nonemacher, J. F., S. Naqash, F. Tietz, and J. Malzbender, "Micromechanical Assessment of Al/Y-Substituted NASICON Solid Electrolytes", *Ceramics International*, Vol. 45, No. 17, pp. 21308–21314, 2019.

101. Laxmiprasanna, N., P. S. Reddy, G. S. Kumar, M. B. Reddy, K. K. Ganta, V. R. Jeedi, and B. Praveen, "A Review on Nano Composite Polymer Electrolytes for High-Performance Batteries", *Materials Today: Proceedings*, Vol. 72, pp. 286–292, 2023.

APPENDIX A: ADDITIONAL FIGURES

Figure A.1 shows the authorization for Figure 1.6, showing the rhombohedral and monoclinic phases of NASICON mentioned under the heading of Inorganic Additives.

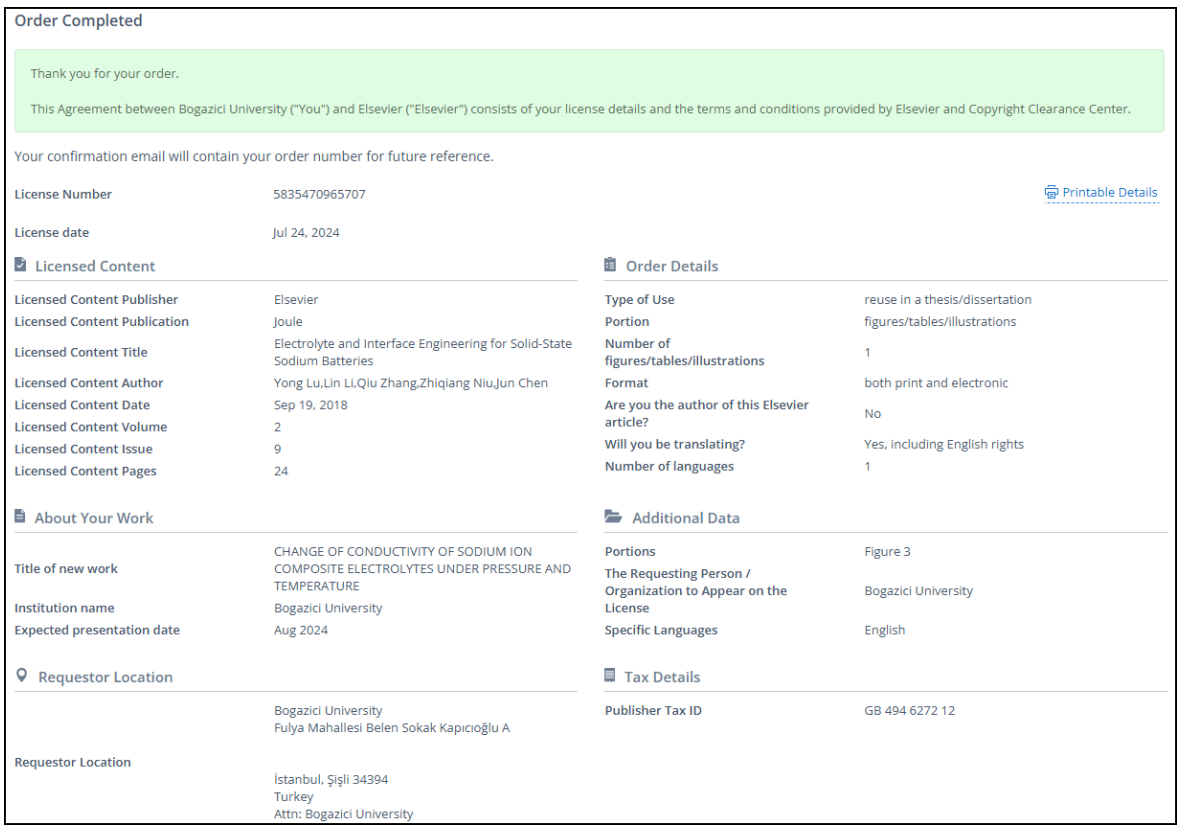

Order Completed

Thank you for your order.

This Agreement between Bogazici University ("You") and Elsevier ("Elsevier") consists of your license details and the terms and conditions provided by Elsevier and Copyright Clearance Center.

Your confirmation email will contain your order number for future reference.

Printable Details

License Number	5835470965707
License date	Jul 24, 2024

Licensed Content

Licensed Content Publisher	Elsevier
Licensed Content Publication	Joule
Licensed Content Title	Electrolyte and Interface Engineering for Solid-State Sodium Batteries
Licensed Content Author	Yong Lu,Lin Li,Qiu Zhang,Zhiqiang Niu,Jun Chen
Licensed Content Date	Sep 19, 2018
Licensed Content Volume	2
Licensed Content Issue	9
Licensed Content Pages	24

Order Details

Type of Use	reuse in a thesis/dissertation
Portion	figures/tables/illustrations
Number of figures/tables/illustrations	1
Format	both print and electronic
Are you the author of this Elsevier article?	No
Will you be translating?	Yes, including English rights
Number of languages	1

About Your Work

Title of new work	CHANGE OF CONDUCTIVITY OF SODIUM ION COMPOSITE ELECTROLYTES UNDER PRESSURE AND TEMPERATURE
Institution name	Bogazici University
Expected presentation date	Aug 2024

Additional Data

Portions	Figure 3
The Requesting Person / Organization to Appear on the License	Bogazici University
Specific Languages	English

Requestor Location

Requestor Location	Bogazici University Fulya Mahallesi Belen Sokak Kapıcıoğlu A İstanbul, Şişli 34394 Turkey Attn: Bogazici University

Tax Details

Publisher Tax ID	GB 494 6272 12

Figure A.1. Permission for Figure 1.6.

Figure A.2 displays the error rates of resistance and CPEs in the equivalent circuit models of c and d. Equivalent circuit model of c has a single resistor and two CPEs. The resistor in equivalent circuit model of c models the grain boundary resistance and the error rate of the resistor is 1.05%. Equivalent circuit model of d has two resistors and two CPEs and the error rate of the resistor modelling the grain boundary resistance is 1.55%. The error rate of the equivalent circuit model of c used for the fitting study is lower than that of the equivalent circuit model of d. Figure A.3 shows the error rates in the equivalent circuit models of CSEs containing different weight ratios of NASICON.

(a)

	Parameter	Value	± Error	Units
1	Yo1	5,7018e-07	3,5603e-08	S*s^a
2	a1	0,6596	1,2074e-02	1
3	Yo_grain_boundary	6,2690e-11	8,4855e-12	S*s^a
4	a_grain_boundary	0,9250	9,1758e-03	3
5	R_grain_boundary	45215,2227	477,7302	ohm
6	Goodness of Fit	3,5266e-05		
7	Frequency Range	Not specified		
8	Status Message: Success			

(b)

	Parameter	Value	± Error	Units
1	Yo_grain_boundary	6,2688e-11	1,3336e-11	S*s^a
2	a_grain_boundary	0,9250	1,5406e-02	1
3	Yo1	5,7018e-07	3,8357e-08	S*s^a
4	a1	0,6596	1,3048e-02	3
5	R_bulk	1,1407e-03	350,9258	ohm
6	R_grain_boundary	45215,1079	699,6808	ohm
7	Goodness of Fit	3,5266e-05		
8	Frequency Range	Not specified		
9	Status Message: Success			

Figure A.2. The error rates of the parameters of the CPEs and resistors in (a) equivalent circuit of c, and (b) equivalent circuit of d.

(a)

	Parameter	Value	± Error	Units
1	Yo1	1,5383e-05	6,1502e-07	S*s^a
2	a1	0,7256	6,8329e-03	1
3	Yo_grain_boundary	6,3215e-10	8,4367e-10	S*s^a
4	a_grain_boundary	0,8799	0,0864	3
5	R_grain_boundary	330,4689	3,3146	ohm
6	Goodness of Fit	3,2229e-04		
7	Frequency Range	Not specified		
8	Status Message: Success			

(b)

	Parameter	Value	± Error	Units
1	Yo1	4,5941e-06	1,4518e-07	S*s^a
2	a1	0,7423	4,7661e-03	1
3	Yo_grain_boundary	3,6652e-08	6,6579e-08	S*s^a
4	a_grain_boundary	0,6342	0,1156	3
5	R_grain_boundary	223,1370	3,5886	ohm
6	Goodness of Fit	1,9441e-03		
7	Frequency Range	Not specified		
8	Status Message: Success			

(c)

	Parameter	Value	± Error	Units
1	Yo1	2,9282e-06	1,2119e-07	S*s^a
2	a1	0,8436	7,2851e-03	1
3	Yo_grain_boundary	3,9411e-09	2,4078e-09	S*s^a
4	a_grain_boundary	0,7398	3,9654e-02	3
5	R_grain_boundary	1084,8161	10,6824	ohm
6	Goodness of Fit	8,0045e-04		
7	Frequency Range	Not specified		
8	Status Message: Success			

(d)

	Parameter	Value	± Error	Units
1	Yo1	4,6412e-06	2,0104e-07	S*s^a
2	a1	0,7561	7,6729e-03	1
3	Yo_grain_boundary	6,1788e-09	3,0451e-09	S*s^a
4	a_grain_boundary	0,7227	3,2011e-02	3
5	R_grain_boundary	1206,3431	13,0352	ohm
6	Goodness of Fit	8,2132e-04		
7	Frequency Range	Not specified		
8	Status Message: Success			

Figure A.3. The error rates of the CSEs containing (a) 20 wt% NASICON, (b) 25 wt% NASICON, (c) 30 wt% NASICON, and (d) 40 wt% NASICON.